D 2022

U.PORTO
FEUP FACULDADE DE ENGENHARIA
UNIVERSIDADE DO PORTO

HIGHLY EFFICIENT MONOLITHIC DYE-SENSITIZED SOLAR CELLS

FÁTIMA EDUARDA OLIVEIRA SANTOS
TESE DE DOUTORAMENTO APRESENTADA
À FACULDADE DE ENGENHARIA DA UNIVERSIDADE DO PORTO EM
ENGENHARIA QUÍMICA E BIOLÓGICA

This thesis was financially supported by Foundation for Science and Technology (FCT) through the **PhD grant SFRH/BD/132388/2017**. The research leading to these results has received funding from: i) **BI-DSC** (No. 321315) funded by the European Commission through the 7th Framework Programme, the Specific Programme "Ideas" of the European Research Council as part of an Advanced Grant; ii) **SunStorage**, with reference POCI-01-0145-FEDER-016387, funded by the European Regional Development Fund (ERDF) through COMPETE 2020 - Operational Programme for Competitiveness and Internationalization (POCI), by FCT; iii) **2SMART**, with reference NORTE-01-0145-FEDER-000054, supported by Norte Portugal Regional Operational Programme (NORTE 2020), under the PORTUGAL 2020 Partnership Agreement, through the ERDF; iv) project **HopeH$_2$**, with reference POCI-01-0145-FEDER-030760, funded by FEDER funds through COMPETE2020 – Operational Programme for Competitiveness and Internationalization (POCI) and by national funds (PIDDAC) through FCT/MCTES; and v) LA/P/0045/2020 (**ALiCE**), UIDB/00511/2020 and UIDP/00511/2020 (**LEPABE**), funded by national funds through FCT/MCTES (PIDDAC).

Fátima Santos

LEPABE - Laboratory for Process Engineering, Environment, Biotechnology and Energy

ALiCE - Associate Laboratory in Chemical Engineering

University of Porto – Faculty of Engineering

Rua Dr. Roberto Frias s/n, 4200-465 Porto, Portugal

Agradecimentos

Em primeiro lugar, quero agradecer ao meu orientador, o Prof. Dr. Adélio Mendes, por me ter incentivado a iniciar o trabalho de investigação e a ingressar no programa doutoral. Foram quatro anos com altos e baixos, mas agradeço-lhe por toda a ajuda e orientação, e por estar sempre disponível para responder às chamadas dos seus alunos, mesmo que muitas vezes olhe para o telefone, e pense: "Ai, que chatos!". Agradeço imenso também ao meu co-orientador, o Dr. Dzmitry Ivanou, por toda a paciência e orientação ao longo do doutoramento, por me esclarecer todas as dúvidas, e por considerar sempre as minhas ideias, mesmo aquelas que, bem… Talvez não devesse ter considerado. Agradeço também ao Dr. José Nogueira e Ana Pereira, que me orientaram e ajudaram no início desta jornada; sem as vossas primeiras experiências com as M-DSSCs esta tese não existiria. Obrigada aos meus colegas da equipa das DSSCs, Carolina Hora e Jeffrey Capitão, por todo o companheirismo e entreajuda. Ao longo destes quatro anos juntos, acabamos por "desencaminhar" o Jorge Martins a juntar-se a nós, e convencemos a Daniela Rodrigues a diminuir o trabalho em Coimbra e a vir trabalhar connosco. Também a eles, o meu obrigada. Aos meus restantes colegas, estudantes e doutorados, obrigada por tornarem o nosso laboratório um excelente local para trabalhar, sempre com boa disposição, e que os convívios perdurem; os churrascos e os jogos de voleibol unem toda a equipa e são sempre uma boa forma de descontrair depois de um dia de trabalho até tarde.

A nível pessoal sinto-me grata por ter pessoas muito especiais ao meu lado. Às minhas melhores amigas, que me acompanham desde a pré-escola e com as quais partilhei tantos momentos, incluindo até as imprudências da adolescência, só posso tecer elogios.

À minha família perfeitamente imperfeita, são eles os responsáveis por quem eu sou, pela minha personalidade e pela caraterística que mais me reconhecem, o meu sentido de humor (ou falta dele). Obrigada ao meu irmão Fábio Santos, a pessoa que mais me incentivou a estudar engenharia. Por causa da televisão e das séries, pensa que o meu trabalho de laboratório envolve síntese de drogas ou produção de bombas, mas, um dia, ele há de entender. À minha querida cunhada Cláudia Barbosa, obrigada por permitires que o meu teletrabalho tenha sido produtivo, mesmo com os "pestinhas" dos meus sobrinhos, Mariana e Leonardo, lá em casa. Ao meu namorado e melhor amigo Rui Carmo, obrigada por todo o apoio; para alguém que trabalha em gestão, devido ao meu trabalho, já incluíste as palavras "monolíticas" e "Grätzel" no teu vocabulário.

Por fim, o agradecimento mais especial e profundo desta tese, é para os meus pais, Manuel Teixeira e Madalena Soares: obrigada pelos valores e princípios que me transmitem desde criança, e por todos os sacrifícios que fizeram para me permitirem ingressar no ensino superior. Espero deixar-vos orgulhosos!

Estes quatro anos foram difíceis, mas muito gratificantes. Espero terminar esta jornada com sucesso, e que novos projetos e desafios surjam brevemente. Muito obrigada a todos!

To my beloved family

Preface

In 2017, Adélio Mendes' research team performed the first experiments with monolithic dye-sensitized solar cells. The monolithic design allows straightforward fabricating in-series modules and reduces material costs. The goal was to produce efficient, stable, and cost-effective M-DSSCs. After getting my PhD scholarship from Foundation for Science and Technology (grant SFRH/BD/132388/2017), this became the focus of my entire PhD thesis, which is here submitted for the degree of Doctor of Philosophy at the University of Porto – Faculty of Engineering (FEUP).

The present work was developed at the Laboratory for Process Engineering, Environment, Biotechnology and Energy (LEPABE) and at the Associate Laboratory in Chemical Engineering (ALiCE), Chemical Engineering Department of the Faculty of Engineering - University of Porto (FEUP), between 2017 and 2021. The work was supervised by Professor Adélio Mendes and co-supervised by Doctor Dzmitry Ivanou, both from FEUP-LEPABE. The thesis is based on 4 scientific articles; two articles are currently under peer-review, and two articles were published.

The thesis consists of five chapters: one review paper that represents an introduction chapter; three scientific papers, where each paper represents one independent chapter; and a final chapter with the general conclusions and the prospects of future work.

CONTENTS

CHAPTER 4

CHAPTER 5

APPENDIX

Abstract

The rapid growth of the Internet of Things (IoT) implies the installation of billions of wireless sensors over the coming decades. Nowadays, cordless and sustainable power strategies for IoTs and billions of other emerging low-power electronics have become imperative. Indoor photovoltaics (iPVs) turned into one of the most promising pathways to address this challenge. In 2021, the estimated market of iPVs was above 10^9 USD, corresponding to hundreds of millions of installed units. Dye-sensitized solar cells (DSSCs) are one of the most promising iPVs technologies, offering low production cost, simple and versatile architecture, low environmental impact, and non-toxicity. Photocurrent quantum yield of the DSSCs is perfectly fitted with the emission spectra of most lamps for indoor use, leading to incredible power conversion efficiency (PCE) values; DSSCs hold a PCE record of 34.5 % under 1000 lx room light. Recently, several companies launched the commercial production of indoor DSSCs.

Monolithic DSSCs (M-DSSCs) attracted much technological interest. They need only one transparent conductive oxide substrate, allowing a 20-30 % reduction of the device costs, and making the production of modules becomes straightforward. The drawback of M-DSSCs is the lower PCE compared with their conventional counterparts. This hurdle is typically due to insufficient light harvesting caused by poor reflectivity of the spacer layer, higher charge transfer resistance at spacer layer/counter-electrode interface, higher diffusion and series resistances, and low fill factor. This thesis addresses these weaknesses by demonstrating efficient, stable, and cost-effective M-DSSCs architectures.

The spacer layer was one of the least studied components of M-DSSC. In this work, new SiO_2 spacer layers, derived from an entirely water-based formulation, were developed; 30 wt.% of TiO_2 nanoparticles in silica increased the reflectance of these spacer layers and rendered M-DSSC with a record 1-sun PCE of 8.3 % for iodide-mediated device. Another PCE record was achieved in this work, developing the first cobalt-mediated M-DSSC. The apparent activation energy for electron transfer, the electron charge transfer resistance, and the exchange current density of different materials - Pt nanoparticles, Pt metal, graphite/carbon-black, and PEDOT:PSS - in the cobalt electrolyte, were determined to select the most favorable catalyst for the reduction of $Co(III)(bpy)_3$. Cobalt M-DSSC with carbon counter-electrode and highly reflective rutile spacer layer displayed 1-sun PCE of 9.5 % and *ca.* 22 % under 1000 lx indoor LED light. The sensitization conditions of M-DSSCs, as well as the concentration of 4-*tert*-butylpyridine (TBP) in cobalt electrolyte, were addressed to produce efficient devices.

Finally, the reported most stable cobalt M-DSSC was developed, implementing a state-of-the-art glass encapsulation process, which displayed exceptional hermeticity levels. The device edges and the electrolyte injection holes were glass-sealed using a laser-assisted process. The

standard helium gas leak test MIL-STD-883, method 1014.10, performed before and after humidity-freeze cycles following IEC 61646 standard, confirmed the hermeticity and robustness of the device encapsulation. Glass-encapsulated M-DSSCs with ACN-based cobalt electrolyte passed successfully, for the first time ever, several ISOS tests, including thermal cycling up to 85 ^{o}C, 1000 h of shelf-aging, and 1000 h of solar and artificial light soaking with passive load, showing the most steady history of photovoltaic metrics. The observed device stability, according to ISOS testing, opens the doors for certificating new PCE records by cobalt-based devices.

Sumário

O crescimento acelerado da Internet das Coisas (IoT) implica a instalação de biliões de sensores sem fio nas próximas décadas. Atualmente, tem-se tornado imperativo definir estratégias sustentáveis sem necessidade de ligação constante à corrente elétrica para fornecer energia a dispositivos IoT e a biliões de outros dispositivos de baixa potência. Energia fotovoltaica para uso interior (iPVs) tornou-se uma das opções mais promissoras para responder a este desafio. Em 2021, o mercado estimado para iPVs foi cerca de 10^9 dólares americanos, o que corresponde a centenas de milhões de unidades instaladas. Células solares sensibilizadas por corante (DSSCs) são uma das mais promissoras tecnologias iPVs, já que permite baixos custos de produção, arquitetura simples e versátil, baixo impacto ambiental, e ausência de toxicidade. O rendimento quântico de fotocorrente de uma DSSC é perfeitamente compatível com o espetro de emissão da maioria das lâmpadas de uso interior, o que permite obter eficiências de conversão de energia (PCE) elevadas; as DSSCs apresentam o recorde de PCE de 34.5 % perante uma intensidade de luz interior de 1000 lx. Recentemente, várias empresas iniciaram a produção comercial de DSSCs para aplicações interiores.

DSSCs em configuração monolítica (M-DSSCs) atraíram interesse tecnológico significativo. Estas células apenas usam um único substrato de óxido condutor transparente, o que permite uma redução de 20-30 % nos custos dos dispositivos, e torna a produção de módulos mais direta. A sua limitação é a baixa PCE em comparação com as DSSCs convencionais. Este problema está relacionado com a insuficiente absorção de luz causada pela baixa refletividade da camada isoladora, com resistência mais elevada à transferência de carga na interface camada isoladora/contra-elétrodo, com resistência mais elevada à difusão, com resistência em série mais elevada, e com fatores de preenchimento mais baixos. Esta tese responde a estas limitações, permitindo a produção de M-DSSCs eficientes, estáveis e com bom custo-benefício.

Em geral, a camada isoladora foi um dos componentes menos estudados das M-DSSCs. Neste trabalho, foram desenvolvidas camadas isoladoras de SiO_2, provenientes de formulações aquosas; 30 % (em massa) de nanopartículas de TiO_2 em SiO_2 aumentaram a refletância destas camadas isoladoras, o que resultou numa PCE recorde de 8.3 % (1 sol) para M-DSSC com eletrólito de iodo. Outra eficiência recorde foi alcançada neste trabalho ao desenvolver a primeira M-DSSC com eletrólito de cobalto. A energia de ativação aparente para a transferência de eletrões, a resistência à transferência de carga elétrica, e a densidade de corrente de troca de eletrões de diferentes materiais – nanopartículas de Pt, filme metálico de Pt, grafite/carbono, e PEDOT:PSS – em eletrólito de cobalto foram determinados para selecionar o catalisador mais favorável para a redução de $Co(III)(bpy)_3$. M-DSSCs compostas por eletrólito de cobalto, contra-elétrodo de carbono e camada isoladora de TiO_2 (rutilo) apresentaram eficiências de 9.5 % (1 sol) e cerca de 22 % (1000 lx, lâmpada LED). As

condições de sensibilização destas M-DSSCs, assim como a concentração de TBP no eletrólito de cobalto, foram analisadas para produzir células solares eficientes.

Finalmente, foram desenvolvidas as mais estáveis M-DSSCs com eletrólito de cobalto reportadas atualmente; foi implementado o processo de selagem baseado na fusão de vidro auxiliada por laser, o qual apresentou uma hermeticidade excecional. O perímetro de selagem e os furos para injeção de eletrólito foram ambos selados a vidro num processo auxiliado por laser. O teste padrão MIL-STD-883 (método 1014.10) foi realizado antes e após os ciclos de humidade referentes ao teste padrão IEC 61646, o que permitiu confirmar a hermeticidade e a robustez do encapsulamento. M-DSSCs seladas a vidro com eletrólito de cobalto à base de ACN passaram pela primeira vez em vários testes ISOS, nos quais se inclui ciclo térmico a 85 ºC, 1000 h de envelhecimento natural, e 1000 h de envelhecimento sob constante iluminação solar e artificial com carga passiva, o que resultou em estáveis parâmetros de caraterização fotovoltaica. De acordo com os testes ISOS, a estabilidade observada nestas células solares abre portas para a certificação de novos recordes de PCE em DSSCs com eletrólito de cobalto.

List of Abbreviations and Symbols

Variables	Definition	S.I. Units
A	Area	m^2
A_{CS}	Adsorbate cross-section area (A_{CS} = 16.2 Å^2 for N_2)	m^2
c_0	Speed of light ($c_0 = 3.0\times10^8$ m·s^{-1})	m·s^{-1}
C_μ	Chemical capacitance	F
E_a	Apparent activation energy	eV
E_g	Bandgap energy	J
f	Frequency	s^{-1}
F	Faraday constant (F = 96 500 C·mol^{-1})	C·mol^{-1}
h	Planck's constant ($h = 6.626\times10^{-34}$ m^2·kg·s^{-1})	m^2·kg·s^{-1}
I	Current	A
J_0	Exchange current density	A·m^{-2}
J_{inf}	Exchange current density at infinite temperature	A·m^{-2}
J_{MPP}	Current density at the maximum power point	A·m^{-2}
J_{SC}	Short-circuit current density	A·m^{-2}
L_o	Levi's diffusion element	Ω
m	Mass	kg
N	Avogadro's number ($N = 6.022\times10^{23}$ mol^{-1})	mol^{-1}
n	Number of electrons	
n_g	Specific amount of adsorbed gas at the relative pressure P/P_0	
n_m	Monolayer capacity of the adsorbed gas	
P	Pressure	Pa
P_0	Saturation pressure	Pa
P_{in}	Incident light power	W·m^{-2}

q	Elementary charge ($q = 1.602 \times 10^{-19}$ C)	C
R	Universal gas constant ($R = 8.314$ J·mol^{-1}·K^{-1})	J·mol^{-1}·K^{-1}
R_{CE}	Charge-transfer resistance at counter-electrode/electrolyte interface	Ω
R_{El}	Diffusion resistance in the electrolyte	Ω
R_K	Charge-transfer resistance at TiO_2/electrolyte interface	Ω
r_p	Pore diameter	m
r_k	Kelvin radius	m
R_S	Series resistance	Ω
R_{sh}	Shunt-resistance	Ω
T	Temperature	K
t	Time	s
V	Potential	V
V_{MPP}	Potential at the maximum power point	V
V_{OC}	Open-circuit potential	V
W_S	Warburg diffusion element	Ω
wt	Weight	
Z'	Real part of impedance	Ω
Z''	Imaginary part of impedance	Ω
Z_C	Impedance associated with a capacitor	Ω
Z_{CE}	Counter-electrode impedance	Ω
Z_d	Electrolyte impedance	Ω
Z_L	Impedance associated with an indutor	Ω
Z_{PE}	Photoanode impedance	Ω
Z_R	Impedance associated with a resistor	Ω

Greek Symbols	Definition	S.I. Units
θ	Phase shift	
λ	Wavelength	m
η_{abs}	Light-harvesting efficiency	%
η_{col}	Electron collection efficiency	%
η_{FF}	Fill factor	
η_{inj}	Electron injection efficiency	%
η_{PCE}	Power conversion efficiency	%
ω	Angular frequency	$rad \cdot s^{-1}$

Subscripts	Definition
CE	Counter-electrode
OC	Open-circuit
PE	Photoanode
S	Series
SC	Short-circuit
sh	Shunt

Abbreviations	Definition
ACN	Acetonitrile
AM	Air mass
BET	Brunauer-Emmett-Teller
BIPV	Building-integrated photovoltaics
BJH	Barrett-Joyner-Halenda
CDA	Chenodeoxycholic acid
CE	Counter-electrode
CPE_{CE}	Constant phase element associated with counter-electrode/electrolyte interface
CPE_{El}	Constant phase element associated with electrolyte diffusion
CPE_{K}	Constant phase element associated with TiO_2/electrolyte interface
DSSC	Dye-sensitized solar cell
EDS	Energy-dispersive X-ray spectroscopy
EIS	Electrochemical impedance spectroscopy
FF	Fill factor
FTO	Fluorine-doped tin oxide
GCB	Graphite/carbon-black
HOMO	Highest occupied molecular orbital
HPC	Hydroxypropyl cellulose
HTM	Hole transport material
IoT	Internet of Things
IPCE	Incident photon to current conversion efficiency
iPV	Indoor photovoltaics
ITO	Indium tin oxide

LED	Light-emitting diodes
LUMO	Lowest unoccupied molecular orbital
M-DSSC	Monolithic dye-sensitized solar cell
MPP	Maximum power point
NHE	Normal hydrogen electrode
NP	Nanoparticles
OSC	Organic solar cell
PCE	Power conversion efficiency
PE	Photoelectrode
PEDOT	Poly(3,4-ethylenedioxythiophene)
PEDOT:PSS	Poly(3,4-ethylenedioxythiophene) polystyrene sulfonate
PSC	Perovskite solar cell
Pt_{Met}	Platinum metal
Pt_{NP}	Platinum nanoparticles
PV	Photovoltaic
SEM	Scanning electron microscopy
Spiro-OMeTAD	2,2',7,7'-tetrakis(N,N-di-p-methoxyphenyl-amine)9, 9' spirobifluorene
SSA	Specific surface area
TBP	4-*tert*-butylpyridine
TCO	Transparent conductive oxide
UV	Ultraviolet
XRD	X-ray diffraction

CHAPTER 1

INTRODUCTION

Under peer-revision in *Materials and Today Communications* journal.

1

Introduction

The World is facing an increasing energy demand, derived from the faster population and economic growth observed in the last decades, especially in non-OECD (Organisation for Economic Co-Operation and Development) countries. The projections from International Energy Outlook 2021 estimate that world energy consumption will be kept increasing until 2050 (**Fig. 1.1a**). Nowadays, fossil fuels are still the major energy source, which contributes considerably to greenhouse gas emissions. Since the oil reserves are finite, it is expected that the oil price will increase considerably in the next decades. Besides, the environmental impact caused by the combustion of fossil fuels has been attracted a lot of attention, especially by the youngest generations. Thereby, the governmental entities have been giving financial incentives for the development of technologies for harvesting energy from sustainable and renewable sources. According to the International Energy Outlook 2021, solar energy is expected to be the major energy source in 2050, surpassing even coal and natural gas (**Fig. 1.1b**) [1].

a) b)

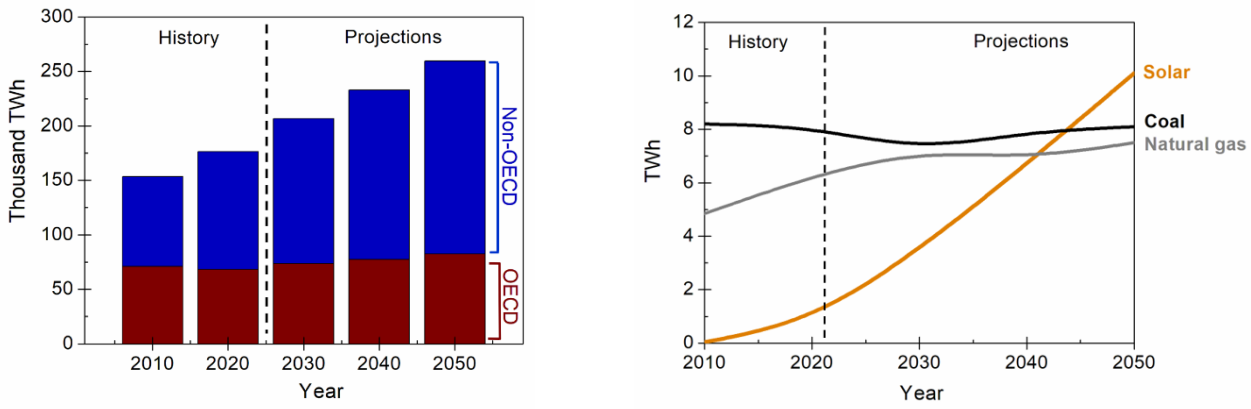

Fig. 1.1 – World energy consumption in thousand TWh ***(a)***, world energy generation from different sources in TWh range ***(b)*** (adapted from the International Energy Outlook 2021 [1]).

Countries such as Portugal, which present pleasant sunshine even in the winter season, are very attractive for the generation of electricity from the sunlight. The silicon solar panels are still the dominant photovoltaic (PV) devices in the market, with a power conversion efficiency (PCE) of 26.7 % recorded at laboratory-scale [2], and with a developed production process, which has been reducing the price of these panels along the years. Yet, these systems present high manufacturing costs and energy-demanding purification processes.

Another huge energy challenge that emerged quite recently is the exponential increase of low-power electronic devices of the Internet of Things (IoT). The estimated market of indoor photovoltaic (iPV) devices is *ca.* 10^9 USD in 2021, corresponding to *ca.* 100 million units (**Fig. 1.2a**). Building-integrated photovoltaics (BIPV) is still the dominant market for PV technologies, but continuous growth is expected in iPV market for the coming years [3], as depicted in **Fig. 1.2b**.

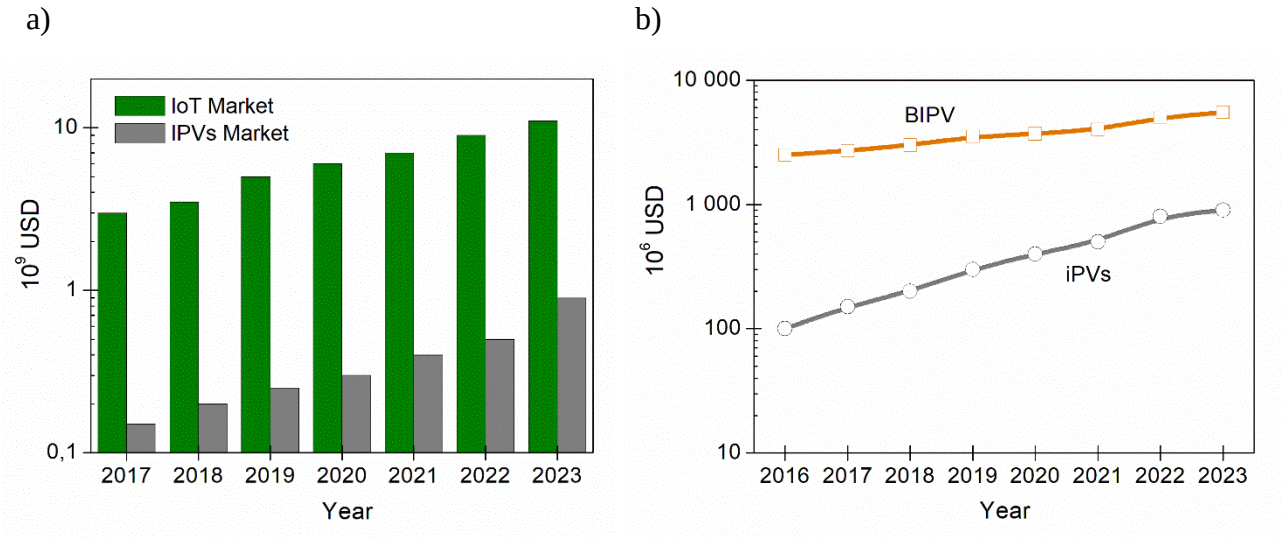

Fig. 1.2 – The estimated market size (in 10^9 of USD) of IoT and iPV devices ***(a)***, the estimated market size (in 10^6 of USD) of BIPV and iPV technologies ***(b)*** (adapted from [3]).

Despite silicon solar panels being the dominant PV technology on the market, the high production costs and energy demand purification processes boosted the research for low-cost alternatives, the third-generation PV technologies, such as dye-sensitized solar cells (DSSCs), perovskite solar cells (PSCs), and organic solar cells (OSCs). Some advantages of these PV devices include their transparency and nice appearance, the possibility to be built in flexible and lightweight substrates, and the decent PCE under full sunlight and low-light intensities [4]. The history of record PCEs under 1-sun simulated solar light (AM1.5G, 1000 $W \cdot m^{-2}$) for DSSCs, PSCs, and OSCs are displayed in **Fig. 1.3a**. DSSCs have been battling during the last decades to improve their PCE; even with the emergence of metal coordination complexes as redox mediators, the highest certified PCE for liquid-junction DSSCs is 13.0 % [5]. Unlikely DSSCs, PSCs and OSCs present considerably higher PCEs; OSCs already recorded a PCE of 18.2 %, while PSCs reached 25.7 %, very close to the

maximum efficiency defined by the Shockley-Queisser limit [6].

a) b)

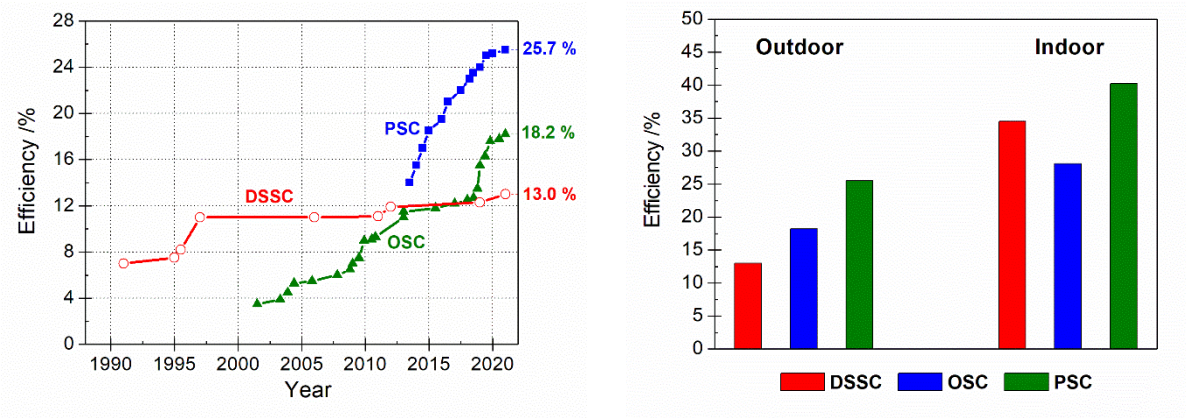

Fig. 1.3 – History of PCEs (extracted from Best Research-Cell Efficiencies Chart of NREL) [5] ***(a)***, highest certified PCEs (outdoor) [5] and highest reported PCEs (indoor) [7-9] ***(b)*** for DSSCs, PSCs and OSCs.

Under full sunlight, PSCs and OSCs outperformed DSSCs. However, the same is not observed for indoor artificial illumination, as **Fig. 1.3b** shows. OSCs reached a PCE of 28.1 % under 1000 lx light intensity [8], while PSCs achieved 40.2 % in devices employing Pb [9], which requires an effective encapsulation of the devices to prevent leakage. Most of the reports considering PCEs above 30 % under low-light intensities belong to DSSCs, where their record PCE nowadays is 34.5 % [7]. It is relevant to mention that standards for indoor light sources were not defined so far. Nonetheless, the efficient harvesting of artificial low-intensity light and diffuse light, together with the low cost, versatility, and non-toxicity, turn DSSCs probably the most attractive third PV technology to power small indoor electronic devices [10,11].

DSSCs were first reported in 1991 by O'Regan and Grätzel; the first device was made of a semiconductor mesoporous layer made of TiO_2 nanoparticles (NP) sensitized with a ruthenium complex. The high surface area of the TiO_2 electrode allowed the absorption of 46 % of incident light by the ruthenium dye, and this seminal device reported a photon to current conversion efficiency (IPCE) of 80 %, displaying a PCE of 7.1 % under simulated solar light [12]. The photoanode and the cathode of the original device were deposited in opposite transparent conductive oxide (TCO) substrates, and the microgap between the electrodes was filled with an electrolyte, as illustrated in **Fig. 1.4a**. A few years later, an alternative device arrangement was proposed by Kay and Grätzel – the monolithic configuration. In the monolithic configuration, the mesoporous TiO_2-anatase photoanode and a carbon-based counter-electrode (CE) were placed in the same conductive substrate, being electrically separated by a porous TiO_2-rutile insulating/spacer layer, and physically by a

groove in the TCO glass. The cell was assembled using a non-conductive top glass, and the electrolyte was injected by vacuum filling through pre-drilled holes on the top glass (**Fig. 1.4b**). This new design rendered a PCE of 6.7 % [13].

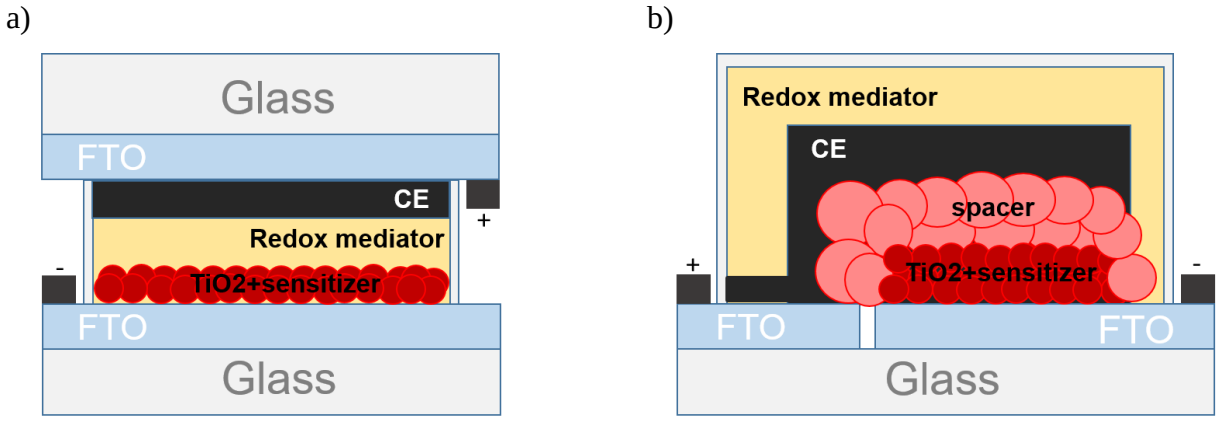

Fig. 1.4 – Structure of DSSCs in conventional configuration ***(a)*** and in monolithic configuration ***(b)***.

What is so attractive in the monolithic design is the reduction of 20-30 % in materials costs [14] just by using only one TCO-coated glass substrate, besides being more straightforward fabricating in-series modules [13;15-17] and fabricating in flexible substrates [18,19]. Monolithic dye-sensitized solar cells (M-DSSCs) are typically less efficient than their conventional counterparts, which could contribute to a considerably small number of works published with this configuration. While the highest reported PCE for a DSSC is 14.3 % under 1-sun simulated solar light [20], the best performing M-DSSC rendered a PCE of 9.5 % [21]. The smaller PCE is often attributed to a higher charge transfer resistance at the spacer layer/counter-electrode interface, essentially related to three factors: higher mass transport/electrical resistance of the electrolyte through the spacer layer; inefficient reduction of the oxidized species of the redox mediator; and insufficient light harvesting due to poorer reflectivity of the spacer layer [22-25]. When carbon-based counter-electrodes are used, high series resistance typically emerged, apart from low fill factors [22-25]. Under indoor illumination, the lack of information does not allow to withdraw of a similar conclusion concerning the PCE of a DSSC *vs* a M-DSSC devices; PCEs higher than 30 % have been reported for conventional DSSCs under indoor illumination [7,26], but, surprisingly, little attention was paid to the characterization of M-DSSCs under the same light conditions. In the 2000s was reported for the first time the performance of M-DSSCs modules under indoor illumination, but without presenting the spectra or the irradiance of the lamps. Therefore, the performance was evaluated essentially using the maximum power delivered by the devices [27-29]. Recently, in 2021, a decent PCE of 22 % was reported by the authors under 1000 lx indoor illumination [21].

This chapter reviews the M-DSSC developments since 1996, when it was first reported. Since

the monolithic structure is very appellative for emerging efficient solid-state DSSCs devices, a subsection is reserved for this topic. The limitations beyond efficiency, such as the flexibility and the transparency of these devices, are discussed along with the chapter. Only a few works are published annually on M-DSSCs, and the last one on M-DSSC modules was published in 2012. Therefore, the final goal of this review chapter is to discuss strategies to overcome the weaknesses of the monolithically assembled devices, and to contribute to the renaissance of this DSSC configuration.

1.1 Working Principle and Characterization of DSSCs

In this section, the working principle of DSSCs, as well as the most used characterization techniques to evaluate the performance of the solar cells, are discussed.

1.1.1 Device working principle

Dye-sensitized solar cells present a working principle similar to natural photosynthesis (**Fig. 1.5**); upon illumination, the sensitizer molecules absorb a photon, which causes the excitation of an electron from the highest occupied molecular orbital (HOMO) to the lowest unoccupied molecular orbital (LUMO). This electron is then injected into the TiO_2 conduction band. In this process, the sensitizer gets oxidized, being regenerated by taking an electron from the redox mediator. After diffusion towards the conductive substrate and travel through the external circuit, the electron is collected at the counter-electrode interface and used to reduce the redox mediator, completing thereby the cycle. The performance of a DSSC can be negatively affected by the recombination of the injected electron with the oxidized sensitizer or oxidized redox mediator [30-32].

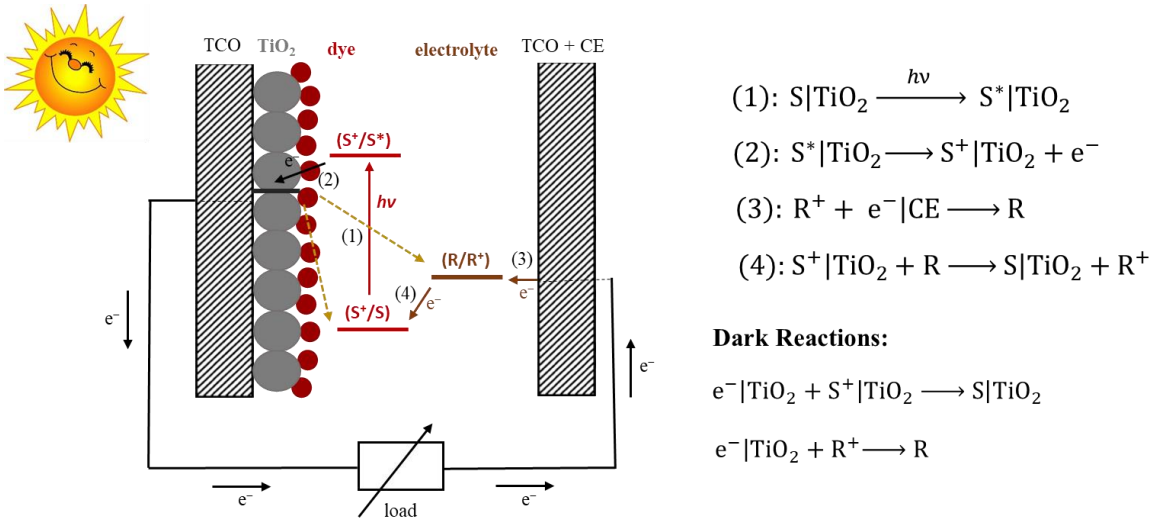

Fig. 1.5 – Schematic representation on the working principle of DSSCs: (1) photon absorption; (2) electron injection; (3) electrolyte regeneration; (4) sensitizer regeneration.

1.1.2 Characterization parameters

The performance of DSSCs is commonly evaluated based on its current-potential (*J-V*) characteristic, and therefore by determination of the *J-V* parameters: the short-circuit current (J_{SC}), the open-circuit potential (V_{OC}), the maximum power output (MPP), the fill factor (FF) and the power conversion efficiency (PCE). J_{SC} depends essentially on the light-harvesting efficiency of the sensitizers, on the electron injection efficiency into the semiconductor conduction band edge, and on the electron collection efficiency [33]. Hence, the photocurrent is influenced, among other factors, by the surface area of the photoanode, the LUMO level and the extinction coefficient of the sensitizer, the bandgap of the semiconductor, and the recombination of the injected electron with oxidized dye or oxidized specie of the redox mediator. In turn, V_{OC} is determined by the energy difference between the quasi-Fermi level of the electrons in the semiconductor and the redox potential of the redox couple [33]. So, the V_{OC} of the devices could be enhanced by shifting the Fermi-level towards more negative potentials or by using redox mediators with higher redox potentials. The MPP can be calculated simply by considering the maximum product of the photocurrent (J_{MPP}) and the photopotential (V_{MPP}) reached by the DSSC. The FF is the ratio between the MPP and the product between V_{OC} and J_{SC}. Finally, the PCE shows the fraction of incident light power (P_{in}) that is converted into electrical. A typical *J-V* curve, as well as the equations to determine MPP, FF and PCE are indicated in **Fig. 1.6**.

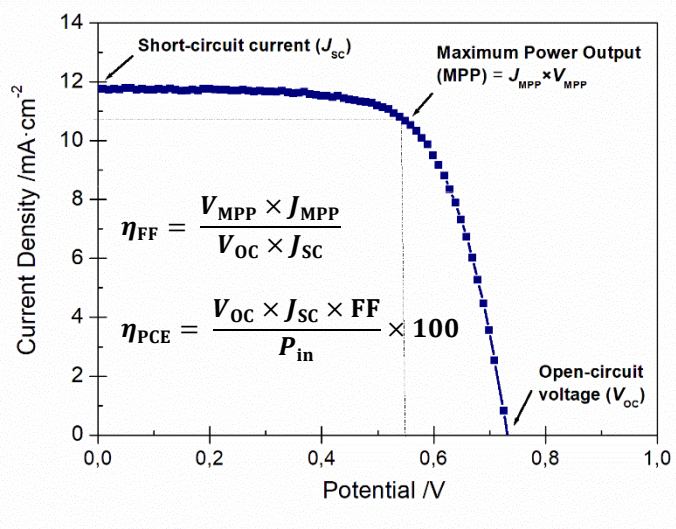

Fig. 1.6 – *J-V* characteristics of a DSSC and equations to determine the MPP, FF and PCE.

1.1.3 Determination of the internal resistances by Electrochemical Impedance Spectroscopy (EIS)

Electrochemical impedance spectroscopy (EIS) is a powerful technique to characterise the charge transfer and accumulation happening in electrochemical systems [34,35]. A small-signal sinusoidal potential $V(\omega, t) = V_0 \times \sin(\omega t)$ with amplitude V_0 is applied to the system, and the

corresponding current $I(\omega, t)$ is measured; the analysis is performed in a wide range of frequencies f ($f = \omega/2\pi$). The current $I(\omega, t)$ with amplitude I_0 is given by $I(\omega, t) = I_0 \times \sin(\omega t - \theta)$, being ω the angular frequency, t the time and θ the phase shift. The impedance $Z(\omega, t)$ is given by Ohm's law:

$$Z(\omega, t) = \frac{V(\omega, t)}{I(\omega, t)} \tag{1.1}$$

The potential $V(\omega, t)$ and the current $I(\omega, t)$ could be described as complex functions: $V(\omega, t) = V_0 \times e^{i \cdot w \cdot t}$ and $I(\omega, t) = I_0 \times e^{i \cdot (w \cdot t - \theta)}$, respectively, where i is the imaginary unit. Therefore, the impedance $Z(\omega, t)$ could be expressed as:

$$Z(\omega, t) = \frac{V_0}{I_0} \times e^{i \cdot \theta} = |Z(\omega)| \times e^{i \cdot \theta} \tag{1.2}$$

being $|Z(\omega)|$ the impedance modulus.

Introducing the Euler's formula [$e^{i \cdot \theta} = \cos\theta + i \times \sin\theta$]:

$$Z(\omega, t) = |Z(\omega)| \times (\cos\theta + i \times \sin\theta) = Z'(\omega) + i \times Z''(\omega) \tag{1.3}$$

where $Z' = |Z(\omega)| \times \cos\theta$ is the real part of the impedance, and $Z'' = |Z(\omega)| \times \sin\theta$ is the imaginary part.

The phase shift θ and the impedance modulus $|Z(\omega)|$ are given by:

$$\theta(\omega) = \tan^{-1}\left(\frac{Z''(\omega)}{Z'(\omega)}\right) \tag{1.4}$$

$$|Z(\omega)| = \sqrt{Z'^2(\omega) + Z''^2(\omega)} \tag{1.5}$$

The electric circuits are essentially composed of three electrical elements: the resistors, the capacitors and the inductors. The impedance associated with the resistor $Z_R(\omega, t)$ is given by Ohm's law, **eq. (1.1)**. The current $I(\omega, t)$ is in phase with the potential stimulus ($\theta = 0$). Therefore, the $Z_R(\omega, t)$ is given by the resistance R:

$$Z_R(\omega, t) = \frac{V(\omega, t)}{I(\omega, t)} = \frac{V_0}{I_0} = R \tag{1.6}$$

The current associated with a capacitor C is given by $I(t) = C \times \frac{dV(t)}{dt}$. Considering a sinusoidal potential $V(\omega, t)$, the correspondent current $I(\omega, t)$ is out of phase ($\theta = -\pi/2$):

$$I(\omega, t) = C \times \frac{dV(\omega, t)}{dt} = C \times \omega \times V_0 \times \cos(\omega t) = C \times \omega \times V_0 \times \sin(\omega t + \pi/2) = I_0 \times \sin(\omega t + \pi/2) \tag{1.7}$$

Therefore, the impedance associated with the capacitor $Z_C(\omega, t)$ is determined by:

$$Z_C(\omega, t) = \frac{V(\omega, t)}{I(\omega, t)} = \frac{V_0}{I_0} \times e^{i \cdot \theta} = \frac{1}{\omega \times C} \times e^{-i \cdot \pi/2} = \frac{1}{i \times \omega \times C} \tag{1.8}$$

The ideal capacitors *C* are often replaced by constant phase elements (CPE). The impedance associated with a CPE (Z_Q) is given by **eq. (1.9)**, where *Q* is the CPE prefactor and β is the CPE index. β presents a value between 0 and 1; when β=1, the CPE performs like a capacitor. The CPE shows an angle phase of $-\beta\pi/2$ [34].

$$Z_Q(\omega, t) = \frac{V(\omega, t)}{I(\omega, t)} = \frac{1}{(i\times\omega)^{\beta}\times Q} \tag{1.9}$$

The potential associated with an inductor *L* is given by $V(t) = L\times\frac{dI(t)}{dt}$. The impedance associated with an inductor $Z_L(\omega, t)$ is expressed by **eq. (1.10)**, being the phase shift of $\pi/2$:

$$Z_L(\omega, t) = \frac{V(\omega, t)}{I(\omega, t)} = \frac{V_0}{I_0} \times e^{i\cdot\theta} = \omega \times L \times e^{i\cdot\pi/2} = i \times \omega \times L \tag{1.10}$$

The impedance data is often analysed plotting $-Z''$ as a function of Z', which is referred to as the Nyquist plot. The Nyquist plot of a DSSC normally originates three semi-circles, as displayed in **Fig. 7a**. The semi-circle of the Nyquist plot recorded at higher frequencies gives information about the charge transfer resistance at the counter-electrode/electrolyte interface (R_{CE}); the intermediate semi-circle relates both with the resistance of the electron transport in the TiO_2 mesoporous layer and the recombination resistance at the TiO_2/electrolyte interface (R_K); finally, at lower frequencies, is visible a third semi-circle associated with the diffusion resistance of charge carriers in the electrolyte (R_{EI}). The series resistance, R_S, corresponds to the onset of the Nyquist plot at high frequencies. This resistance is associated with the resistance of the TCO-coated substrate and of the electrical contacts [34,35]. Since the frequency *f* is hidden in the Nyquist plots, the Bode plots log |Z| *vs f* and $-\theta$ *vs f* are used as a complement (**Fig. 1.7b**).

a) b)

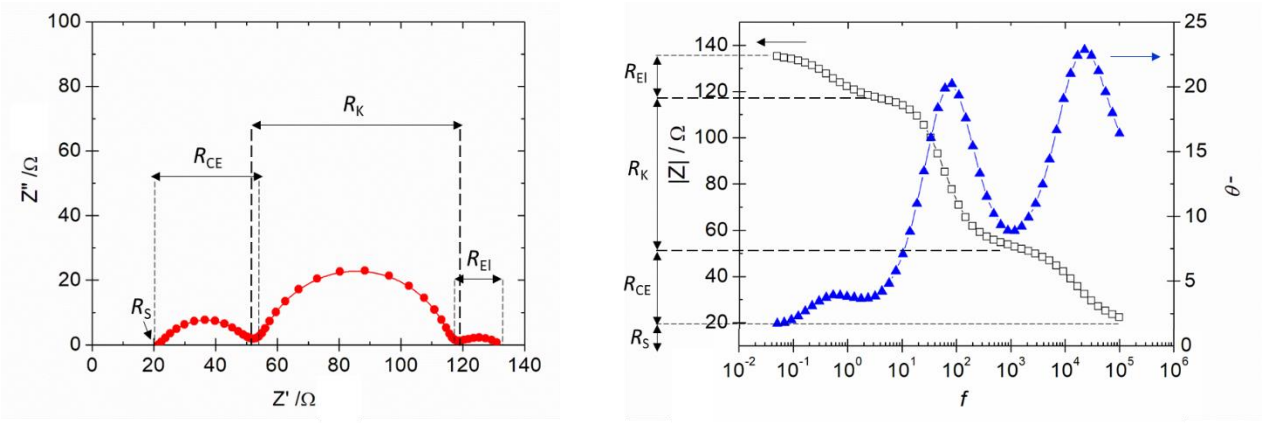

Fig. 1.7 – Typical Nyquist plot (***a***) and Bode plot (***b***) for DSSCs (adapted from [34]).

The impedance spectra of DSSCs are commonly fitted using a transmission line model [36-38]. The simplified transmission line model is displayed in **Fig. 1.8**. This simplification is valid when the

recombination at TCO/electrolyte interface ($R_{ct_{TCO}}$) and the contact resistance between TCO and TiO_2 (R_{TCO}) are both negligible compared with the remaining resistances of the devices [34]. In consequence, the total impedance Z of a device could be calculated using **eq. (1.11)**, where R_S is the ohmic series resistance, Z_{PE} is the photoanode impedance, Z_d is the electrolyte impedance and Z_{CE} is the counter-electrode impedance:

$$Z = R_S + Z_{PE} + Z_d + Z_{CE} \tag{1.11}$$

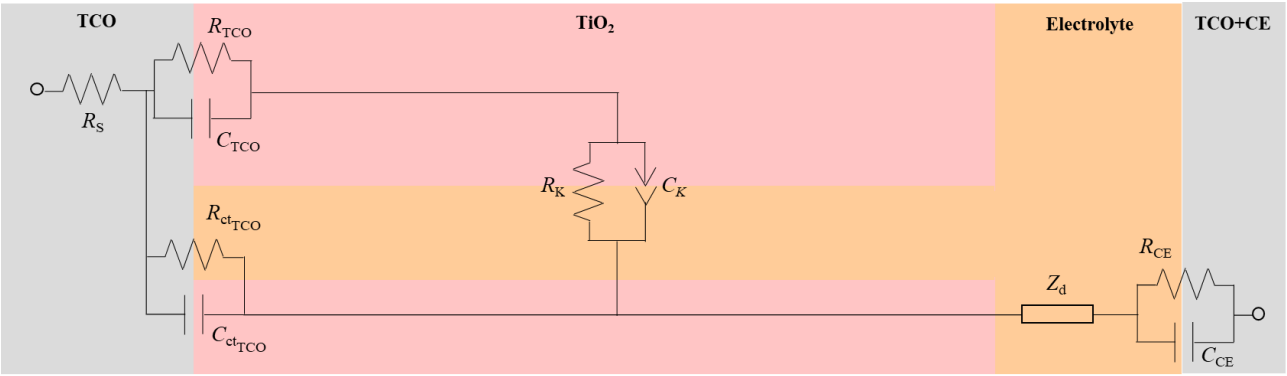

- R_S: Ohmic series resistance
- R_{TCO}: Substrate contact resistance at TCO/TiO_2 interface
- C_{TCO}: Substrate contact capacitance at TCO/TiO_2 interface
- $R_{ct_{TCO}}$: Substrate charge transfer resistance for the electron recombination from the uncovered layer of the TCO to the electrolyte
- $C_{ct_{TCO}}$: Substrate charge transfer capacitance for the electron recombination from the uncovered layer of the TCO to the electrolyte
- R_K: Electron transport resistance in TiO_2 layer and charge transfer resistance at TiO_2/electrolyte interface
- C_K: Photoanode chemical capacitance
- Z_d: Diffusion impedance of charge carriers in the electrolyte
- R_{CE}: Charge transfer resistance at counter-electrode/electrolyte interface
- C_{CE}: Charge transfer capacitance at counter-electrode/electrolyte interface

Fig. 1.8 – Simplified transmission line model (adapted from [38]).

Several equivalent circuits can be used to fit the impedance spectra of DSSCs [34,35], allowing the determination of the charge transfer resistances of the devices. There is a lack of information on charge transfer of M-DSSCs, with only a few works reporting the impedance spectra of monolithic assembled devices and the corresponding equivalent circuits [18,21,24,39,40]. Among them, the most common is shown in **Fig. 1.9a** [21,24,39], displaying three semi-circles associated with R_{CE}, $R_{K,}$ and R_{El}; CPE_{CE}, CPE_K and CPE_{El} are the constant phase elements associated with counter-electrode/electrolyte interface, TiO_2/electrolyte interface, and diffusion of charge carriers diffusion in the electrolyte, respectively. R_{El} is caused by an electrolyte diffusion resistance through the spacer layer and the thick counter-electrode [18,21,24,39], which one is usually made of

carbonaceous materials [21,39]. When thin metal film is used as counter-electrode, the electrolyte diffusion is sometimes negligible [40], resulting in two semi-circles associated with R_{CE} and R_K (**Fig. 1.9b**).

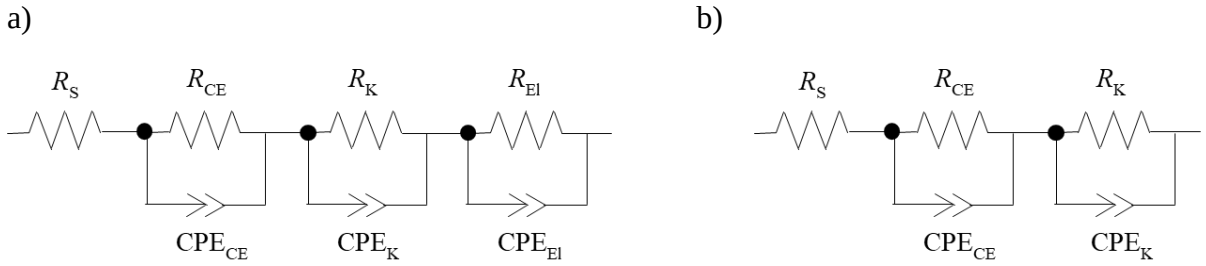

Fig. 1.9 – Typical equivalent circuits for M-DSSCs.

1.1.4 Photocurrent yield measurements

The incident photon to current conversion efficiency (IPCE) is another useful technique to evaluate the performance of solar cells. The IPCE is expressed by the percentage of the incident photons ($N_{photons}$) that are converted into electrons ($N_{electrons}$) at a given wavelength λ under monochromatic light irradiation [41,42]:

$$\mathrm{IPCE}(\lambda) = \frac{N_{\mathrm{electrons}}}{N_{\mathrm{photons}}} \tag{1.12}$$

The IPCE could also be defined as a function of the light-harvesting efficiency (η_{abs}), the electron injection efficiency into the semiconductor conduction band edge (η_{inj}), and the charge collection efficiency of the devices (η_{col}) [41,42].

$$\mathrm{IPCE}(\lambda) = \eta_{\mathrm{abs}}(\lambda) \times \eta_{\mathrm{inj}}(\lambda) \times \eta_{\mathrm{col}}(\lambda) \tag{1.13}$$

The number of photogenerated electrons flowing in the external circuit can be correlated with the short-circuit current J_{SC} by **eq. (1.14)**, where q is the elementary charge and t is the time.

$$J_{SC} = \frac{q \times N_{\mathrm{electrons}}}{t} \tag{1.14}$$

The number of incident photons can be determined by measuring the power of the IPCE monochromator at each wavelength, and correlates with the power of incident light (P_{in}) by the **eq. (1.15)**:

$$P_{\mathrm{in}} = \frac{N_{\mathrm{photons}}}{t} \times h \times f = \frac{N_{\mathrm{photons}}}{t} \times h \times \frac{c_0}{\lambda} \tag{1.15}$$

where h is the Planck's constant (6.626068×10^{-34} $m^2 \cdot kg \cdot s^{-1}$), f is the frequency and c_0 is the speed of light (3.0×10^8 $m \cdot s^{-1}$).

By replacing **eq. (1.14)** and **eq. (1.15)** on **eq. (1.12)** is attained the following equation [41,42]:

$$\text{IPCE}\ (\lambda) = \frac{1240 \times J_{SC}}{\lambda \times P_{in}} \times 100\ \% \qquad (1.16)$$

A typical IPCE spectra of a DSSC is plotted in **Fig. 1.10**.

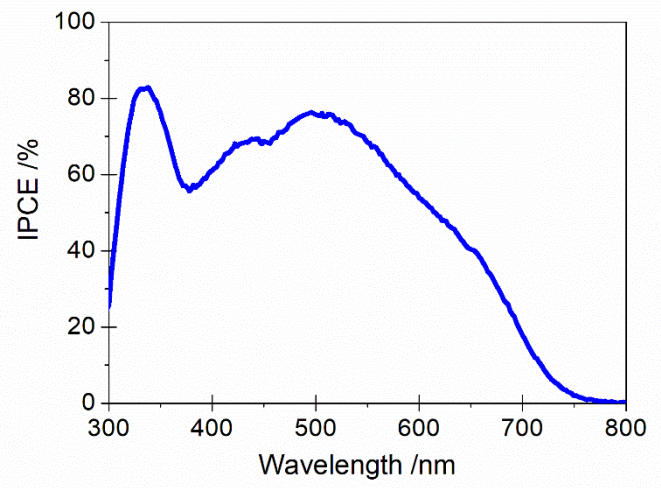

Fig. 1.10 – Typical IPCE spectra of a DSSC (adapted from [41]).

1.2 Laboratory-scale Monolithic Dye-Sensitized Solar Cells

M-DSSCs differ from their conventional counterparts mainly owing to the electrical spacer layer. Therefore, it is important to understand the impact that this additional layer could have on the performance of the devices. Besides, both the insulating layer and the counter-electrode must be composed of porous materials, unlike the conventional DSSCs. This triple-layer structure (photoanode, spacer layer and counter-electrode) increases the total thickness of the monolithic devices, which could require a distinct sensitization time or electrolyte composition. All these factors will be addressed in the next subsections.

1.2.1 Counter-electrode layer

The counter-electrode collects the electrons that arrived from the external circuit, and reduces the oxidized species of the redox mediator; the counter-electrode must have high electrical conductivity and good catalytic activity of charge transfer with the redox mediator. Besides, the counter-electrode should be chemical and electrochemically stable in the electrolyte [43,44]. Platinum was for a long time the preferable counter-electrode for iodide-mediated devices. However, the high cost of this material drove the research for cost-effective alternatives, like conducting polymers, carbonaceous materials or metal oxides [43,44]. In the monolithic configuration, the DSSC counter-electrode must have pores large enough to allow the diffusion of the redox mediator through the triple-layer structure and the dye at the TiO_2 mesoporous layer. For these reasons, carbonaceous

materials, like graphite and carbon-black, are the most used counter-electrodes on M-DSSCs [13].

In 1996, in the first published work on M-DSSCs, Kay and Grätzel [13] reported a 6.7 % efficient M-DSSC employing a counter-electrode composed of a mixture of graphite powder and carbon-black to enhance the conductivity and catalytic activity, respectively. A drawback of carbon counter-electrodes is the poor adhesion to the TCO-coated glass substrate and then a high electronic contact resistance. For mitigating this shortcoming, the authors added a small amount of TiO_2 to the carbon layer, to avoid cracks and to increase the adhesion both to the spacer layer and to the TCO substrate [13]. Since then, several approaches were considered to increase the performance of M-DSSCs. In 2012, Liu *et al*. [22] developed a platinized graphite/carbon-black counter-electrode, which enhanced the charge transfer and the catalytic activity in comparison with a pure carbon counter-electrode. Besides, using only 0.5 % Pt loading in the carbon-electrode, the authors achieved a PCE of 7.6 %. One year later, Vesce *et al*. [45] prepared a lab-made counter-electrode composed of graphite powder and carbon-black with the addition of a small amount of TiO_2. These authors used a thicker layer (~120 μm) to increase the catalytic activity of the counter-electrode and to reduce both R_{CE} and R_S. However, the best performing device displayed a PCE of 4.9 %. A similar strategy was proposed by Ito and Takahashi (2012) [39]; TiO_2 nanopowder was added to the carbon paste to prevent cracking and peeling-out, which contributed to a stable device operating at 80 ºC for 1000 h. Thompson *et al*. (2013) [25] used poly (3,4-ethenedioxythiophene) (PEDOT) applied by electrodeposition on top of carbon layer counter-electrode. This composite counter-electrode decreased the electrical resistivity of the devices and enhanced the fill factor, allowing a PCE of 5.2 %. However, since these authors improved the mechanical stability of the counter-electrode, the relevant advantage here was the possibility to apply them in flexible substrates.

A very innovative approach was proposed by Kwon *et al*. in 2013 [23]. These authors combined a macroporous polymer spacer layer with a PEDOT layer counter-electrode, obtaining a PCE of 7.7 %. Since both layers are made of polymers, this configuration is also very promising for flexible devices. Fu *et al*. (2013) [18] prepared M-DSSCs on flexible metal substrates; these authors used two coplanar charge collecting electrodes (such as Ti foils) separated by a ZrO_2 spacer layer, and eliminated the need for TCO substrates, having achieved a PCE of 4.2 % in completely TCO-free device. An 8.0 % efficient M-DSSC device was reported by Behrouznejad *et al.* (2018) [24], using a counter-electrode composed of electrodeposited Cr and Pt nanoparticles on a metal foil. This alternative decreases the R_S of the devices and requires a smaller amount of the catalyst. All these works, assessing different counter-electrodes, are summarized in **Table 1.1**.

1.2.2 Electrical spacer layer

In M-DSSCs, the main function of the spacer layer is to electrically separate the photoanode from the counter-electrode. If the spacer layer is made of large particles (>200 nm) with a high refractive index, it could play a role as a scattering layer, by reflecting light not absorbed back to the photoelectrode. The spacer must be porous to let the electrolyte charge carriers to diffuse all through to the TiO_2 mesoporous layer [13]. Despite the impact that the spacer layer can have on the performance of M-DSSCs, only few works gave attention to it.

Thompson *et al*. (2010) [46] evaluated the role of the spacer layer in M-DSSCs. These authors prepared M-DSSCs without spacer layer (which means direct contact between photoanode and counter-electrode), and others with a TiO_2 and a ZrO_2 spacer layer. The highest PCE, 5.1 %, was recorded in the M-DSSCs with a ZrO_2 spacer layer. The devices using a TiO_2 spacer presented a PCE of 4.3 %, while the ones without any spacer layer produced a PCE of 3.2 %. These results show that M-DSSCs can work without a spacer layer but underperforms; the spacer layer prevents the direct percolation of electrons from the TiO_2 mesoporous layer to the counter-electrode, which increases the electron lifetime and enhances the performance of the devices. These results agreed with the ones reported by Hinsch *et al.* in 1998 [47].

Vesce *et al*. (2013) [45] analysed the effect of the spacer layer thickness in the performance of M-DSSCs. The optimum thickness is the one that enhances the light harvesting of the photoanode and increases the shunt resistance, without significantly increasing the charge transfer resistance at the spacer layer/counter-electrode interface and the diffusion resistance of the charge carriers in the electrolyte. The M-DSSCs using a 15 μm-thick ZrO_2/TiO_2-rutile spacer layer presented the highest J_{SC}, V_{OC}, FF and PCE; above 16 μm, the layer cracked after sintering.

Behrouznejad *et al.* (2018) [24] evaluated the performance of M-DSSCs with SiO_2, TiO_2 and Al_2O_3 spacer layers. The highest photocurrent was achieved in M-DSSCs using a TiO_2 spacer layer, which was assigned to the higher refractive index of TiO_2, especially in the rutile-phase. The lowest shunt-resistances was observed for the M-DSSCs with a TiO_2-SiO_2 spacer layer, which indicates percolation of electrons from photoanode to counter-electrode. Therefore, these authors used a SiO_2 shell around TiO_2 particles (TiO_2@SiO_2) to properly isolate the electrodes. TiO_2 particles with an average size of 300-400 nm was used to enhance the light harvesting of the devices. M-DSSCs with a TiO_2@SiO_2 spacer layer delivered a PCE of 6.1 % in the first experiment. Further optimization of the counter-electrode layer resulted in a PCE of 8.0 %.

The spacer layers typically use a high fraction of volatile organics (~60–70 wt.%); compounds such terpineol, acetic acid or ethanol are presented in the composition of commercial ZrO_2 and Al_2O_3 pastes, and even in lab-made SiO_2/TiO_2/ZrO_2/Al_2O_3 spacer layers. Santos *et al.* (2019) [40] prepared silica-based spacer layers, derived entirely from water-based formulations. The reflectance of these

Table 1.1

M-DSSCs employing different electrical spacer layers and counter-electrodes.

Year	Spacer layer	Counter-electrode	Sensitizer	Electrolyte	Active area	PCE /%	ref
1996	TiO_2-rutile/ZrO_2 (9:1)	Graphite/carbon-black/TiO_2	N3	I_3^-/I^- a)	0.40 cm^2	6.7	[13]
1998	Metal oxide	Graphite/carbon-black	N3	I_3^-/I^- a)	1 cm^2	*ca.* 2-3 (100-350 $W \cdot m^{-2}$) b)	[47]
2007	ZrO_2	Activated carbon + platinized activated carbon	N3	BMII/I_2 a) PMII/I_2 in BMII	0.50 cm^2	6.8 3.0	[49]
2007	ZrO_2	Activated carbon + platinized activated carbon	N3	I^-/IBr_2^- a)	0.50 cm^2	6.4	[50]
2008	ZrO_2	Graphite/carbon-black	N719	MHII/I_2 a) I_2 in EMIOTf/PMII	0.40 cm^2	5.8 2.7	[52]
2010	ZrO_2	Activated carbon + platinized activated carbon	N719	[MeBuIM]I/I_2 in [MeBuIM]SCN	0.48 cm^2	5.6 (250 $W \cdot m^{-2}$) 2.2 (1000 $W \cdot m^{-2}$)	[53]
2010	ZrO_2	Graphite	N719, 24 h	I_3^-/I^- a)	0.16 cm^2	5.1	[46]
2012	ZrO_2	Graphite/carbon-black + PEDOT	N719, 48 h	I_3^-/I^- a)	0.16 cm^2	5.2	[25]
2012	TiO_2/ZrO_2	Platinized graphite/carbon-black	N719	I_3^-/I^- a)	0.13 cm^2	7.6	[22]
2013	ZrO_2	Platinized CE on Ti foil	N719, 20-24 h	I_3^-/I^- a)	0.16 cm^2	4.2	[18]
2013	TiO_2-rutile/ZrO_2 (3:1)	Graphite/carbon-black/TiO_2	N719, 8 h	I_3^-/I^- a)	0.49 cm^2	4.9	[45]
2013	Polyethylene membrane	PEDOT	N719	I_3^-/I^- a)	0.64 cm^2	7.7	[23]
2018	TiO_2-rutile/SiO_2 (15:2)	Cr film + Pt NP on Ni foil	N719, 20 h	I_3^-/I^- a)	0.16 cm^2	8.0	[24]
2019	SiO_2-TiO_2 (7:3)	Platinum metal	N719	I_3^-/I^- a)	0.07 cm^2	8.3	[40]
2021	TiO_2-reflector	Graphite/carbon-black	YD2-*o*-C8	Co(III)/(II)$(bpy)_3$ a)	0.07 cm^2	9.5	[21]

a) dissolved in organic solvents; b) extracted from the *J-V* curve.

spacers was improved, not compromising the percolation of electrons, by adding 30 wt.% of TiO_2-anatase nanoparticles, rendering a M-DSSC device with a PCE of 8.3 %. The works concerning the effect of the spacer layer in M-DSSCs are summarized in **Table 1.1**.

1.2.3 Electrolyte solution

Most of the works concerning M-DSSCs use iodide-based electrolytes with volatile organic solvents [13,18,22-25,39,40,45,46]. The ionic liquids are an alternative for the organic solvents, since they are electrochemical stables, present good solvent properties, and are non-volatile [48]. In 2007, Petterson *et al.* [49] subjected M-DSSCs to aging tests using different electrolytes. The M-DSSCs employing an electrolyte composed of 1-butyl-3-methylimidazolium iodide (BMII)/I_2 in γ-butyrolactone showed an average initial PCE of 6.5 % under 1-sun illumination, but the degradation of 20 % after 45 days under continuous illumination at 350 $W \cdot m^2$ delivered by a sodium lamp. Under the same aging conditions, M-DSSCs using an electrolyte composed of 1-propyl-3-methylimidazolium iodide (PMII)/I_2 in BMII presented an initial PCE of 1.8 %, which one increased up to 3.0 % until the end of the experiment. This indicates that longer times of exposure are required to ensure the full infiltration of the more viscous ionic liquid electrolytes into the monolithic structure. In the same year, Gorlov *et al.* [50] produced M-DSSCs with I^-/IBr_2^- redox mediator. The highest PCE, 6.4 %, was achieved in M-DSSC using an electrolyte made of interhalogen ionic salts dissolved in γ-butyrolactone. The performance of the devices was evaluated for 1000 h under 350 $W \cdot m^2$ illumination provided by a sodium lamp and protected by an ultraviolet (UV)-filter under open-circuit conditions. M-DSSCs with an initial PCE of *ca*. 5 % showed a loss of performance of *ca*. 9-14 %.

The drawback of ionic liquids is their high viscosity, which causes mass transport limitations. This drawback was mitigated using a binary ionic liquid system, where the second ionic liquid should present a low viscosity [51]. Hinsch *et al.* (2008) [52] produced M-DSSC encapsulated using glass frit layers and employing volatile and non-volatile electrolytes. A PCE of 5.8 % was recorded using a volatile electrolyte [1-methyl-3-hexylimidazolium iodide (MHII)/I_2 in acetonitrile (ACN)], while a PCE of 2.7 % was achieved with a binary ionic liquid electrolyte [I_2 in ethylmethylimidazolium triflate (EMIOTf)/PMII]. The authors developed a model to analyze the charge transport in M-DSSCs. The results showed a concentration gradient of I^- into the graphite/carbon-black layer, which suggests that the counter-electrode operate as a reservoir for the electrolyte. Therefore, it is estimated that the diffusion-limited current in the M-DSSCs is enhanced by a factor of 2, in comparison with the conventional DSSCs. In 2010, Fredin *et al.* [53] evaluated the influence of binary ionic liquids electrolytes in M-DSSCs, employing 1-methyl-3-*n*-butylimidazolium cation (BMIm) but using

different anions (I^-, BF_4^-, SCN^-, CF_3COO^-, $CF_3SO_3^-$). The electron lifetime, the TiO_2 conduction band edge and the dye regeneration were affected by the chosen anion. The highest PCE was recorded using the SCN^- anion, the less viscous electrolyte, which delivered a PCE of 5.6 % under 250 $W \cdot m^{-2}$, and a PCE of 2.2 % under 1000 $W \cdot m^{-2}$. The efficiency decreased 10 % after 1000 h under 350 $W \cdot m^{-2}$ continuous illumination provided by a sodium lamp and under open-circuit conditions. PCEs of 7.0 % were reported for DSSCs employing binary ionic liquid electrolytes [54]; the decent PCEs and good stability reported in [50,53] shows that ionic liquids electrolytes are also suitable for M-DSSCs.

Co(III)/Co(II) [*ca.* 0.56 V *vs* normal hydrogen electrode (NHE)] [55] and Cu(II)/Cu(I) (*ca.* 0.94 V *vs* NHE) [55] redox complexes have emerged as the most promising electrolytes to replace the conventional I_3/I^- system (*ca.* 0.4 V *vs* NHE) [55]. Their higher redox potentials enhance the V_{OC} of the devices and decrease the driving force for dye regeneration. Besides, the limitations of iodide systems, such as volatility, corrosiveness and absorption of visible light, are not observed in these alternatives. Being a recent trend, there is only one report so far regarding M-DSSCs employing a Co(III)/(II)$(bpy)_3$ redox mediator [21]. 4-*tert*-butylpyridine (TBP) additive is often used in the cobalt electrolytes to suppress the back electron recombination by adsorption on the TiO_2 surface. However, when present in high concentration, could affect the diffusion of cobalt species and decrease the photocurrent [56]. The typical 0.6-0.8 M TBP used in conventional DSSCs [57] should not be extrapolated for M-DSSCs, since the spacer layer and the carbon counter-electrode could require a higher concentration of this additive. Both TiO_2 and carbon layers could adsorb TBP from the electrolyte, which decreases the amount of TBP available in the solution. This hypothesis was assessed by Santos *et al.* [21] using different concentrations of TBP (0.8-1.4 M) in the electrolyte composition. The highest performing M-DSSC used 1.2 M TBP, higher than the typical 0.8 M used in the conventional counterparts. These works, related with the effect of the electrolyte composition in M-DSSCs, are included in **Table 1.1**.

1.2.4 Conditions of sensitization

The sensitizer is a main component of a DSSC, since it is responsible for the light harvesting and the subsequent electron injection into the TiO_2 conduction band. The thermal and chemical stability of the ruthenium complexes, their ability to absorb a wide range of solar spectrum, and the position of HOMO/LUMO energy levels, turned them the most used sensitizers in iodide-mediated DSSCs [30]. Besides the sensitizer itself, it is also crucial to define the optimum sensitization time for each system. Insufficient dye adsorption limits the absorption of photons and, in consequence, hinders the photocurrent of the devices; on the other hand, excessive dye loading could cause agglomerates between

the dye molecules, blocking the pores of the photoanode and affecting the electron injection into the TiO_2 conduction band [40]. Sensitization times between 12-48 h were found to be optimum for conventional DSSCs sensitized with ruthenium dyes [58,59]. In M-DSSCs, the additional spacer layer and the thick carbon-based counter-electrode may require a different sensitization time. Surprisingly, this assumption was only considered in 2019 by Santos *et al.* [40]. These authors evaluated the performance of DSSCs and M-DSSCs, under dye loadings between 20 and 100 h in an ethanolic solution of N719, at room temperature. In the case of M-DSSCs, the best performance was reached only after *ca.* 60-70 h of sensitization time.

The biggest limitation of ruthenium dyes lies on their cost and on ruthenium scarcity. For that reason, metal-free organic dyes, such as Y123 and ADEKA-1, and Zn-porphyrin dyes, such as YD2 and SM315, have been extensively investigated [30,31]. Since their extinction coefficients are *ca.* 10 times higher than the ones for ruthenium dyes, very efficient DSSCs could be prepared using thinner mesoporous TiO_2 layers. The HOMO energy level of these dyes fits well with the redox potential of the cobalt and copper redox complexes, making them the preferred choice for these systems [60]. Cobalt-mediated M-DSSCs produced by Santos *et al.* [21] used a thinner mesoporous TiO_2 layer and a porphyrin dye, YD2-*o*-C8; the time needed for a complete sensitization was *ca.* 46±2 h. The works concerning the effect of sensitization conditions are included in **Table 1.1**.

1.3 Monolithic Dye-Sensitized Solar Cells Modules

The work published by Kay and Grätzel in 1996 [13] not only introduced the concept of M-DSSC, but also proved the straightforward upscale for M-DSSC modules. These authors prepared a small module made of 6 cells connected in series. As in small area devices, the photoanode was made of TiO_2-anatase, the spacer layer was made of TiO_2-rutile, and the counter-electrode was made of graphite and carbon-black nanoparticles. The layers were deposited using simple laboratory techniques, such as doctor-blading, screen-printing or spraying; the photoanode and the counter-electrode were electronically separated by a groove in the TCO-coated substrate. Unlike silicon modules, DSSCs modules are not so affected by small pin-holes due to the robustness and thickness of the counter-electrode. This small module, with a total active area of 21 cm^2, delivered a PCE of 5.3 %.

Onsetting on the year 2000, the research focused on the development of M-DSSCs modules for indoor applications. Burnside *et al.* (2000) [27] prepared M-DSSC modules made of three and five cells in series, with a total active area of 2.2 cm^2 and 8.3 cm^2, respectively. The triple-layer structure (TiO_2 photoanode, ZrO_2 spacer layer, and carbon counter-electrode) was prepared using laboratory-made

screen-printable pastes; the electrolyte solution was based on an ionic liquid composed of I_2 in MHII. The layers were characterized by scanning electron microscopy (SEM), nitrogen adsorption/desorption isotherms and X-ray diffraction (XRD); the rheology of the pastes was analysed. Under 50 and 250 lx indoor illumination, the performance of the M-DSSC modules was similar with the one recorded using a commercial amorphous silicon module, suggesting that M-DSSC could replace silicon solar cells for indoor applications.

A year later, Petterson *et al.* [28] developed monolithic modules composed of 5 cells in series, with a total TiO_2 active area of 9 cm^2. The cells were made of a TiO_2 photoanode, a ZrO_2 spacer layer and a graphite counter-electrode, all deposited by screen-printing. The sensitization was done by dipping using a ruthenium dye, while the electrolyte solution was based on an ionic liquid composed of I_2 in MHII. The encapsulation was done using a 40 μm flexible polyester film with a coating that absorbed UV-light. The performance of the M-DSSC modules was evaluated based on the maximum power output delivered by the devices. These authors found that the modules were affected by UV-light, and that an efficient sealing was crucial for stabilizing the devices. The quality of the sealing was evaluated using a humidity test: the modules were subjected to a relative humidity of 95 % and a temperature between 20 and 60 ºC for 10 days in a humidity chamber. Then, the modules were stored in dark for 10 days, before being illuminated at 5000 lx using a fluorescent lamp. After 200 days under continuous 5000 lx indoor illumination, the modules presented a minor decrease in the maximum power output, proving the good quality of the sealing process. The results showed that a UV-filter can minimize the degradation under UV-light, since the modules employing a UV-filter retained 94 % of the initial maximum power output after 200 days under continuous 5000 lx illumination.

In 2003, the same authors [29] subjected the devices under more stressful test conditions, focusing on the conjugated effect of illumination and humidity, as well the effect of temperature in the long-term performance of monolithic modules. After 90 days of continuous illumination at 1400 lx and 100 % relative humidity, only the modules with defects in the sealing suffered degradation. The modules exposed to a continuous illumination at 5000 lx for one year presented a decrease in the performance of 7 %. The influence of temperature was evaluated storing the modules in dark at temperatures between -20 ºC and 85 ºC for 70 days. Only the modules stored at temperature > 50 ºC showed loss of performance, mostly related to the decrease of V_{OC} due to faster recombination reactions. These works [27-29] illustrate the suitability of M-DSSC modules for indoor applications.

In 2007, Meyer *et al.* [61] prepared a 10×10 cm^2 module, made of 11 cells in series. These M-DSSC modules were composed of a TiO_2 mesoporous layer, a TiO_2-ZrO_2 spacer layer, and a double counter-electrode layer made of a thin platinum-carbon layer followed by a highly conductive carbon

layer. This M-DSSC module rendered a PCE of 5.8 % under 1-sun simulated solar light.

In 2009, Kato *et al.* [62] reported the longest stability test for DSSCs modules under outdoor conditions (2.5 years). These authors used a 11 × 10 cm^2 TCO-coated substrate, further divided into nine stripes. The M-DSSC cells were composed of a TiO_2-anatase mesoporous layer, a TiO_2-rutile spacer layer, and a carbon counter-electrode. The electrolyte was made of ionic liquid 1,2-dimethyl-3-propylimidazoliumiodide (DPII)/I_2 in γ-butyrolactone. Operating at the maximum power point, the modules – PCE of *ca.* 3 %, three cells in series – presented a deterioration factor of 1.7×10^{-4} /day. Since the modules did not present electrolyte leakage, the loss of performance was associated with the degradation of cell components. The J_{SC} did not show deterioration along 2.5 years of exposure, which could indicate the preservation of the properties of TiO_2, N719, and carbon counter-electrode; this assumption was proved using Raman's spectroscopy. V_{OC} and FF decreased along with the experiment, while the dark current and the resistance associated with the diffusion of I_3^- increased. The authors associated this deterioration with a change in the electrolyte composition derived from contamination with water or dust, and with a decrease in I_3^- concentration due to the sublimation of I^-. Comparing the performance of the outdoor M-DSSCs modules with the accelerated tests performed on small cells, it was possible to determine the acceleration factor of the light-soaking test, which is 11 times faster. These results show the importance of good encapsulation to preserve the long-term performance of DSSCs modules.

All works reported so far are on the development of M-DSSCs modules made of an opaque ZrO_2 or TiO_2-rutile spacer layer, and an opaque carbon-based counter-electrode. In 2009, Takeda *et al.* [15] demonstrated a 9.5 × 9.5 cm^2 semi-transparent module made of 12 cells connected in series. The M-DSSC modules were composed of a TiO_2 mesoporous layer made of *ca.* 20 nm TiO_2 nanoparticles, a SiO_2 spacer layer made of *ca.* 30 nm SiO_2 nanoparticles, and a Pt counter-electrode loaded with *ca.* 70 nm of indium tin oxide (ITO) nanoparticles. The performance of these devices was evaluated for 2000 h under 1-sun simulated solar light soaking at 60 ºC. The J_{SC}, FF, and PCE improved in the first 100 h, showing values close to the ones reported for M-DSSC modules employing opaque spacer layers and carbon-based counter-electrodes. The improvement in the FF was associated with the better electrical conductivity and catalytic activity properties of the Pt-loaded ITO counter-electrode. After the initial 100 h of light-soaking, the J_{SC} and FF present small fluctuations, while the V_{OC} slightly decreased along the experiment. Summarizing, after 2000 h of light-soaking, the M-DSSCs modules retained 85 % of the initial efficiency, *ca.* 3 %.

In 2010, Petterson *et al.* [16] designed four individual monolithic cells connected in parallel. These modules had a total active area of 13.5 cm^2, where each cell presented an active area of 3.38 cm^2.

The M-DSSCs modules were exposed to a continuous 1-sun simulated solar light at 50 ºC and open-circuit conditions. The PCE increased from 3.5 % to 5.0 % within first 100 h, and then kept stable for 2100 h; this aging experiment corresponds to *ca.* 3 years of outdoor exposure. The degradation factor determined for the PCE was 1.36×10^{-4} %/h. These authors point out the need for the developing standards for the accelerating tests. Despite experiments under 1000 h light soaking and 1000 h high temperature being very common nowadays, they were not the standard procedure at that time; later, NREL defined the conditions for several accelerated tests [63].

In 2012, Kato *et al.* [64] used a solvent-free ionic liquid (imidazolium salts) electrolyte, and reduced 1/6 the deterioration factor, from 7.8×10^{-5} /h to 1.3×10^{-5} /h. Using a Z907 dye, the devices retained *ca.* 80 % of their initial PCE after 15 000 h under 1-sun illumination at 60 ºC, which corresponds with 15 years of outdoor exposure. Unlike the previous work using γ-butyrolactone [62], the resistance associated with the diffusion of I_3^- did not increase, showing that the solvent-free ionic liquid electrolyte protects the device from changes in the electrolyte composition. Unfortunately, these authors do not indicate the PCE of these devices.

Up to now, the highest certified PCE for M-DSSC modules was achieved by Sharp Corporation [65], with a PCE of 10.7 % for a mini-module (< 200 cm^2 area) and a PCE of 8.8 % for a sub-module (200-800 cm^2 area) [66]. The works on M-DSSC modules are summarized in **Table 1.2**.

1.4 Solid-state DSSCs

Liquid-junction DSSCs present good PCEs but demonstrate also challenges, such as leakage of electrolyte solvent, degradation of the dye, and corrosion, compromising the long-term performance of these devices. The solvent leakage through the pre-drilled holes of liquid-junction DSSCs could be prevented by laser-assisted glass sealing these holes [67,68]. A different pathway for achiving stable DSSCs is the development of solid-state devices, by replacing the liquid redox mediator with a solid-state hole transporting material (HTM). The HTM should be photochemically stable, transparent, displaying a HOMO level slightly above of the HOMO level of the sensitizer (~200 mV), present high ionic conductivity and mobility, and should be amorphous since crystallization restricts the pore filling. The PCEs of solid-state DSSCs are lower than the ones reported for liquid-junction DSSCs. Their limitations include: the difficulty to fulfil the pores of the TiO_2 photoanode, resulting in incomplete dye regeneration; the low conductivity, causing high internal resistances; and the charge recombination at

Table 1.2

M-DSSCs modules employing different electrical spacer layers and counter-electrodes.

Year	Spacer layer	Counter-electrode	Sensitizer	Electrolyte	Active area	Nr. cells	PCE /%	ref
1996	TiO_2-rutile/ZrO_2 (9:1)	Graphite/carbon-black/TiO_2	N3	I_3^-/I^- a)	*ca.* 20 cm^2	6	5.3	[13]
2000	ZrO_2	Graphite/carbon-black	N719	I_2 in MHII	2.2 cm^2 8.3 cm^2	3 5	-	[27]
2001 2003	ZrO_2	Activated carbon	N3	I_2 in MHII	9 cm^2	5	-	[28] [29]
2007	TiO_2/ZrO_2	Platinized carbon layer + carbon layer	N719	I_3^-/I^- a)	60.7 cm^2	11	5.8	[61]
2009	TiO_2-rutile	Carbon	N719	DPII/I_2 a)	*ca.* 30 cm^2	3	*ca.* 3 b)	[62]
2009	SiO_2	Pt-loaded ITO	N719	DPII/I_2 a)	*ca.* 90 cm^2	12	*ca.* 3 b)	[15]
2010	ZrO_2	Activated carbon + platinized activated carbon	K77	BMII/I_2 a)	13.5 cm^2	4	5	[16]
2011					<200 cm^2 200-800 cm^2	7 26	10.7 (certified) 8.8 (certified)	[65] [66]
2012	SiO_2	Carbon	Z907	Solvent-free ionic liquid (imidazolium salts)	*ca.* 30 cm^2	3	-	[64]

a) dissolved in organic solvents; b) extracted from the *J-V* curve.

TiO_2/HTM interface, which decreases the V_{OC} [69,70], are other challenges of this technology.

Like M-DSSCs, the solid-state DSSCs typically uses only one TCO-coated substrate, with a groove separating the photoanode from the counter-electrode. A blocking-layer is deposited on the photoanode side to prevent the direct contact between the TCO layer and the HTM. The sensitization of the mesoporous TiO_2 layer is done prior to the HTM deposition. The back-contact, usually made of metal or carbon-based, is deposited by drop-casting or thermal evaporation on top of the HTM. The working principle of solid-state DSSCs is presented in **Fig. 1.11**. The main difference from liquid-junction DSSCs is the regeneration of the oxidized dye. This process is performed by a solid HTM, which is faster (ns) than the diffusion gradient characterized by the liquid redox mediator (μs). Therefore, the hole injection from HTM to the metal contact happens almost at the same time as the electron injection into the TiO_2 conduction band [69,70].

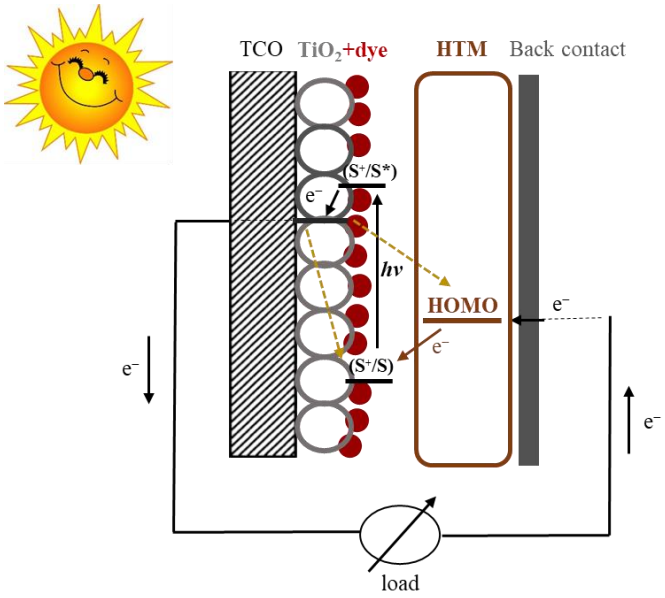

Fig. 1.11 – Schematic representation on the working principle of solid-state DSSCs.

The next subsection presents the most common HTM for solid-state DSSCs: organic and inorganic molecules, polymers, and coordination metal complexes [69,70].

1.4.1 Hole transport materials

Spiro-OMeTAD [2,2',7,7'-tetrakis(N,N'-di-p methoxyphenylamine)-9,9'-spirobifluorene] was for a long time the most used HTM in DSSCs and PSCs. This small size molecule has a glass-transition temperature (T_g) of 120 ºC, allowing a stable amorphous phase under ambient conditions. The main limitation of spiro-oMeTAD is the low charge carrier mobility, which limits the TiO_2 mesoporous layer thickness to 2 μm. Such a thin TiO_2 mesoporous layer compromises the light harvesting of the devices,

resulting in poor photocurrents [69,70]. This downside could be attenuated using a sensitizer with a wide extinction coefficient. Additives or p-dopants are often added into the spiro-oMeTAD solution to improve the performance of the solid-state DSSCs. The additives, such as Li salt and TBP, shift the TiO_2 conduction band and change the HTM morphology, allowing a better charge injection and preventing recombination at the TiO_2-HTM interface. The p-dopants partially oxidize the HTM, creating some vacancies and enhancing the hole mobility. PCEs higher than 7.0 % were achieved for solid-state DSSCs using spiro-oMeTAD HTM or derivatives of this molecule [71,72]. Burschka *et al.* (2011) [71] reported a solid-state DSSC with a spiro-oMeTAD HTM and a cobalt-based dopant, which one retained *ca.* 80 % of their initial efficiency after 40 days under 1000 $W \cdot m^{-2}$ illumination at 60 ºC.

Inorganic HTM for solid-state DSSCs includes CuI, CuBr, CuSCN, Cs_2SnI_6 and NiO. These compounds present good hole mobility. Their limitations include high series resistance (which compromises the photocurrent of the devices), the formation of crystals along the time (which promotes a worse connection with the sensitizer molecules), and the charge recombination at TiO_2/HTM interface. The size of the crystals can be decreased using an ionic liquid additive, while the electron recombination at TiO_2/HTM interface could be prevented by coating the TiO_2 molecules with insulating materials [69,70]. Up to now, PCEs of at least 8 % were reported for solid-state DSSCs using inorganic HTM [73,74].

Polymers, such as PEDOT and poly(3,4-ethylenedioxypyrrole) (PEDOP), are a suitable material for HTM in solid-state DSSCs. The monomers need to infiltrate into the TiO_2 mesoporous layer prior to the polymerization (*in situ* polymerization). The long and tangled chains of the polymers enable the charge transport, which promotes more points of contact between the molecules [69,70]. PCE of 7.1 % was reported for a solid-state DSSC with a PEDOT HTM [74], which is closer to the ones reported with spiro-OMeTAD or inorganic HTM.

The breakthrough in this field was made in 2015 by Freitag *et al.* [76] using coordination metal complexes as HTM for solid-state DSSCs. In these devices, the holes are kept open after the injection of the electrolyte, the solvent is slowly evaporated under ambient conditions, wetting and filling the TiO_2 mesoporous layer; for completely filling the device, the filling process has to be repeated one or two times. In the first experiment it was used a HTM of copper dimethyl phenanthroline $[Cu(dmp)_2]^{2+/1+}$ complexes. A solid-state DSSC with a PCE of 8.2 % was obtained, outperforming the liquid counterpart, with a PCE of 6.0 %; the main difference was on the J_{SC}. The copper-HTMs present advantages compared with the previously mentioned HTMs: solid-state DSSCs could be prepared without the cost associated with the high price of spiro-oMeTAD; thicker mesoporous TiO_2 could be used, which enhances the light harvesting of the devices; and higher V_{OC} could be achieved due to the more positive redox potential of the copper complexes. However, being this an innovative HTM, more

research is necessary to understand how the copper-HTMs are formed. Freitag *et al.* [76] suggested that the distorted tetragonal geometry of the copper complexes minimized the structural changes, and allowed a high electron transfer between Cu(I) and Cu(II). XRD showed that the copper-HTMs are partially crystallized, and photoinduced absorption spectroscopy (PIA) suggested a faster electron transport and a similar or higher electron lifetime compared with the liquid electrolyte, which resulted in higher charge collections. Up to now, the best performing solid-state DSSC was reported by Zhang *et al.* [77] in 2018. These solid-state DSSCs used a tetramethylbipyridyl $[Cu(tmby)]_2$ HTM, rendering a PCE of 11.7 % under 1-sun simulated solar light. Besides the good efficiency, these devices also presented decent stability. Cao *et al.* prepared DSSCs with $[Cu(tmby)]_2$ HTM and Y123 dye; these devices retained 85 % of their maximum power output after 200 hours under 500 $W \cdot m^{-2}$ illumination [78]. Copper-mediated liquid-junction DSSCs present PCE higher than 30 % under indoor illumination [7,26]. Therefore, these copper-HTM DSSCs are very promising for iPVs [3]. Cobalt polypyridine could also be suitable for solid-state DSSCs, despite the lower PCEs [79,80], which are associated with higher charge transport limitations [70].

The most efficient solid-state DSSCs with different HTM are summarised in **Table 1.3.**

Table 1.3

Solid-state DSSCs.

Year	Sensitizer	CE/Back-contact	HTM	Dopant HTM	Additives HTM	PCE /%	ref
2011	Y123	Silver	Spiro-OMeTAD	FK102	LiTFSI + TBP	7.2	[71]
2016	LEG4	Silver	X60*	-	LiTFSI + TBP	7.3	[72]
2012	N719	Pt	$CsSnI_{2.95}F_{0.05}$ + 5% SnF_2 + ZnO	-	-	10.2 (mask: 8.5)	[73]
2014	N719 + RLC5 + YD2-*o*-C8	Sputtered Pt or Au	Cs_2SnI_6	-	LiTFSI + TBP	7.8	[74]
2016	LEG4	Silver	PEDOT	-	LiTFSI + TBP	7.1	[75]
2016	Y123	Pt	$[Co(bpyPY4)](OTf)_{2.33}$	-	LiTFSI + TBP + TFMP	5.7	[79]
2018	WS-72 + CDA	PEDOT	$Cu(tmby)]_2$	-	LiTFSI + TBP	11.7	[77]

*molecule similar with spiro-OMeTAD

1.5 Scope of the thesis

DSSCs are an attractive PV technology to low-power indoor electronic devices. PCEs above 30 % were achieved in conventional laboratory-size DSSCs under 1000 lx artificial room light [7,26]. The monolithic configuration is straightforward for the fabrication of in-series modules, compatible with the roll-to-roll production [13,15-17], and offers *ca.* 20-30 % reduction of the device cost [14]. The number of works on M-DSSCs is smaller than the ones concerning the conventional counterparts, and typically reporting less efficient devices [23,24,40]; the lower PCE of M-DSSCs is associated with the inefficient light harvesting caused by poor reflectivity of the spacer layer, high charge transfer resistance at spacer layer/counter-electrode interface, high diffusion resistance of charge carriers in the electrolyte, high series resistance and low fill factor [22-25]. The work developed in this thesis overcomes these limitations by developing efficient, stable, and cost-effective M-DSSCs.

The thesis consists of 5 chapters. **Chapter 1** addresses iPVs, with emphasis on DSSCs. An overview of the working principle of DSSCs and the characterization techniques of solar cells are presented. State-of-the-art M-DSSCs are critically overviewed, discussing the role of the counter-electrode, the spacer layer, the electrolyte composition, and the sensitization conditions on the overall photovoltaic performance of the laboratory-size devices; a review of M-DSSCs modules and solid-state DSSCs is presented.

Chapter 2 presents the development of new eco-friendly and cost effective SiO_2-TiO_2 spacer layers derived entirely from water-based formulations. The reflectance of these spacers is improved by adding 30 wt.% of TiO_2-anatase nanoparticles, but without compromising the percolation of electrons. The sensitization time for iodide-mediated M-DSSCs with a Pt metal counter-electrode is addressed here for the first time; the performance of these monolithic assembled devices is evaluated along 1000 h under natural aging. This work allowed to produce a highly reflective eco-friendly and cost effective spacer layer for M-DSSCs, rendering a stable device with 1-sun PCE of 8.3 %, the highest reported PCE for iodide-mediated M-DSSCs.

Chapter 3 presents cobalt-mediated M-DSSCs, that have never been considered before. The exchange current density on FTO − Pt nanoparticles, Pt metal, graphite/carbon-black, and PEDOT:PSS, the electron charge transfer resistance at the counter-electrode/electrolyte interface, and the apparent activation energy for electron transfer in cobalt electrolyte are determined to select the favourable counter-electrode. The sensitization time for cobalt-mediated M-DSSCs and the concentration of TBP in the electrolyte solution are addressed; the photovoltaic performance of these devices is followed along 1000 h under natural aging. In the counter electrode, Pt was replaced with a graphite/carbon-black, rendering a stable device with the highest PCE ever reported for liquid-junction M-DSSCs under 1-sun simulated solar light, 9.5 %, and a decent PCE under 1000 lx

indoor light, 22.0 %. These results show that the developed M-DSSCs are very attractive for indoor use.

Chapter 4 aims to evaluate the long-term performance of cobalt-mediated M-DSSCs in fully hermetic seal. The device edge and the electrolyte injection holes are glass-sealed using a laser-assisted process with glass-frit. The hermicity and robustness of the device encapsulation comply with the standard helium gas leak test MIL-STD-883, method 1014.10, performed before and after humidity-freeze cycles following IEC 61646 standard. The effect of the standard ISOS test conditions on the interfacial charge transfer of M-DSSCs, the dye desorption, and the redistribution of cobalt ions in the working device are considered, and their impact on the PCE and the stability of the devices. Glass-encapsulated M-DSSCs with ACN-based cobalt electrolyte show the most steady history of photovoltaic metrics, passing successfully for the first time several ISOS tests, including thermal cycle up to 85 ^{o}C, 1000 h of shelf-aging, and 1000 h of solar and artificial light soaking with a passive load.

Finally, **Chapter 5** presents the main conclusions of this thesis, along with suggestions for future work.

Acknowledgments

F. Santos acknowledges the FCT for her PhD grant reference SFRH/BD/132388/2017. The research leading to these results also received funding from: i) project 2SMART - engineered Smart materials for Smart citizens, with reference NORTE-01-0145-FEDER-000054, supported by Norte Portugal Regional Operational Programme (NORTE 2020), under the PORTUGAL 2020 Partnership Agreement, through the European Regional Development Fund (ERDF); and ii) Base - UIDB/00511/2020 and Programmatic - UIDP/00511/2020 Funding of the Laboratory for Process Engineering, Environment, Biotechnology and Energy – LEPABE - funded by national funds through the FCT/MCTES (PIDDAC).

References

[1] International Energy Outlook 2021, U.S. Energy Administration, 2021.

[2] M.A. Green, E.D. Dunlop, J. Hohl-Ebinger, M. Yoshita, N. Kopidakis, X. Hao, Solar cell efficiency tables (Version 58), *Prog. in Photovolt.: Res. Appl.,* 2021, 29, 657-667. DOI: 10.1002/pip.3444.

[3] I. Mathews, S.N. Kantareddy, T. Buonassisi, I.M. Peters, Technology and Market Perspective for

Indoor Photovoltaic Cells, *Joule*, 2019, 3(6), 1415-1426. DOI: 10.1016/j.joule.2019.03.026.

[4] E. Mirabi, F.A. Abarghuie, R. Arazi, Integration of buildings with third-generation photovoltaic solar cells: a review, *Clean Energy*, 2021, 5, 3, 505–526. DOI: 10.1093/ce/zkab031.

[5] NREL – Best Research Cell Efficiencies. Available on: https://www.nrel.gov/pv/cell-efficiency.html

[6] B. Ehrler, E. Alarcón-Lladó, S.W. Tabernig, T. Veeken, E.C. Garnett, A. Polman, Photovoltaics Reaching for the Shockley-Queisser Limit, *ACS Energy Lett.*, 2020, 5, 9, 3029–3033. DOI: 10.1021/acsenergylett.0c01790.

[7] D. Zhang, M. Stojanovic, Y. Ren, Y. Cao, F.T. Eickemeyer, E. Socie, N. Vlachopoulos, J.-E. Moser, S.M. Zakeeruddin, A. Hagfeldt, M. Grätzel, A molecular photosensitizer achieves a V_{oc} of 1.24 V enabling highly efficient and stable dye-sensitized solar cells with copper(II/I)-based electrolyte, *Nat. Commun.*, 2021, 12, 1777. DOI: 10.1038/s41467-021-21945-3.

[8] H.K.H. Lee, J. Wu, J. Barbé, S.M. Jain, S. Wood, E.M. Speller, Z. Li, F.A. Castro, J.R. Durrant, W.C. Tsoi, Organic photovoltaic cells – promising indoor light harvesters for self-sustainable electronics, *J. Mater. Chem. A*, 2018, 6(14), 5618–5626. DOI:10.1039/c7ta10875c.

[9] C. Dong, X.-M. Li, C. Ma, W.-F. Yang, J.-J. Cao, Fe. Igbari, Z.-K. Wang, L.-S. Liao, Lycopene-Based Bionic Membrane for Stable Perovskite Photovoltaics, *Adv. Funct. Mater.*, 2021, 31, 2011242. DOI:10.1002/adfm.202011242.

[10] A. Muñoz-García, I. Benesperi, G. Boschloo, J. Concepcion, J. Delcamp, E. Gibson, G. Meyer, M. Pavone, H. Pettersson, A. Hagfeldt, M. Freitag, Dye-sensitized solar cells strike back, *Chem. Soc. Rev.*, 2021. DOI: 10.1039/D0CS01336F.

[11] B. Li, B. Hou, G.A.J. Amaratunga, Indoor photovoltaics, *The Next Big Trend* in solution-processed solar cells, *InfoMat.*, 2021; 3: 445– 459. DOI: 10.1002/inf2.12180.

[12] B. O'Regan, M. Grätzel, A low-cost, high-efficiency solar cell based on dye-sensitized colloidal TiO_2 films, *Nature*, 1991, 353, 737-740. DOI: 10.1038/353737a0.

[13] A. Kay, M. Grätzel, Low-cost photovoltaic modules based on dye sensitized nanocrystalline titanium dioxide and carbon powder, *Sol. Energy Mater. Sol. Cells*, 1996, 44, 99-117. DOI: 10.1016/0927-0248(96)00063-3.

[14] J.M. Kroon, Energy Research Center report, 2005, ECN-C-05-078, 1-41.

[15] Y. Takeda, N. Kato, K. Higuchi, A. Takeichi, T. Motohiro, S. Fukumoto, T. Sano, T. Toyoda, Monolithically series-interconnected transparent modules of dye-sensitized solar cells, *Sol. Energy Mater. Sol. Cells,* 2009, 93, 808–811. DOI:10.1016/j.solmat.2008.09.054.

[16] H. Pettersson, T. Gruszecki, C. Schnetz, M. Streit, Y. Xu, L. Sun, M. Gorlov, L. Kloo, G.

Boschloo, L. Häggman, A. Hagfeldt, Parallel-connected monolithic dye-sensitised solar modules, *Prog. Photovolt: Res. Appl.,* 2010, 18, 340-345. DOI:10.1002/pip.971.

[17] A. Fakharuddin, R. Jose, T.M. Brown, F. Fabregat-Santiago, J. Bisquert, A Perspective on the Production of Dye-Sensitized Solar Modules, *Energy Environ. Sci.*, 2014, 7(12), 3952–3981. DOI:10.1039/c4ee01724b.

[18] D. Fu, P. Lay, U. Bach, TCO-free flexible monolithic back-contact dye-sensitized solar cells, *Energy Environ. Sci.*, 2013, 6(3), 824-829. DOI: 10.1039/C3EE24338A.

[19] J. He, K. Wang, F. Huang, Y. Peng, C. Bing, Fabrication and Performances of Flexible Monolithic Dye-sensitized Solar Cell Using Metal Reinforced Porous Counter Electrodes, *Curr. Nanosci.,* 2015, 11(4), 488-493. DOI: 10.2174/1573413711666150202232622.

[20] K. Kakiage, Y. Aoyama, T. Yano, K. Oya, J.-ichi Fujisawa,' M. Hanaya, Highly-efficient dye-sensitized solar cells with collaborative sensitization by silyl-anchor and carboxy-anchor dyes, *Chem. Commun.*, 2015, 51(88), 15894-15897. DOI: 10.1039/C5CC06759F.

[21] F. Santos, C. Hora, D. Ivanou, A. Mendes, Efficient Liquid-Junction Monolithic Cobalt-Mediated Dye-Sensitized Solar Cells for Solar and Artificial Light Conversion. *ACS Appl. Energy Mater.,* 2021, 4, 5, 5050–5058. DOI: 10.1021/acsaem.1c00616.

[22] G. Liu, H. Wang, X. Li, Y. Rong, Z. Ku, M. Xu, L. Liu, M. Hu, Y. Yang, P. Xiang, T. Shu, H. Han, A mesoscopic platinized graphite/carbon black counter electrode for a highly efficient monolithic dye-sensitized solar cell, *Electrochim. Acta*, 2012, 69, 334-339. DOI: 10.1016/j.electacta.2012.03.012.

[23] J. Kwon, N.-G. Park, J.Y. Lee, M.J. Ko, J.H. Park, Highly Efficient Monolithic Dye-Sensitized Solar Cells, *ACS Appl. Mater. Interfaces*, 2013, 5(6), 2070-2074. DOI: 10.1021/am302974z.

[24] F. Behrouznejad, N. Taghavinia, N. Ghazyani, Monolithic dye sensitized solar cell with metal foil counter electrode, *Org. Electron.*, 2018**,** 57, 194-200. DOI: 10.1016/j.orgel.2018.03.009.

[25] S.J. Thompson, J.M. Pringle, X.L. Zhang, Y.-B. Cheng, A novel carbon–PEDOT composite counter electrode for monolithic dye-sensitized solar cells, *J. Phys. D Appl. Phys.*, 2012, 46, 024007. DOI: 10.1088/0022-3727/46/2/024007.

[26] H. Michaels, M. Rinderle, R. Freitag, I. Benesperi, T. Edvinsson, R. Socher, A. Gagliardi, M. Freitag, Dye-sensitized solar cells under ambient light powering machine learning: towards autonomous smart sensors for the internet of things, ***Chem. Sci.***, 2020, **11**, 2895-2906. DOI: 10.1039/C9SC06145B.

[27] S. Burnside, S. Winkel, K. Brooks, V. Shklover, M. Grätzel, A. Hinsch, R. Kinderman, C. Bradbury, A. Hagfeldt, H. Pettersson, Deposition and characterization of screen-printed porous multi-

layer thick film structures from semiconducting nanomaterials for use in photovoltaic devices, *J. Mater. Sci.: Mater. Electron.*, 2000, 11, 355-362. DOI: 10.1023/A:1008989601919.

[28] H. Pettersson, T. Gruszecki, Long-term stability of low-power dye-sensitized solar cells prepared by industrial methods, *Sol. Energy Mater. Sol. Cells*, 2001, 70, 203-212. DOI: 10.1016/S0927-0248(01)00025-3.

[29] H. Pettersson, T. Gruszecki, L.-H. Johansson, P. Johander, Manufacturing Method for Monolithic Dye-Sensitized Solar Cells Permitting Long-Term Stable Low-Power Modules, *Sol. Energy Mater. Sol. Cells*, 2003, 77, 405-413. DOI: 10.1016/S0927-0248(02)00368-9.

[30] K. Sharma, V. Sharma, S.S Sharma, Dye-Sensitized Solar Cells: Fundamentals and Current Status, *Nanoscale Res. Lett.*, 2018, 13, 381. DOI: 10.1186/s11671-018-2760-6.

[31] N. Mariotti, M. Bonomo, L. Fagiolari, N. Barbero, C. Gerbaldi, F. Bella, C. Barolo, Recent Advances in Eco-Friendly and Cost-Effective Materials towards Sustainable Dye-Sensitized Solar Cells, *Green Chem,*. 2020, 22, 7168-7218. DOI: 10.1039/D0GC01148G.

[32] M. Kokkonen, P. Talebi, J. Zhou, S. Asgari, S.A. Soomro, F. Elsehrawy, J. Halme, S. Ahmad, A. Hagfeldt, S.G. Hashmi, Advanced research trends in dye-sensitized solar cells, *J. Mater. Chem. A*, 2021, 9, 10527-10545. DOI: 10.1039/D1TA00690H.

[33] O.S. Al-Qurashi, N. Wazzan, Prediction of Power Conversion Efficiencies of Diphenylthienylamine-Based Dyes Adsorbed on the Titanium Dioxide Nanotube, *ACS Omega*, 2021, 6(13), 8967-8975. DOI:10.1021/acsomega.0c06340.

[34] A. Sacco, Electrochemical Impedance Spectroscopy: Fundamentals And Application In Dye-Sensitized Solar Cells, *Renew. Sust. Energ. Rev.*, 2017, 79, 814-829. DOI: 10.1016/j.rser.2017.05.159.

[35] S. Sarker, A.J.S. Ahammad, H. Seo, D.M. Kim, Electrochemical Impedance Spectra Of Dye-Sensitized Solar Cells: Fundamentals And Spreadsheet Calculation, *Int. J. Photoenergy*, 2014. DOI: 10.1155/2014/851705.

[36] F. Fabregat-Santiago, Bisquert, G. Garcia-Belmonte, G. Boschloo, A. Hagfeldt, Influence Of Electrolyte In Transport And Recombination In Dye-Sensitized Solar Cells Studied By Impedance Spectroscopy, *Sol. Energy Mater. Sol. Cells*, 2005, 87(1-4), 117–131. DOI: 10.1016/j.solmat.2004.07.017.

[37] Q. Wang, J.-E. Moser, M. Grätzel, Electrochemical Impedance Spectroscopic Analysis of Dye-Sensitized Solar Cells, *J. Phys. Chem. B*, 2005, 109(31), 14945–14953. DOI:10.1021/jp052768h.

[38] F. Fabregat-Santiago, J. Bisquert, E. Palomares,L. Otero, D.-B. Kuang, S. Zakeeruddin, M. Grätzel, Correlation between Photovoltaic Performance and Impedance Spectroscopy of Dye-

Sensitized Solar Cells Based on Ionic Liquids, *J. Phys. Chem. C*, 2007, 111. DOI: 10.1021/jp066178a.

[39] S. Ito, K. Takahashi, Fabrication of Monolithic Dye-Sensitized Solar Cell Using Ionic Liquid Electrolyte, *Int. J. Photoenergy*, 2012. DOI: 10.1155/2012/915352.

[40] F. Santos, C. Hora, G. Bernardo, D. Ivanou, A. Mendes, Efficient Monolithic Dye Sensitized Solar Cells with Eco-Friendly Silica-Titania Spacer Layers, *Sol. Energy*, 2019, 183, 419–424. DOI: 10.1016/j.solener.2019.03.056.

[41] M.A.M. Al-Alwani, A.B. Mohamad, N.A. Ludin, A.A.H. Kadhum, K. Sopian, Dye-Sensitised Solar Cells: Development, Structure, Operation Principles, Electron Kinetics, Characterisation, Synthesis Materials And Natural Photosensitisers, *Renew. Sust. Energ. Rev.*, 2016, 65, 183-213. DOI: 10.1016/j.rser.2016.06.045.

[42] M.-E. Yeoh, K.-Y. Chan, Recent Advances In Photo-Anode For Dye-Sensitized Solar Cells: A Review, *Int. J. Energy Res.*, 2017, 41: 2446– 2467. DOI: 10.1002/er.3764.

[43] J. Wu, Z. Lan, J. Lin, M. Huang, Y. Huang, L. Fan, G. Luo, Y. Lin, Y. Xie, Y. Wei, Counter electrodes in dye-sensitized solar cells, *Chem. Soc. Rev.*, 2017, 46(19), 5975–6023. DOI:10.1039/c6cs00752j.

[44] U. Ahmed, M. Alizadeh, N.A. Rahim, S. Shahabuddin, M.S. Ahmed, A.K. Pandey, A comprehensive review on counter electrodes for dye sensitized solar cells: A special focus on Pt-TCO free counter electrodes, *Sol. Energy*, 2018, 174, 1097–1125. DOI:10.1016/j.solener.2018.10.010.

[45] L. Vesce, R. Riccitelli, G. Mincuzzi, A. Orabona, G. Soscia, T. Brown, A. Di Carlo, A. Reale, Fabrication of Spacer and Catalytic Layers in Monolithic Dye-Sensitized Solar Cells, *IEEE J. Photovolt.*, 2013, 3(3), 1004-1011. DOI: 10.1109/JPHOTOV.2013.2262374.

[46] S. Thompson, N. Duffy, U. Bach, C. Bing, On the Role of the Spacer Layer in Monolithic Dye-Sensitized Solar Cells, *J. Phys. Chem. C*, 2010, 114, 2365-2369. DOI: 10.1021/jp907967h.

[47] A. Hinsch, R. Kinderman, M. Späth, E. Rijnberg, J. Roosmalen, The performance of dye-sensitised solar cells with a one-facial, monolithic layer built-up prepared by screen printing, 2nd World Conference and Exhibition on Photovoltaic Solar Energy Conversion, Vienna, 1998.

[48] R.A.A. Talip, W.Z.N. Yahya, M.A. Bustam, Ionic Liquids Roles and Perspectives in Electrolyte for Dye-Sensitized Solar Cells, *Sustainability, 2020,* 12, 7598. DOI: 10.3390/su12187598.

[49] H. Pettersson, T Gruszecki, R. Bernhard, L. Häggman, M. Gorlov, G. Boschloo, T. Edvinsson, L. Kloo, A. Hagfeldt, The monolithic multicell: a tool for testing material components in dye-sensitized solar cells. *Prog. Photovolt: Res. Appl.*, 2007, 15: 113-121. DOI: 10.1002/pip.713.

[50] M. Gorlov, H. Pettersson, A. Hagfeldt, L. Kloo, Electrolytes for Dye-Sensitized Solar Cells Based on Interhalogen Ionic Salts and Liquids, *Inorg. Chem.*, 2007, 46 (9), 3566-3575. DOI: 10.1021/ic062244b.

[51] S.M.M. Yusof, W.Z.N. Yahya, Binary Ionic Liquid Electrolyte for Dye-Sensitized Solar Cells, *Procedia Eng*., 2016, 148, 100-105. DOI: 10.1016/j.proeng.2016.06.453.

[52] A. Hinsch, S. Behrens, M. Berginc, H. Bönnemann, H. Brandt, A. Drewitz, F. Einsele, D. Faßler, D. Gerhard, H. Gores, R. Haag, T. Herzig, S. Himmler, G. Khelashvili, D. Koch, G. Nazmutdinova, U. Opara Krašovec, P. Putyra, U. Rau, M. Zistler, Material development for dye solar modules: Results from an integrated approach, *Prog. Photovolt.: Res. Appl.*, 2008, 16, 489 - 501. DOI: 10.1002/pip.832.

[53] K. Fredin, M. Gorlov, H. Pettersson, A. Hagfeldt, L. Kloo, G. Boschloo On the Influence of Anions in Binary Ionic Liquid Electrolytes for Monolithic Dye-Sensitized Solar Cells, *J. Phys. Chem. C*, 2007, 111. DOI: 10.1021/jp072514r.

[54] Z. Wang, B. Wenger, R. Humphry-Baker, J.-E. Moser, J. Teuscher, W. Kantlehner, J. Mezger, E. Stoyanov, S. Zakeeruddin, M. Grätzel, Charge separation and efficient light energy conversion in sensitized mesoscopic photoelectrochemical cells based on binary ionic liquids, *J. Am. Chem. Soc.*, 2005, 127, 6850-6856. DOI: 10.1021/ja042232u.

[55] H. Iftikhar, G.G. Sonai, S.G. Hashmi, A.F. Nogueira, P.D. Lund, Progress on Electrolytes Development in Dye-Sensitized Solar Cells, *Mater.*, 2019, 12, 1998. DOI:10.3390/ma12121998.

[56] T.M. Koh, K. Nonomura, N. Mathews, A. Hagfeldt, M. Grätzel, S.G. Mhaisalkar, A.C. Grimsdale, Influence of 4-tert-Butylpyridine in DSCs with CoII/III Redox Mediator, *J. Phys. Chem. C*, 2013, 117(30), 15515–15522. DOI:10.1021/jp403918q.

[57] A. Yella, H.-W. Lee, H.N. Tsao, C. Yi, A.K. Chandiran, M.K. Nazeeruddin, E.W.-G. Diau, C.-Y. Yeh, S.M. Zakeeruddin, M. Grätzel, Porphyrin-Sensitized Solar Cells with Cobalt (II/III)−Based Redox Electrolyte Exceed 12 Percent Efficiency, *Science*, 2011, 334, 629−634. DOI: doi:10.1126/science.1209688.

[58] J.K. Kim, H. Seo, M.K. Son, I. Shin, J. Hong, H.J. Kim, The analysis of the change in the performance and impedance of dye-sensitized solar cell according to the dye-adsorption time, *Curr. Appl. Phys*., 2010, 10, S418–S421. DOI: 10.1016/j.cap.2010.02.024.

[59] E. Dell'Orto, L. Raimondo, A. Sassella, A. Abbotto, Dye-sensitized solar cells: Spectroscopic evaluation of dye loading on TiO_2, *J. Mater. Chem*., 2012, 22, 11364–11369. DOI: 10.1039/c2jm30481c.

[60] F. Bella, S. Galliano, C. Gerbaldi, G. Viscardi, Cobalt-Based Electrolytes for Dye-Sensitized

Solar Cells: Recent Advances towards Stable Devices, *Energies*, 2016, 9, 384. DOI:10.3390/en9050384.

[61] T. Meyer, D. Martineau, A. Azam, A. Meyer, All screen printed dye solar cell. *Proc. SPIE*, 2007, 6656. DOI: 10.1117/12.734545.

[62] N. Kato, Y. Takeda, K. Higuchi, A. Takeichi, E. Sudo, H. Tanaka, T. Motohiro, T. Sano, T. Toyoda, Degradation analysis of dye-sensitized solar cell module after long-term stability test under outdoor working condition, *Sol. Energy Mater. Sol. Cells*, 2009, 93, 893-897. DOI: 10.1016/j.solmat.2008.10.022

[63] C.R. Osterwald, Terrestrial Photovoltaic Module Accelerated Test-To-Failure Protocol, Technical Report NREL/TP-520-42893, 2008.

[64] N. Kato, K.Higuchi, H. Tanaka, J. Nakajima, T. Sano, T. Toyoda, Improvement in long-term stability of dye-sensitized solar cell for outdoor use, *Sol. Energy Mater. Sol. Cells,* 2011, 95, 301-305. DOI: 10.1016/j.solmat.2010.04.019.

[65] R. Komiya, A. Fukui, N. Murofushi, N. Koide, R. Yamanaka, H. Katayama, Improvement of the conversion efficiency of a monolithic type dyesensitized solar cell module, *Technical Digest, 21st International Photovoltaic Science and Engineering Conference*, Fukuoka, November 2011, 2C-5O-08.

[66] M. Kawai, High-durability dye improves efficiency of dye-sensitized solar cells, *Nikkei Electronics*, 2013.

[67] D.K. Ivanou, R. Santos, J. Maçaira, L. Andrade, A. Mendes, Laser assisted glass frit sealing for production large area DSCs panels, *Sol. Energy*, 2016, **135**, 674–681. DOI: 10.1016/j.solener.2016.06.043.

[68] S. Emami, J. Martins, D. Ivanou, A. Mendes, Advanced Hermetic Encapsulation of Perovskite Solar Cells: The Route to Commercialization, *J. Mater. Chem. A*, 2020, **8**, 2654-2662. DOI: 10.1039/C9TA11907H.

[69] J. Zhang, M. Freitag, A. Hagfeldt, G. Boschloo, Solid-State Dye-Sensitized Solar Cells. *Molecular Devices for Solar Energy Conversion and Storage,* 2017, 151–185. DOI:10.1007/978-981-10-5924-7_4.

[70] I. Benesperi, H. Michaels, M. Freitag, The Researcher's Guide to Solid-state Dye-sensitized Solar Cells, *J. Mater. Chem. C*, 2018, **6**, 11903-11942. DOI :10.1039/c8tc03542c.

[71] J. Burschka, A. Dualeh, F. Kessler, E. Baranoff, N.-L. Cevey-Ha, C. Yi, M.K. Nazeeruddin, M. Grätzel, Tris(2-(1H-pyrazol-1-yl)pyridine)cobalt(III) as p-Type Dopant for Organic Semiconductors and Its Application in Highly Efficient Solid-State Dye-Sensitized Solar Cells, *J. Am. Chem. Soc.*,

2011, 133, 18042–18045. DOI: 10.1021/ja207367t.

[72] B. Xu, D. Bi, Y. Hua, P. Liu, M. Cheng, M. Grätzel, L. Kloo, A. Hagfeldt, L. Sun, (2016). A low-cost spiro[fluorene-9,9′-xanthene]-based hole transport material for highly efficient solid-state dye-sensitized solar cells and perovskite solar cells, *Energy Environ. Sci.*, 2016, 9(3), 873–877. DOI: 10.1039/c6ee00056h.

[73] I. Chung, B. Lee, J. He, R.P.H. Chang, M.G. Kanatzidis, All-solid-state dye-sensitized solar cells with high efficiency, *Nature*, 2012, 485(7399), 486–489. DOI:10.1038/nature11067.

[74] B. Lee, C.C. Stoumpos, N. Zhou, F. Hao, C. Malliakas, C.-Y. Yeh, T.J Marks, M.G. Kanatzidis, R.P.H. Chang, Air-Stable Molecular Semiconducting Iodosalts for Solar Cell Applications: Cs2SnI6 as a Hole Conductor, *J. Am. Chem. Soc.*, 2014, 136(43), 15379–15385. DOI:10.1021/ja508464w.

[75] J. Zhang, N. Vlachopoulos, M. Jouini, M.B. Johansson, X. Zhang, M.K. Nazeeruddin, G. Boschloo, E.M.J. Johansson, A. Hagfeldt, Efficient solid-state dye sensitized solar cells: The influence of dye molecular structures for the in-situ photoelectrochemically polymerized PEDOT as hole transporting material, *Nano Energy*, 2016, 19, 455-470. DOI: 10.1016/j.nanoen.2015.09.010.

[76] M. Freitag, Q. Daniel, M. Pazoki, K. Sveinbjornsson, J. Zhang, L. Sun, A. Hagfeldt, G.Boschloo, High-efficiency dye-sensitized solar cells with molecular copper phenanthroline as solid hole conductor, *Energy Environ. Sci.*, 2015, 8(9):2634–2637. DOI:10.1039/c5ee01204j.

[77] W. Zhang, Y. Wu, H. Bahng, Y. Cao, C. Yi, Y. Saygılı, J. Luo, L. Kavan, J.-E. Moser, A. Hagfeldt, H. Tian, S. Zakeeruddin, W. Zhu, M. Grätzel, Comprehensive control of voltage loss enables 11.7% efficient solid-state dye-sensitized solar cells, *Energy Environ. Sci.*, 2018, 11. DOI: 10.1039/C8EE00661J.

[78] Y.S. Cao, A. Ummadisingu, J. Teuscher, J. Luo, N. Pellet, F. Giordano, S.M. Zakeeruddin, J.-E. Moser, M. Freitag, A. Hagfeldt, M. Grätzel, 11% efficiency solid-state dye-sensitized solar cells with copper(ii/i) hole transport materials, *Nat. Commun.*, 2017, 8:15390. DOI:10.1038/ncomms15390.

[79] M.K. Kashif, R.A. Milhuisen, M. Nippe, J. Hellerstedt, D.Z. Zee, N.W. Duffy, B. Halstead, F. De Angelis, S. Fantacci, M.S. Fuhrer, C.J. Chang, Y.-B. Cheng, J.R. Long, L. Spiccia, U. Bach, Cobalt Polypyridyl Complexes as Transparent Solution-Processable Solid-State Charge Transport Materials, *Adv. Energy Mater.*, 2016, 6(24), 1600874. DOI:10.1002/aenm.201600874.

[80] X.L. Zhang, W. Huang, A. Gu, W. Xiang, F. Huang, Z.X. Guo, Y.-B. Cheng, L. Spiccia, High efficiency solid-state dye-sensitized solar cells using a cobalt(ii/iii) redox mediator, *J. Mater. Chem. C*, 2017, 5(20), 4875–4883. DOI:10.1039/c7tc0099.

CHAPTER 2

EFFICIENT MONOLITHIC DYE-SENSITIZED SOLAR CELLS WITH ECO-FRIENDLY SILICA-TITANIA SPACER LAYERS

Adapted from the peer-reviewed article

F. Santos, C. Hora, G. Bernardo, D. Ivanou, A. Mendes, Efficient Monolithic Dye Sensitized Solar Cells with Eco-Friendly Silica-Titania Spacer Layers, *Sol. Energy*, 2019, 183, 419–424. DOI: 10.1016/j.solener.2019.03.056

2

Efficient monolithic dye-sensitized solar cells with eco-friendly silica-titania spacer layers

2.1 Introduction

Merging low manufacturing cost with good power conversion efficiency (PCE), dye-sensitized solar cells (DSSCs) are the object of intensive scientific research [1-3], which resulted already in full commercial products [2-4].

The highest confirmed PCE of DSSCs with Ru-sensitizer and I_3^-/I^- redox mediator is 11.9 % [5]; recently, certified PCE of 13.0 % was achieved using the emergent redox couples [6]. Besides, efficiency of 14.3 % was already reported in DSSCs employing porphyrin dyes and cobalt redox shuttle [7]. These efficiency values were obtained using liquid junction cells in which a photoanode and a counter-electrode are assembled on separated conducting glasses and placed opposite each other, with the microgap between the electrodes filled with the electrolyte – so-called "conventional" architecture [3]. In an alternative architecture, so-called "monolithic" DSSCs (M-DSSC) [3,8], both electrodes are configured on a single conducting glass: photoanode, electrical spacer layer, and counter-electrode. This arrangement is encapsulated using a non-conductive material; the cell is then filled with electrolyte and sealed. Monolithic design is quite straightforward for production of in series modules [3,8,9] compatible with roll-to-roll processing and offers 20–30 % of material cost reduction [10]. The challenging objective is, however, to improve the PCEs of M-DSSCs as they are less efficient than conventional analogs. In M-DSSCs the photoanode is the same as in a "conventional" cell, and their lower PCE is usually associated with an increased charge-transfer resistance in the spacer layer/counter-electrode interface, namely because of inefficient reduction of triiodide(iodine), and high series resistance observed when carbon-based counter-electrodes are used; higher mass transport/electrical resistance of the electrolyte through the spacer layer; inefficient light harvesting caused by poor reflectivity of the spacer layer [11-14].

The works on liquid junction M-DSSCs advancements are not numerous [8,9,11-16] mainly aiming at developing cost-effective and energy-efficient counter-electrodes. Liu *et al*. (2012) [11] reported 7.61 % of PCE in M-DSSCs when platinized graphite/carbon-black counter-electrode was

used. Kwon *et al.* (2013) [12] improved the efficiency of M-DSSCs up to 7.73 % using PEDOT as a counter-electrode and a macroporous polyethylene membrane as an electrical spacer. Behrouznejad *et al.* (2018) [13] suggested replacing the carbon counter-electrode with a platinized Ni/Cr foil, physically attached to the spacer layer, achieving a PCE of 8.0 %. Surprisingly, little attention is paid to tuning the spacer layer, known to display a high impact on the efficiency of DSSCs [14,16].

As electrical spacer layers, porous films of ZrO_2 are commonly used. The spacer layer is applied by spreading the paste on top of the photoanode followed by sintering. Commercial pastes are heavily loaded with volatile organics (~ 60-70 wt.%): α-terpineol, acetic acid, and ethanol. In addition to the higher cost of ZrO_2 itself, the need for capturing the volatiles in large-scale industrial production leads to the increase of the process cost.

In this report, a silica-based electrical spacer layer for M-DSSCs derived from entirely aqueous formulations is described. Silicon dioxide is an abundant and cheap material with high dielectric properties and stability. However, silica is very transparent. To tune the reflectivity of the spacer layers, anatase nanoparticles were added to the formulations. Application of the developed spacers in M-DSSCs rendered a device with the highest to date power conversion efficiency in monolithic cells, 8.3 %, and full stability. A schematic presentation of monolithic configuration is presented in **Fig. 2.1**.

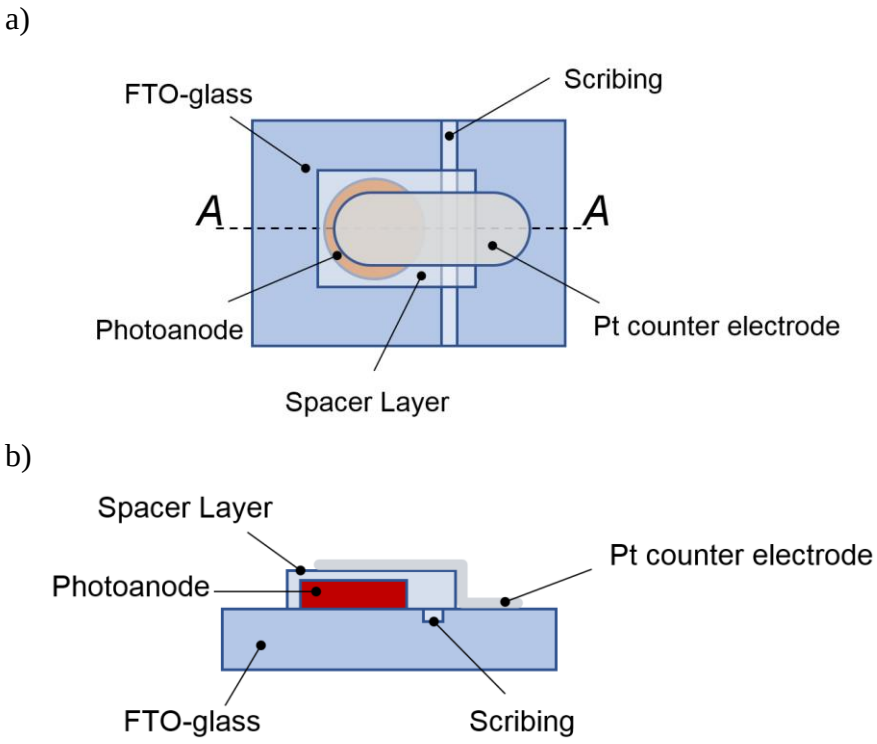

Fig. 2.1 Schematic presentation of a monolithic arrangement of DSSCs: top view (***a***) and cross-section (***b***) along line A-A.

2.2 Experimental

2.2.1 Reagents and materials

FTO-coated glasses (TEC-7; 7 Ω/sq), screen-printable TiO_2 pastes (18NR-T and 18NR-AO), DSSCs electrolyte (EL-HPE) were from GreatCell Solar®. Titanium diisopropoxide bis(acetylacetonate), anhydrous isopropyl alcohol, acetylacetone, hydroxypropyl cellulose (HPC, Mw ~ 100 000), and aqueous solution of colloidal silica (LUDOX® AS-40) were purchased from Sigma-Aldrich®; paste for deposition of ZrO_2 electrical spacers (Zr-Nanoxide ZR/SP), as well as dye N719 (ruthenizer 525-bisTBA), chenodeoxycholic acid (CDA) and hot melt sealant (Meltonix 1170-60, 60 µm Surlyn®) were ordered in Solaronix®. TiO_2 powder (PC 500) from Lyondell®, $TiCl_4$ (99.90 %, Acros Organics) and ammonium hydroxide solution (25 wt.%) from FlukaTM were used.

2.2.2 Preparation of pastes for electrical spacers

Silica-based pastes for electrical spacers were prepared from an aqueous suspension of colloidal silica (LUDOX® AS 40, monodispersed 22 nm particles) with the addition of hydroxypropyl cellulose (HPC, Mw ~ 100 000) as a structure-forming agent. For titania/SiO_2 pastes, titania (PC 500, Lyondell) was added to the formulation in the amount of 10 to 40 wt.% concerning SiO_2. Mass fraction of the solids in the pastes was adjusted to 23 wt.% balancing with distilled water; the mass ratio HPC: water in the pastes was kept at 1:4.8. To prevent the gelation of the pastes, ammonium hydroxide solution was added to the final mixture at the rate of 2.7 ml for 100 g of the paste. The spacer layers formed from these pastes were denoted as $SiO_2@xTiO_2$, where x is the fraction of TiO_2 in the final solid in wt.%.

2.2.3 Fabrication of DSSCs

FTO coating on conducting glasses was laser-scribed (VersaLaser®) to separate the photoanode from the cathode. Textured glasses were then washed in an ethanol solution of KOH (30 g of KOH dissolved in 200 mL of 70 wt.% EtOH) in an ultrasonic bath, rinsed with distilled water, dried in a hot air flow, and cleaned in air plasma.

DSSCs with and without blocking-layers of TiO_2 were prepared. Blocking-layer was applied by spraying of TiO_2 precursor solution (7.0 mL of anhydrous isopropyl alcohol + 0.6 mL diisopropoxide bis(acetylacetonate) + 0.4 mL of acetylacetone) on heated up to 450 ^oC FTO-substrates. As deposited TiO_2 films were annealing at this temperature for 45 min. According to SEM the thickness of the blocking-layer was 80±5 nm.

Circularly shaped photoanodes (0.13 cm^2) were formed by subsequent screen-printing of a transparent mesoporous TiO_2 (18NR-T paste) layer and opaque atop layer (18NR-AO paste). Substrates with TiO_2 films were then heated up to 500 ºC (3 ºC min^{-1}) and sintered for one hour. After sintering, TiO_2 films were treated in a 40 mM $TiCl_4$ aqueous solution for 20 minutes at 70 ºC, dried, and annealed at 500 ºC for one hour. The overall thickness of the photoanodes was 25±2 μm, where 17±1 μm was the mesoporous layer and 8±1 μm was the opaque TiO_2 layer. This arrangement of TiO_2 layers allows 9.8 % of PCE in conventionally assembled DSSCs. Electrical spacer layers in M-DSSCs were made from SiO_2@*x*TiO_2 and commercial ZrO_2, and deposited on photoanode by blade-coating followed by annealing at 500 ºC (3 ºC min^{-1}) for one hour, originating an electrical spacer layer of 28±3 μm. Platinum counter-electrodes (100 ± 20 nm) were deposited on top of the spacer layers by DC magnetron sputtering, like shown in **Fig. 2.1**. Pt layer was slightly smaller than TiO_2 layer, ensuring penetration of sensitizing solution and electrolyte to the photoanode. The low sheet resistance of the sputtered Pt (*ca.* 1.7±0.2 Ω·sq^{-1}) and excellent activity in triiodide reduction determined the choice of sputtered Pt as counter-electrode material.

The sensitization of the photoanodes was performed in a fresh solution of 0.5 mM N719 dye + 5 mM CDA in absolute ethanol. After sensitization the cells were rinsed with absolute ethanol, dried in N_2 flow, and immediately sandwiched with ordinary glass and sealed to the front glass using a hot-pressed thermoplastic gasket. The electrolyte was injected through the holes pre-drilled in the ordinary glass; these holes were later sealed atop with thermoplastic film and lamella glass.

2.2.4 Characterization

The photovoltaic response of the DSSCs was characterized under simulated solar light (AM1.5G, 100 mW·cm^{-2}) driving from a Solar Simulator MiniSol (LSH-7320, Newport). Photocurrent *vs.* potential curves were recorded using an electrochemical workstation Zennium (Zahner).

The spectra of electrochemical impedance were collected in the dark at potential 20 mV below the open-circuit potential of the DSSCs using Autolab (PGSTAT 302 N, Metrohm). The impedance spectra were analyzed using ZView® software.

The incident photon to current conversion efficiency (IPCE) spectra was recorded using a semi-automatic station (Newport). Measurements were made at 2 nm wavelength intervals.

X-ray diffraction (XRD) studies of the SiO_2@*x*TiO_2 spacers were performed using a Philips X'Pert MPD diffractometer (Cu Kα radiation). Surface area and pore size distribution of the spacer layers were assessed by Brunauer-Emmett-Teller (BET) and Barrett-Joyner-Halenda (BJH) methods, respectively, using a Quantachrome AS1 analyzer. Samples were previously degassed for 5 h at

250 ºC. Isotherms of N_2 adsorption/desorption were obtained at 77 K in the range of 1 and 1000 mbar. SEM and EDS characterizations were performed using a desktop SEM Phenom XL microscope. The reflectance spectra were collected using a Shimadzu UV-3600 spectrophotometer equipped with LISR-3100 integrating sphere. $BaSO_4$ powder compact was used for the baseline spectrum.

2.3 Results and Discussion

2.3.1 Characterization of insulating layers

Physical properties of the spacer layer impact significantly the efficiency of M-DSSCs [14,16]. Proper spacer layer should be fairly insulating to block electron flow from photoanode to counter-electrode; should be homogeneously porous for fast ionic charge-transfer between electrodes and last but not least, should have a good reflectivity to send unabsorbed light back to the photoelectrode for better light harvesting.

Fig. 2.2 shows XRD patterns of $SiO_2@xTiO_2$ powders produced by calcinating the pastes at 500 ºC for 1 hour. Silica powders without the addition of TiO_2 exhibit a broad diffraction peak at 2θ *ca.* 22°, typical for amorphous silica [17]. When TiO_2 is added to the formulation, well-defined reflections attributed to anatase (JCPDS #21-1272) are observed; the reflections are broad pointing to the presence of small crystallites. The mean sizes of the crystalline domains calculated from the Debye-Scherrer equation for (101) and (200) singlets using a shape factor of 0.9 were found to be 9 nm.

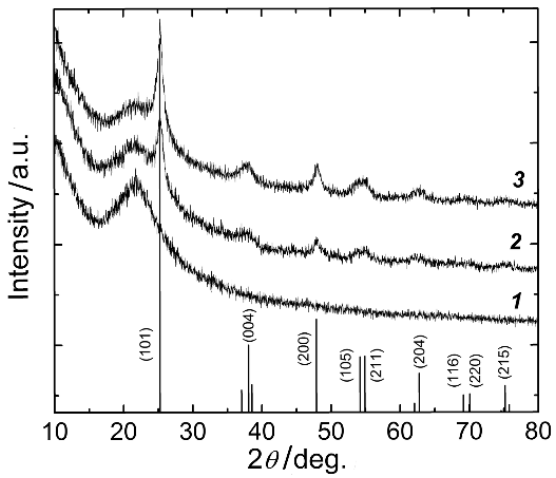

Fig. 2.2 X-ray diffractograms of $SiO_2@xTiO_2$ composites with different mass fraction *x* of TiO_2; patterns **1**, **2** and **3** are for *x* equal 0, 20 and 30 wt.% correspondingly; bar graph is a reference pattern for anatase (JCPDS #21-1272).

BET and BJH analyses showed that titania content in the spacers is not related with the displayed specific surface area and porosity (**Fig. A1**, **Table A1**), within 95 % confidence level. The average specific surface area and diameter of the pores was 140 ± 20 m^2 g^{-1} and 16.5 ± 2.4 nm, respectively.

Secondary electron image of SEM for $SiO_2@xTiO_2$ spacers are presented in **Fig. 2.3**. The spacer layers form a sponge-like porous coating with confined voids as separate defects. Element composition of the spacers determined by EDS (**Fig. A2**, **Table A2**) fits well with the ratio of silica and titania used in the formulations. A trace amount of sodium (less than 0.9 wt.%), coming from LUDOX-AS40 solution, is also observed. The morphology of the insulating layers, loaded with different amounts of TiO_2, remained unchanged until 25-30 wt.% of titania was added.

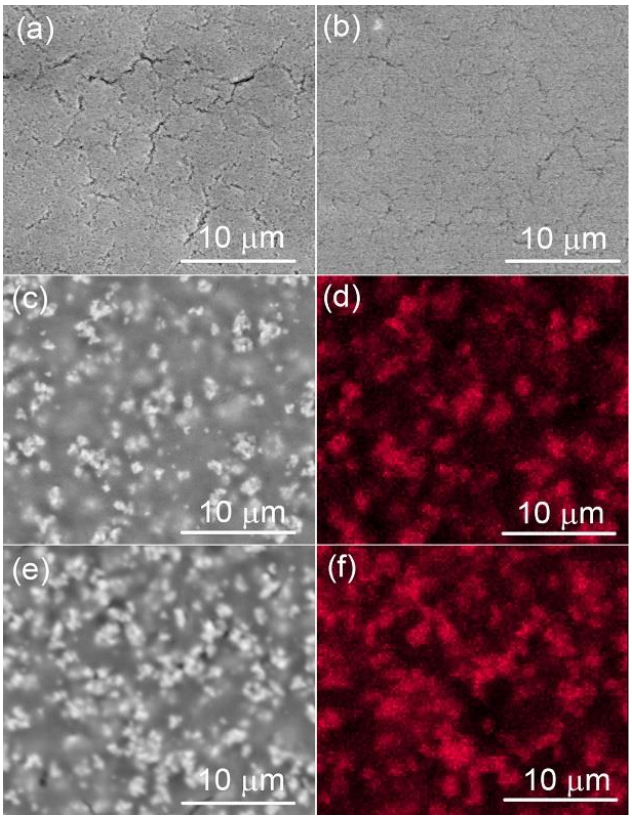

Fig. 2.3 Top-view SEM images of $SiO_2@xTiO_2$ spacer layers with different mass fractions *x* of TiO_2: (***a***), (***b***), (***c***) and (***e***) correspond to *x* = 0, 20, 30 and 40 % respectively; (***d***) and (***f***) are EDS maps of Ti for the surfaces ***c*** and ***e***.

Isolated aggregates with sizes from several nanometers to micrometers are observed in $SiO_2@30TiO_2$ films (**Fig. 2.3c**) making the surface more developed. The aggregates are much bigger than the crystalline domains calculated from the broadening of XRD reflections. EDS mapping (**Fig. 2.3d**) shows that the aggregates are enriched with titanium. When 40 wt.% of titania is added to the spacer, the TiO_2 aggregates turn to contact each other, forming long-range connectivity in distances above 20 μm (**Fig. 2.3e,f**).

Fig. 2.4a presents the reflectance spectra of silica-based spacers deposited on glass, and **Fig. 2.4b** shows their reflectance at 530 nm; 530 nm is the wavelength of the maximum IPCE of DSSCs with N719 dye.

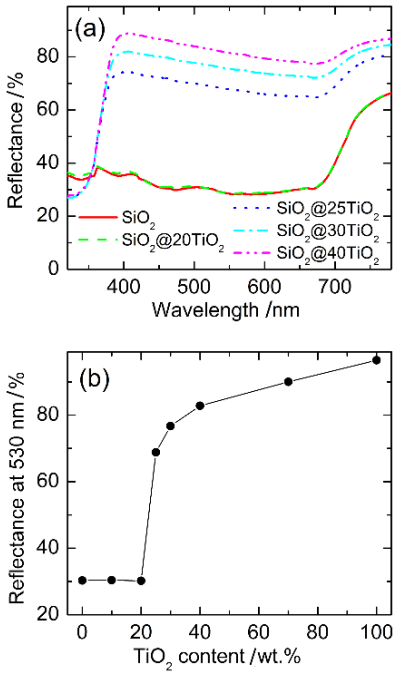

Fig. 2.4 Reflectance of the $SiO_2@xTiO_2$ electrical spacers (***a***) and their reflectance at 530 nm *vs.* mass fraction of TiO_2 (***b***).

The use of just silica nanoparticles in the formulations leads to layers with low reflectance: *ca.* 30 %, which is not enough for an effective backscattering of not absorbed light. The addition of 10 and 20 wt.% of TiO_2 did not cause noticeable changes in the reflectivity of the films. However, when 25-30 wt.% of TiO_2 was added a very sharp increase of reflection up to *ca.* 70-76 % was observed (**Fig. 2.4b**). This jump in reflection correlates well with the appearance of TiO_2 aggregates in the films (**Fig. 2.3c-f**). According to Mie light scattering theory, regardless of whether the material is light absorbing or non-absorbing, for effective light scattering in the range between 500 and 700 nm, particles with sizes above 200 nm are required [18,19]. Indeed, TiO_2 nanoparticles are prone to aggregate; in the lack of effective dispersant, they promptly coalesce [20]. In the formulations for spacer layers, the ratio of hydrophilic dispersant for TiO_2 (HPC) to water was kept constant while the concentration of the solid phase was gradually increased, causing spontaneous aggregation of TiO_2 nanoparticles. Aggregates of TiO_2 contribute to light scattering in the film, thereby increasing the reflectivity of the spacers. The addition of more than 30 wt.% of TiO_2 leads to an extra, though not so drastic, increase in reflectance (**Fig. 2.4**).

Besides light scattering on the aggregates, the higher refractive index of anatase TiO_2 compared to SiO_2 (2.5 and 1.5, respectively), should be taken into account for the reflectance. Further

improvements in the reflectivity might be accomplished by utilizing nanoparticles with higher refractive indices and band gaps above 3.2 eV.

2.3.2 Sensitization of photoanode in M-DSSCs

Good dye uptake is essential to generate high photocurrents. However, excessive dye loading forces the dye molecules to agglomerate [21-25]. The agglomerates ineffectively inject electrons into TiO_2 and, for larger agglomerates, may block the photoanode pores making more difficult the electrolyte diffusion, thereby increasing the charge transfer resistances. In conventional DSSCs, the most effective sensitization occurs within 12-48 hours period when an ethanolic solution of N719 is used [22,25]. DSSCs featuring monolithic arrangement may require a different optimum time for sensitization, since the surface of photoanode is coated with electrical spacer and counter-electrode. The amount of the adsorbed dye is simply controlled by the contact time of the sensitizer solution with titanium dioxide, at a fixed temperature. Surprisingly, the sensitization optimization of photoanode in the assembled monolithic is not usually considered. **Fig. 2.5** presents metrics (PCE, short circuit current density - J_{SC}*;* open circuit potential – V_{OC} and fill factor - FF) for a series of M-DSSCs and conventional DSSCs, depending on the time spent on sensitization. Each photovoltaic parameter was normalized to its maximum value observed during the dye loading test.

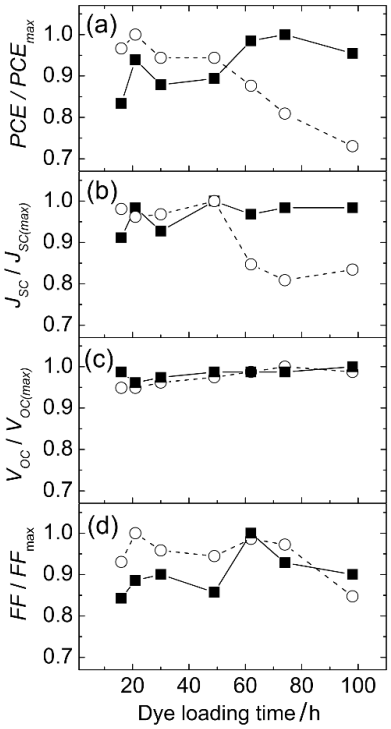

Fig. 2.5 Normalized PCE (***a***), J_{SC} (***b***), V_{OC} (***c***) and FF (***d***) of M-DSSCs (solid lines, filled squares) and conventional DSSCs (dashed lines, circles) *vs*. time of sensitization in an ethanolic solution of N719 dye.

In agreement with previous studies [22,25], conventional DSSCs exhibits the best PCE after *ca.* 20 hours of dye loading (**Fig. 2.5a**), mainly because of the highest FF (**Fig. 2.5d**). After 50 hours of immersion in the dye solution, the PCE rapidly drops due to losses in photocurrent and FF (**Fig. 2.5b,d**), which in turn might be caused by dye aggregation in the photoanode pores [23]. Comparing with conventional DSSCs, for M-DSSC device 3 times longer contacting time (*ca*. 60-70 hours) is required to reach the best performance (**Fig. 2.5a**). J_{SC} in M-DSSCs stabilizes after a particular time of immersion (*ca.* 40 h) and remains almost constant until the end of the test (**Fig. 2.5b**) – 100 h; this may indicate a dye aggregation suppression in the pores of photoanode. The porous spacer layer acts as a filter, which, on the one hand, increases the time required for effective dye loading, but at the same time prevents the access of dye aggregates from solution to the photoanode.

2.3.3 Characterization of M-DSSCs with SiO_2@xTiO_2 spacer layers

Typical photocurrent-potential (*J-V*) curves for M-DSSCs employing several SiO_2@*x*TiO_2 spacer layers are presented in **Fig. 2.6**. From *J-V* curves, the key parameters of the photovoltaic performance were extracted and summarized in **Table 2.1**. For comparison, the performance parameters of M-DSSCs with a commercial insulating layer made from ZrO_2 is added.

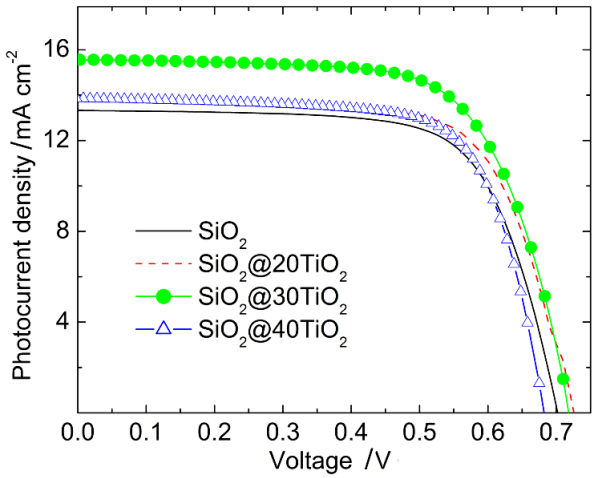

Fig. 2.6 *J-V* curves of M-DSSCs with SiO_2@*x*TiO_2 electrical spacers.

Table 2.1

Photovoltaic metrics of M-DSSCs.

Electrical spacer	V_{OC} / V	J_{SC} / mA·cm^{-2}	FF	PCE / %
ZrO_2	0.71	13.0	0.73	6.7
SiO_2	0.70	13.3	0.69	6.5
SiO_2@10TiO_2	0.71	13.0	0.72	6.6
SiO_2@20TiO_2	0.72	13.8	0.70	6.9
SiO_2@30TiO2	0.72	15.6	0.68	7.6
SiO_2@40TiO2	0.68	13.9	0.71	6.7

PCE of M-DSSCs employing spacer layer made solely from SiO_2 is only 0.2 percentage points less performing than PCE of the cells with commercial ZrO_2 spacer, due to slightly lower V_{OC} and FF. Introducing of 10 and 20 wt.% of TiO_2 into the spacers leads to a subtle increase of PCE. A step PCE improvement was, however, achieved when adding 30 wt.% of TiO_2. The observed increase in photocurrent correlates well with a sharp increase of reflectance of the spacer layer (**Fig. 2.4**); the spacer layer effectively reflects unabsorbed light back to the photoanode forcing photogeneration. For higher titania contents, a drop in V_{OC} and the current density was observed (**Table 2.1**, **Fig. 2.6**). Indeed, anatase is essentially an electronic conductor; above a threshold titania concentration, TiO_2 aggregates (**Fig. 2.3e**) start percolating electricity the in SiO_2@TiO_2 spacer layer, making V_{OC} and photocurrent reduce. IPCE spectra (**Fig. 2.7**) and EIS analyses (**Fig. 2.8**) support this assumption.

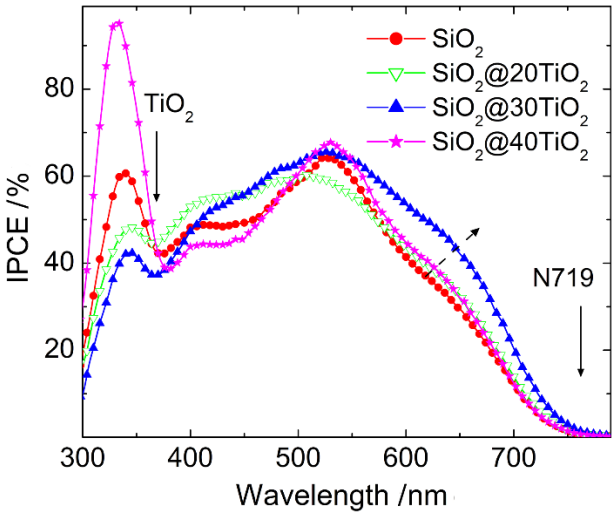

Fig. 2.7 IPCE spectra of M-DSSCs with SiO_2@$x$$TiO_2$ electrical spacers.

The onset of photocurrent quantum yield below 760 nm fits well with transition from ground state of the dye to its lowest excited state localized on TiO_2 (1.58 eV) [26], the maximum at 530 nm correlates with the first absorption band of N719 centered in 521 nm; it is 9 nm positively shifted due

to strong coupling between dye and TiO_2 and delocalization of the excited electron into the semiconductor [27]. The band below 370 nm responses for photocurrent from anatase TiO_2 (E_g = 3.2 eV). The benefit of the reflectance of the spacer layer SiO_2@30TiO_2 on produced photocurrent manifests itself as an increase in IPCE spectrum above 450 nm. Introducing 40 wt.% of TiO_2 in the spacer layer resulted in a higher photocurrent response from TiO_2 (below 370 nm), pointing to the participation of TiO_2 from the spacer layer in the photoelectrochemical process. The sensitized photocurrents (quantum yield in 400-750 nm region) are reduced; photoelectrons flow from photoanode to TiO_2 aggregates in the spacer layer and recombine with electrolyte.

Nyquist plots in **Fig. 2.8** show EIS response of M-DSSCs with different spacer layers.

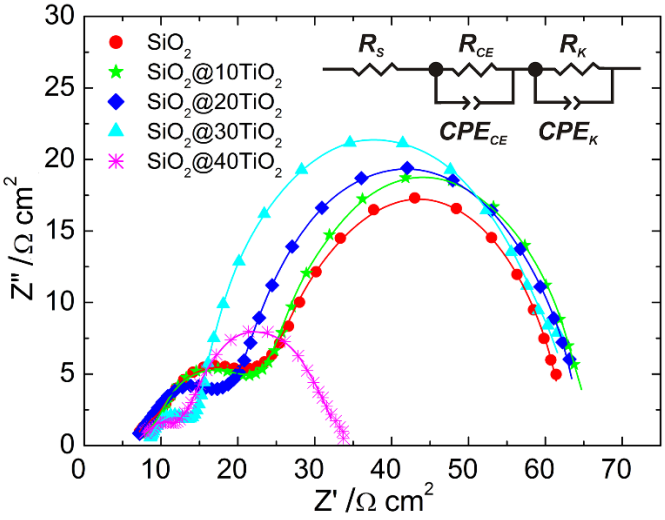

Fig. 2.8 EIS response in Nyquist plots for M-DSSCs with SiO_2@$x$$TiO_2$ electrical spacers.

EIS spectra were fitted using an equivalent electrical circuit drawn in the inset to **Fig. 2.8**. CPE_{CE} and CPE_K are constant phase elements associated with counter-electrode/electrolyte and TiO_2/electrolyte interfaces, respectively. Recombination resistance in the TiO_2/electrolyte interface (R_K), charge-transfer resistance in the electrolyte/counter-electrode interface (R_{CE}) and series resistance (R_S) of the M-DSSCs were derived from fitting the model to the experimental results and are presented in **Table 2.2**.

Table 2.2

Resistances (in $\Omega \cdot cm^2$) of the M-DSSCs obtained by fitting the model to the experimental Nyquist plots.

Electrical spacer	R_S	R_{CE}	R_K
SiO_2	7.2	20.4	35.4
SiO_2@10TiO_2	8.0	15.4	40.8
SiO_2@20TiO_2	7.2	14.5	43.9
SiO_2@30TiO_2	8.6	6.2	47.4
SiO_2@40TiO_2	7.9	9.6	28.9

The R_S values, related to the resistances of FTO, counter-electrode, electrolyte, and electrical contacts, are similar for all M-DSSCs devices. Increasing the concentration of TiO_2 in the film leads to a gradual decrease of the R_{CE}. The most pronounced drop in R_{CE} (2.3 times) is observed when the amount of TiO_2 in the spacer layer is increased from 20 to 30 wt.%. This drop of R_{CE} was assigned to the more developed surface of the SiO_2@30TiO_2 spacer layer (**Fig. 2.3c,d**). The active surface area of Pt film is larger on a rough spacer, and the values of charge-transfer resistance per geometric area are smaller.

Recombination resistance R_K at the TiO_2/electrolyte interface remains practically constant until 40 wt.% of TiO_2. With a spacer layer SiO_2@40TiO_2 the recombination resistance clear drops. This degradation on the insulating properties of the spacer is due to the formation of long-range interconnections of titania aggregates (**Fig. 2.3e,f**); interconnections with sizes comparable with the thickness of the insulating layer (*ca*. 20 μm) are responsible for the electron percolating in SiO_2@40TiO_2 film and recombination with electrolyte.

Due to high reflectivity and good insulating properties, the SiO_2@30TiO_2 spacer layer in M-DSSCs allows attaining a PCE of 7.6 %. To get the best performing M-DSSCs, a pinhole-free blocking-layer of TiO_2 between the FTO layer and the photoanode was applied. The blocking-layer suppresses recombination in the FTO/electrolyte interface. As a result, J_{SC} and V_{OC} were increased to 17.3 $mA \cdot cm^{-2}$ and 0.73 V, respectively (**Fig. 2.9a**), and the PCE was improved to 8.4 %.

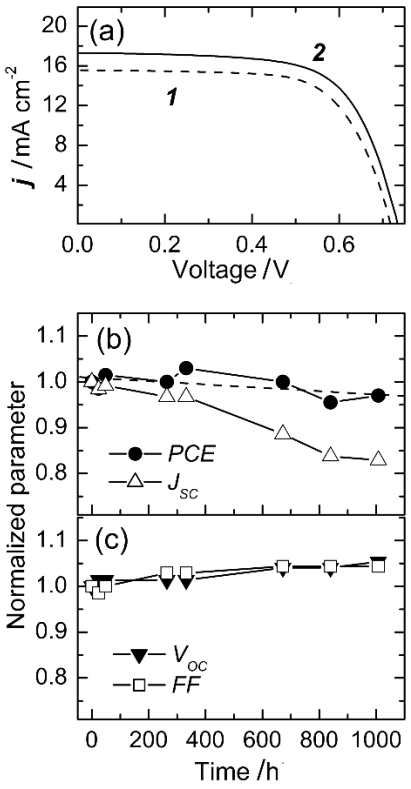

Fig. 2.9 (***a***) *J-V* curves of M-DSSCs with SiO_2@30TiO_2 electrical spacer without blocking-layer (**1**) and with TiO_2 blocking-layer (**2**); history of PCE and J_{SC} (***b***), V_{OC} and FF (***c***) for the best performing M-DSSC.

PCE of the cells with an aperture mask was found to be 8.3 % - the highest reported up to now PCE of M-DSSC with liquid electrolyte. The history of PCE for M-DSSCs was followed during 1000 h under natural aging (**Fig. 2.9b,c**). The PCE history is mostly affected by the current attenuation (**Fig. 2.9b**), frequently caused by electrolyte escape from the cell when polymeric sealants are used [28]. The decrease in current was, however, balanced with an increase in V_{OC} and FF (**Fig. 2.9c**). As a result, the PCE deterioration factor obtained from the linear fit of PCE history of M-DSSCs is low, *ca*. $(8.7\pm0.1)\cdot10^{-4}$ per day.

2.4 Conclusions

SiO_2-based spacer layers derived from water-based formulations were developed for producing energy-efficient M-DSSCs. In optimized sensitization conditions, M-DSSCs employing silica nanoparticles solely in the spacer layers displayed a PCE of 6.5 %; only 0.2 percentage points less than that of the cells with commonly used spacers obtained from ZrO_2-terpineol pastes. The addition of *ca.* 30 wt.% of anatase nanoparticles to the spacer layer originated a very sharp increase in the reflectance due to spontaneous agglomeration of the TiO_2 nanoparticles in the film; TiO_2 aggregates

with sizes ranging from tenths to several microns cause Mie light scattering, allowing scattering the unabsorbed light back to the photoanode, improving drastically photocurrent quantum yield above 450 nm. At titania content above 30 wt.% in the spacer layer, TiO_2 agglomerates tend to form long-range electric connectivities, paving photoelectrons leakage from photoanode to counter-electrode. This short circuit promotes back recombination of photoelectrons with electrolyte, suppressing sensitized photocurrents in the wavelength range 400-750 nm. The best energy performing M-DSSC with SiO_2@30TiO_2 spacer layer delivered a PCE of 8.3 % when an aperture mask was used; the highest up to date reported PCE of liquid-junction M-DSSCs.

Acknowledgments

The authors would like to acknowledge the fruitful scientific discussions with Dr. José Maçaira, and are grateful to Cátia Azenha and C. Mateos-Pedrero for the BET analysis. F. Santos and C. Hora acknowledge the FCT (Foundation for Science and Technology) for the doctoral grants SFRH/BD/132388/2017 and SFRH/BD/129761/2017, respectively. This work also financial supported by the BI-DSC project financed by ERC (Grant Agreement no. 321315); the SunStorage project funded by ERDF through COMPETE2020 – OPCI; the project POCI-01-0145-FEDER-006939 – LEPABE; the project NORTE-01-0145-FEDER-000005 - LEPABE-2-ECO-INNOVATION, FEDER - COMPETE2020, OPCI, NORTE2020. The authors are also thankful to the Materials Centre of the University of Porto.

References

[1] J. Gong, K. Sumathy, Q. Qiao, Z. Zhou, Review on dye-sensitized solar cells (DSSCs): Advanced techniques and research trends, *Renew. Sustain. Energy Rev.*, 2017, 68, 234–246. DOI: 10.1016/j.rser.2016.09.097.

[2] A. Hinsch, W. Veurman, H. Brandt, K. Flarup Jensen, S. Mastroianni, Status of dye solar cell technology as a guideline for further research, *ChemPhysChem*, 2014, 15, 1076–1087. DOI: 10.1002/cphc.201301083.

[3] A. Fakharuddin, R. Jose, T.M. Brown, F. Fabregat-Santiago, J. Bisquert, A perspective on the production of dye-sensitized solar modules, *Energy Environ. Sci.*, 2014, 7, 3952–3981. DOI: 10.1039/c4ee01724b.

[4] BIPV (Building Integrated Photovoltaics) – H.Glass. from <http://h.glass/bipv/>.

[5] M.A. Green, Y. Hishikawa, E.D. Dunlop, D.H. Levi, J. Hohl-Ebinger, M. Yoshita, A.W.Y. Ho-Baillie, Solar cell efficiency tables (version 53), *Prog. Photovoltaics Res. Appl.*, 2019, 27, 3–12. DOI: 10.1002/pip.3102.

[6] S. Mathew, A. Yella, P. Gao, R. Humphry-Baker, B.F.E. Curchod, N. Ashari-Astani, I. Tavernelli, U. Rothlisberger, M.K. Nazeeruddin, M. Grätzel, Dye-sensitized solar cells with 13% efficiency achieved through the molecular engineering of porphyrin sensitizers, *Nat. Chem*., 2014, 6, 242–247. DOI: 10.1038/nchem.1861.

[7] K. Kakiage, Y. Aoyama, T. Yano, K. Oya, J. Fujisawa, M. Hanaya, Highly-efficient dye-sensitized solar cells with collaborative sensitization by silyl-anchor and carboxy-anchor dyes, *Chem. Commun*., 2015, 51, 15894–15897. DOI: 10.1039/C5CC06759F.

[8] A. Kay, M. Grätzel, Low cost photovoltaic modules based on dye sensitized nanocrystalline titanium dioxide and carbon powder, *Sol. Energy Mater. Sol. Cells*, 1996, 44, 99–117. DOI:10.1016/0927-0248(96)00063-3.

[9] Y. Takeda, N. Kato, K. Higuchi, A. Takeichi, T. Motohiro, S. Fukumoto, T. Sano, T. Toyoda, Monolithically series-interconnected transparent modules of dye-sensitized solar cells, *Sol. Energy Mater. Sol. Cells*, 2009, 93, 808–811. DOI: 10.1016/j.solmat.2008.09.054.

[10] Kroon, J.M., 2005. Energy Research Center report, ECN-C-05-078, 1–41.

[11] G. Liu, H. Wang, X. Li, Y. Rong, Z. Ku, M. Xu, L. Liu, M. Hu, Y. Yang, P. Xiang, T. Shu, H. Han, A mesoscopic platinized graphite/carbon black counter electrode for a highly efficient monolithic dye-sensitized solar cell, *Electrochim. Acta*, 2012, 69, 334–339. DOI: 10.1016/j.electacta.2012.03.012.

[12] J. Kwon, N.G. Park, J.Y. Lee, M.J. Ko, J.H. Park, Highly efficient monolithic dye-sensitized solar cells, *ACS Appl. Mater. Interfaces*, 2013, 5, 2070–2074. DOI: 10.1021/am302974z.

[13] F. Behrouznejad, N. Taghavinia, N. Ghazyani, Monolithic dye sensitized solar cell with metal foil counter electrode, *Org. Electron.*, 2018, 57, 194–200. DOI: 10.1016/j.orgel.2018.03.009.

[14] S.J. Thompson, N.W. Duffy, U. Bach, Y.B. Cheng, On the role of the spacer layer in monolithic dye-sensitized solar cells, *J. Phys. Chem. C*, 2010, 114, 2365–2369. DOI: 10.1021/jp907967h.

[15] S. Ito, K. Takahashi, Fabrication of monolithic dye-sensitized solar cell using ionic liquid electrolyte, *Int. J. Photoenergy*, 2012, ID 915352. DOI: 10.1155/2012/915352.

[16] L. Vesce, R. Riccitelli, G. Mincuzzi, A. Orabona, G. Soscia, T.M. Brown, A. Di Carlo, A. Reale, Fabrication of spacer and catalytic layers in monolithic dye-sensitized solar cells, *IEEE J. Photovoltaics*, 2013, 3, 1004–1011. DOI: 10.1109/JPHOTOV.2013.2262374.

[17] S. Chaudhary, D. Rohilla, S.K. Mehta, Surfactant adsorption and aggregate structure of silica nanoparticles: A versatile stratagem for the regulation of particle size and surface modification, *Mater. Res. Express*, 2014, 1, 015011. DOI: 10.1088/2053-1591/1/1/015011.

[18] T.G. Deepak, G.S. Anjusree, S. Thomas, T.A. Arun, S.V. Nair, A. Sreekumaran Nair, A review on materials for light scattering in dye-sensitized solar cells, *RSC Adv.*, 2014, 4, 17615–17638.DOI: 10.1039/c4ra01308e.

[19] Nursam, N.M., J. Hidayat, Shobih, L.M. Pranoto, E.S. Rosa, A comparative study between titania and zirconia as material for scattering layer in dye-sensitized solar cells, *J. Phys. Conf. Ser.*, 2018, 1011. DOI: 10.1088/1742-6596/1011/1/012003.

[20] B. Faure, G. Salazar-Alvarez, A. Ahniyaz, I. Villaluenga, G. Berriozabal, Y.R. De Miguel, L. Bergström, Dispersion and surface functionalization of oxide nanoparticles for transparent photocatalytic and UV-protecting coatings and sunscreens, *Sci. Technol. Adv. Mater.*, 2013, 14, 023001. DOI: 10.1088/1468-6996/14/2/023001.

[21] L. Zhang, J.M. Cole, Dye aggregation in dye-sensitized solar cells, *J. Mater. Chem. A*, 2017, 5, 19541–19559. DOI: 10.1039/c7ta05632j.

[22] E. Dell'Orto, L. Raimondo, A. Sassella, A. Abbotto, Dye-sensitized solar cells: Spectroscopic evaluation of dye loading on TiO_2, *J. Mater. Chem.*, 2012, 22, 11364–11369. DOI: 10.1039/c2jm30481c.

[23] P. Marquet, G. Andersson, A. Snedden, L. Kloo, R. Atkin, Molecular scale characterization of the titania-dye-solvent interface in dye-sensitized solar cells, *Langmuir*, 2010, 26, 9612–9616. DOI: 10.1021/la100193w.

[24] L. Ellis-Gibbings, V. Johansson, R.B. Walsh, L. Kloo, J.S. Quinton, G.G. Andersson, Formation of N719 dye multilayers on dye sensitized solar cell photoelectrode surfaces investigated by direct determination of element concentration depth profiles, *Langmuir*, 2012, 28, 9431-9439. DOI: 10.1021/la100193w.

[25] J.K. Kim, H. Seo, M.K. Son, I. Shin, J. Hong, H.J. Kim, The analysis of the change in the performance and impedance of dye-sensitized solar cell according to the dye-adsorption time, *Curr. Appl. Phys*, 2010, 10, S418–S421. DOI: 10.1016/j.cap.2010.02.024.

[26] F. De Angelis, S. Fantacci, E. Mosconi, M.K. Nazeeruddin, M. Grätzel, Absorption Spectra and Excited State Energy Levels of the N719 Dye on TiO_2 in Dye-Sensitized Solar Cell Models, *J. Phys. Chem. C*, 2011, 115, 8825–8831. DOI: 10.1021/jp111949a.

[27] K. Awasthi, H.Y. Hsu, E.W.G. Diau, N. Ohta, Enhanced charge transfer character of photoexcited states of dye sensitizer on the N719 / TiO_2 interface as revealed by electroabsorption

spectra, *J. Photochem. Photobiol. A Chem*., 2014, 288, 70–75. DOI: 10.1016/j.jphotochem.2014.05.001.

[28] J. Maçaira, L. Andrade, A. Mendes, Laser sealed dye-sensitized solar cells: Efficiency and long term stability, *Sol. Energy Mater. Sol. Cells*, 2016, 157, 134–138. DOI: 10.1016/j.solmat.2016.05.016.

CHAPTER 3

EFFICIENT LIQUID JUNCTION MONOLITHIC COBALT-MEDIATED DYE-SENSITIZED SOLAR CELLS FOR SOLAR AND ARTIFICIAL LIGHT CONVERSION

Adapted from the peer-reviewed article:

F. Santos, C. Hora, D. Ivanou, A. Mendes, Efficient Liquid-Junction Monolithic Cobalt-Mediated Dye-Sensitized Solar Cells for Solar and Artificial Light Conversion. *ACS Appl. Energy Mater.*, 2021, 4, 5, 5050–5058. DOI: 10.1021/acsaem.1c00616.

3

Efficient liquid junction monolithic cobalt-mediated dye-sensitized solar cells for solar and artificial light conversion

3.1 Introduction

Dye-sensitized solar cells (DSSCs) are third-generation photovoltaic devices featuring low cost, ease of fabrication, and environmental friendliness [1,2]. Due to the decent power conversion efficiency (PCE) of scattered and dim light, much-surpassing PCE of silicon [3,4], DSSCs are considered a feasible approach for outdoor building-integrated photovoltaics [5,6]. Nowadays, the exponentially growing number of low-power-consumption electronic devices, such as the Internet of Things (IoT) and wireless sensors to name a few, turned the development of cordless powering strategies for indoor applications absolutely relevant. It triggered the DSSCs to develop as favorable indoor photovoltaic devices [7]. DSSCs effectively compete with other PV technologies offering amazingly high PCE *ca.* 30 % under artificial light [2,8-10]; pleasant colorful appearance, the possibility of incarnating in semitransparent and flexible devices [11]; could be aesthetically integrated into the working and living interior; DSSCs are safe, in the sense, they are free from toxic soluble lead or tin compounds.

Since the seminal breakthrough in 1991 [12], the decades of DSSCs research led to the certified PCE of *ca.* 12 % [13], still employing the family of Ru-dyes and iodide electrolyte discovered from the outset [12,14]. The renaissance of the DSSCs happened with the discovery of new one-electron transfer high potential redox shuttles, dyes with high extinction coefficient, broad absorption spectra, and electron recombination suppressing behavior [15,16]. The state-of-the-art best-performing DSSCs are liquid-junction devices with Co(III)/Co(II) and Cu(II)/Cu(I) redox shuttles for generating high output potential of *ca.* 1 V [10,17]. Cobalt redox couple and porphyrin sensitizers allow attaining PCE of 13 % [16,17]; implementation of co-sensitization strategies with thienoindols yielded as high PCE as 14.2 % [18]. DSSCs with Cu(II)/Cu(I) redox mediator were presented in 2005 [19], nowadays achieving promising PCE *ca*. 13 % [8-10].

Efficient DSSCs are assembled in a so-called "conventional" architecture where the photoanode and counter-electrode, each on a separate conducting glass, are placed opposite with the microgap in-between and electrolyte filling this gap. An alternative design, the so-called "monolithic" (M-DSSCs) design, photoanode and counter-electrode are in the same glass and an electrical spacer layer is used to separate both electrodes [11]. The monolithic arrangement allows *ca.* 30 % reduction in material costs [20] and is very straightforward for assembly in module configuration [11], making it the most promising architecture for upscaling these devices. However, the PCE of the M-DSSCs is below their conventional counterparts [21-24], primarily due to the spacer layer. The spacer layer creates extra resistance for the electrolyte diffusion, increasing the charge transport resistance, and inefficiently scatters unabsorbed light back to the photoanode.

Since the first reported in 1996 [25] with PCE of 6.7 %, M-DSSCs progressed due to the development of new catalytic and low-cost counter-electrodes [21-23] and electrical spacer layers [24,26,27]. Implementation of counter-electrodes made from platinized graphite/carbon-black resulted in PCE of 7.6 % [21]; physically attached PEDOT films and platinized Cr foil counter-electrodes allowed reaching a PCE of 7.7 % and 8.0 %, respectively [22,23]. The use of a highly reflective electrical spacer layer rendered a M-DSSC with the highest reported PCE of 8.3 % [27]. Surprisingly, all the advances in liquid junction M-DSSC are presented so far only for the original archetype of the iodide-mediated devices.

In this work, we report M-DSSCs built using Co(III/II)tris(bipyridyl) redox shuttle and porphyrin sensitizer YD2-*o*-C8. Cobalt-mediated monolithic devices require reference devices with high PCE, which preferably should be feasible for assembly from readily existing commercial parts and reactants. The challenge of producing efficient M-DSSCs from solely commercially available materials is addressed. The most commonly used in DSSCs electrocatalysts were assessed for counter-electrodes – Pt nanoparticles, Pt metal foil, graphite/carbon-black, PEDOT:PSS; exchange current density and apparent activation energy were determined and related to the performance in the M-DSSCs. To the best of our knowledge, we are reporting for the first time on the apparent activation energy of Pt, graphite/carbon-black, and PEDOT:PSS catalysts for the electron transfer in $[Co(bpy)_3]^{(3+/2+)}$ complexes. Spectral distribution of the photocurrent quantum yield revealed the efficient electrical spacer layer made from polydisperse rutile particles. Dye loading time and electrolyte composition were optimized to produce a record break liquid-junction monolithic device displaying 1-sun PCE of 9.5 %, which is the highest of monolithic type DSSCs reported so far. A PCE of *ca.* 22 % was attained under artificial 1000 lx light, making the developed M-DSSCs very attractive and straightforward for indoor light conversion.

3.2 Experimental

3.2.1 Reagents and materials

FTO-coated glasses (TEC-7; 7 $\Omega \cdot sq^{-1}$) and screen-printable TiO_2 pastes (30NR-D and WER2-O) were purchased from GreatCell Solar®. Titanium diisopropoxide bis(acetylacetonate), anhydrous isopropyl alcohol, acetylacetone, lithium perchlorate, dimethyl sulfoxide (≥99.90 %), 4-*tert*-butylpyridine (TBP) and lithium perchlorate ($LiClO_4$, 99.90 %) were ordered in Sigma-Aldrich®. Screen-printable graphite/carbon-black paste (Elcocarb B/SP), platinum nanoparticles paste (Platisol T/SP), and zirconium dioxide paste (Zr-Nanoxide ZR/SP), as well as hot melt sealant (Meltonix 1170-60, 60 μm Surlyn®) were from Solaronix®. Co(II/III)tris(bipyridyl)tetracyanoborate complexes (Eversolar Co-200 and Co-300) and donor-π-bridge-acceptor zinc porphyrin sensitizer (YD2-*o*-C8) were acquired from Everlight. Titanium tetrachloride (99.90 %, Acros Organics) and PEDOT:PSS aqueous solution (Clevios^{TM}), as well ammonium hydroxide solution (25 wt%) were from Fluka^{TM}.

3.2.2 Fabrication of DSSCs

M-DSSCs devices were assembled according to the configuration described in Chapter 2. An 80±5 nm TiO_2 blocking-layer was deposited by spray pyrolysis at 450 ºC. The precursor solution was composed of 7.0 mL of anhydrous isopropyl alcohol, 0.6 mL of titanium diisopropoxide bis(acetylacetonate) and 0.4 mL of acetylacetone. After the spray deposition, TiO_2 layer was annealed at 450 ºC for 45 minutes.

A 7±1 μm mesoporous TiO_2 (30NR-D paste) layer with 0.13 cm^2 of the active area was deposited by screen-printing and sintered at 500 ºC for 1 hour. Then, the TiO_2 films were immersed in a 40 mM $TiCl_4$ aqueous solution at 70 ºC for 30 minutes, dried, and annealed at 500 ºC for 1 hour.

A 6±1 μm opaque ZrO_2 layer (Zr-Nanoxide ZR/SP), a 6±1 μm scattering reflector TiO_2 layer (WER2-O) were used as commercial electrical spacers. The platinum counter-electrode layer was deposited by DC magnetron sputtering; graphite/carbon-black (Elcocarb B/SP) layer was deposited by doctor-blading and sintered for 45 minutes at 420 ºC; PEDOT:PSS layer was formed by spin-coating of PEDOT:PSS commercial solution (Clevios^{TM}) mixed with 5 % of DMSO, followed by annealing at 120 ºC for 15 minutes.

The sensitization was performed using a fresh solution of 0.2 mM YD2-*o*-C8 dye in ethanol/toluene 3:1 volume ratio. Then, the M-DSSC were rinsed in absolute ethanol, dried in N_2 flow, and sandwiched with an ordinary glass using a hot-pressed thermoplastic sealant. The

electrolyte was composed of 0.165 M Co(II) and 0.045 M Co(III) tris(bipyridyl)tetracyanoborate complexes, 0.8-1.4 M TBP and 0.1 M $LiClO_4$. After electrolyte injection through the pre-drilled holes in the ordinary glass, the holes were sealed with a thermoplastic film and a lamella glass.

3.2.3 Fabrication of symmetrical half-cells

The materials used at the counter-electrodes were deposited on FTO substrates by different techniques: platinum metal by DC magnetron sputtering, platinum nanoparticles (Platisol T/SP) layer by doctor-blading, graphite/carbon-black (Elcocarb B/SP) layer by screen-printing and PEDOT:PSS layer by spin-coating. Two identical FTO substrates coated with the same material were sandwiched using a thermoplastic sealant. The electrolyte was injected through the pre-drilled holes in one of the electrodes and the holes were sealed.

3.2.4 Characterization

The photovoltaic performance of the M-DSSC was characterized under simulated solar light (AM1.5G, 100 $mW \cdot cm^{-2}$) driving from a Solar Simulator MiniSol (LSH-7320, Newport), and under artificial light (600 lx and 1000 lx) using a LED lamp (Osram, Class A+, 60 W, 2700 K) as the light source. A radiometer Delta Ohm HD 2102.2 was used to determine the power of the light derived by the LED lamp. A Zennium (Zahner) electrochemical station was used to record photocurrent *vs.* potential characteristics.

The spectra of electrochemical impedance were collected in dark at -0.80 V using an Autolab electrochemical station (PGSTAT 302 N, Metrohm). ZView® software was used to analyze the impedance spectra.

The incident photon to current conversion efficiency (IPCE) spectra was recorded using a semi-automatic station (Newport). Measurements were performed at 2 nm wavelength intervals between 300-800 nm.

The electrocatalytic activity of counter-electrodes was analyzed at a temperature range between -5 ºC and 60 ºC measuring the electrochemical impedance spectra at 0 V bias using symmetrical half cells. An in-house made experimental setup [27] was used to control the operating temperature of the half cells.

The surface morphology of the counter-electrode materials was analyzed using Quanta 400 FEG ESEM microscope. The reflectance spectra of the electrical spacer layers were measured using Shimadzu UV-3600 spectrophotometer equipped with LISR-3100 integrating sphere, being used $BaSO_4$ powder compact for baseline.

3.3 Results and Discussion

3.3.1 Characterization of counter-electrodes for M-DSSCs

The counter-electrode in M-DSSC must provide efficient electrochemical regeneration of Co(III) species continuously produced at the photoanode. Seminal works on cobalt-mediated DSSCs report surprisingly high PCE of *ca.* 10-12 % for the devices assembled with conventional counter-electrodes made from thermally activated Pt nanoparticles (Pt_{NP}) FTO-glass [28,29]. Further studies suggest that Pt_{NP} counter-electrodes show insufficient electrochemical activity to reduce Co(III) complexes [30-38]. More efficient counter-electrodes were based on graphene [30,31], tellurium-graphene composite [32], PEDOT [33] and PEDOT-graphene composite [34], poly(3,4-alkylthiophenes) [35], polyaniline [36], carbon-black [37] and carbon-graphene composite [38]. The present report assesses the use of Pt_{NP} deposited on FTO, Pt metal film (Pt_{Met}), graphite/carbon-black (GCB) composite, and PEDOT:PSS.

Apart from the electrocatalytic activity towards the redox reaction, the specific surface area of the counter-electrode is critical, as polarization and charge transfer resistances decrease with the interfacial area electrode/electrolyte [33,34]. The morphology of the electrodes was studied by SEM. **Fig. 3.1**. presents the secondary electron image of SEM for the selected materials.

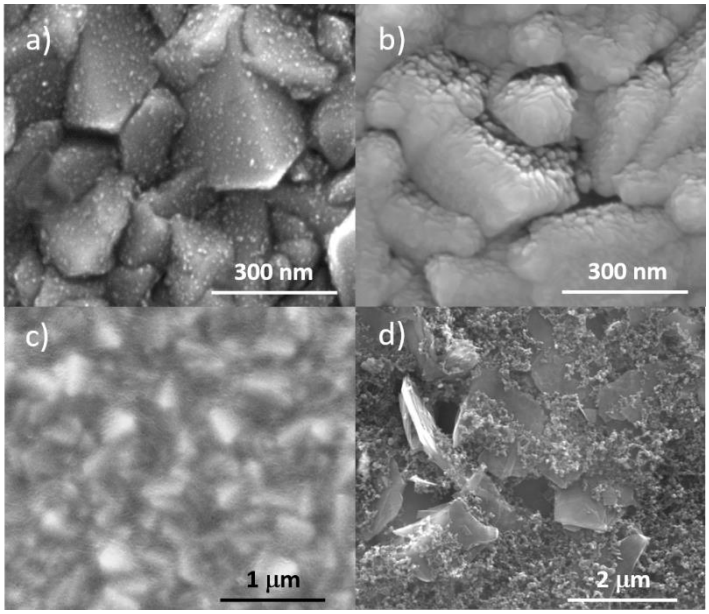

Fig. 3.1 Top-view SEM images of Pt_{NP} (***a***); Pt_{Met} (***b***); PEDOT:PSS (***c***) and GCB (***d***) on FTO-glass.

Conventional thermal activation of the electrode with platinum leads to the formation of a very sparse layer of Pt particles with sizes of *ca.* 8 nm (**Fig. 3.1a**). The Pt film obtained by magnetron sputtering overlays the substrate, repeating the FTO topography (**Fig. 3.1b**). PEDOT:PSS coat

produces a smooth continuous layer (**Fig. 3.1c**). Graphite/carbon-black (GCB) coating is highly heterogeneous with the most developed surface among the others; carbon-black nanoparticles randomly distributed over graphite microplates, ensure high porosity and large specific surface area (**Fig. 3.1d**). The thickness of the layers determined from the cross-section of the samples was 0.1, 0.3, and 15 μm for Pt_{Met}, PEDOT:PSS, and GCB layers, respectively.

Electrochemical and electrocatalytic activity of the cathode materials were analyzed in thin symmetrical half cells [30,32,39-41]. Regarding the counter-electrode, good electrochemical activity means the ability of the electrode to yield high current density with minimal losses of the applied potential. This is typically assessed either by the exchange current density (J_0) or charge transfer resistance (R_{CE}), which are related by **eq. (3.1)** [30,41]:

$$J_0 = \frac{RT}{nFR_{CE}} \tag{3.1}$$

where R is the universal gas constant, T is the temperature, n is the number of electrons, and F is the Faraday constant. Both R_{CE} and J_0 depend on the electrode effective surface area, meaning that the same material prepared with a higher specific surface area will show lower R_{CE} and higher current density. Apart from the developed surface, the electrochemical activity of the counter-electrode is primarily related to the catalytic properties of the material used, which means that the catalytic activity of this material increases as the apparent activation energy (E_a) of charge transfer decreases, **eq. (3.2)** [41]:

$$J_0 = J_{inf} \times \exp\left(-\frac{E_a}{RT}\right) \tag{3.2}$$

where J_{inf} is the J_0 at infinite temperature. The apparent activation energy, E_a, is the most important factor related to the catalytic activity, as it appears in the exponential term of **eq. (3.2).** Surprisingly, no estimates of E_a values for the counter-electrode materials in cobalt electrolytes have been reported so far. Arrhenius equation, **eq. (3.2**), allows the determination of E_a from the temperature dependence of J_0, wherein J_0 could be calculated using **eq. (3.1)** from R_{CE}.

To determine the R_{CE}, the EIS study of the symmetrical half-cells was performed. **Fig. 3.2** shows the impedance response at different temperatures for the half-cells with Pt_{NP}, Pt_{Met}, GCB and PEDOT:PSS electrodes.

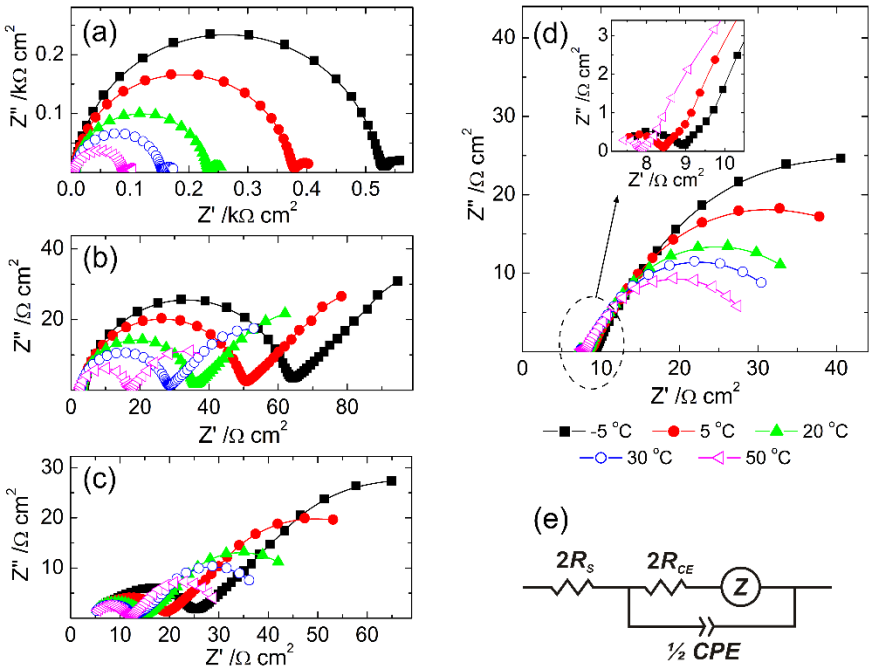

Fig. 3.2 Typical Nyquist plots for the EIS response of dummy cells with electrodes made from Pt_{NP} (***a***), Pt_{Met} (***b***), PEDOT:PSS (***c***), GCB (***d***), and equivalent electrical circuit [30] used for fitting the spectra (***e***).

For all materials studied, the Nyquist diagrams display two well-defined features. The first one appears at high frequencies as a semi-circle close to the origin of the plot and assigned to the R_{CE} at the interface electrode/electrolyte. The second feature appears at medium frequencies and is related to ionic diffusion. In cells with electrodes of Pt_{NP}, Pt_{Met}, and PEDOT:PSS, this feature starts as a line close to *ca*. 45° and bends downwards the abscissa axis for lower frequencies. Such a pattern is typical for the space confined diffusion; finite-length Warburg element (***Z*** is equal to $\boldsymbol{W_S}$ in **Fig. 3.2e**). In the cells with GCB electrodes, the Nyquist shape in the diffusion region fits better to the de Levie's model for semi-infinite length [42] and in the **Fig.3.2e, *Z*** is equal to $\boldsymbol{L_o}$, which is completely consistent with the porous structure and thickness of few microns of the GCB film. The EIS response of the half-cells was fitted to the equivalent circuits in **Fig. 3.2e**; R_{CE} at different temperatures was extracted from the model, J_0 was calculated using **eq. (3.1)** and listed in **Table B1**. **Fig. 3.3** shows the Arrhenius plots for the J_0 with different electrodes.

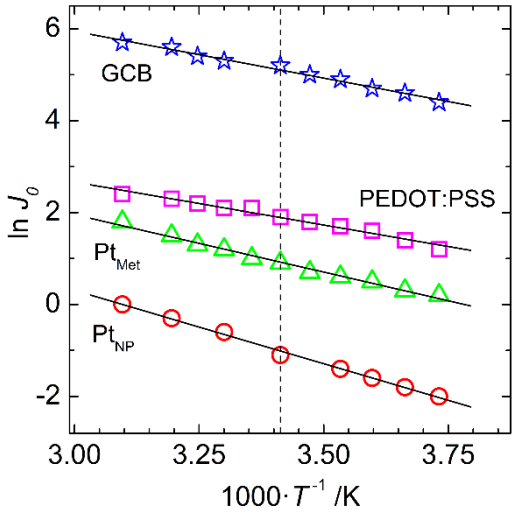

Fig. 3.3 Arrhenius plots of the J_0 for different counter-electrodes. A vertical dashed line is to guide the eyes for a room temperature of 20 ºC.

The Arrhenius behavior as a function of the temperature is observed for all materials studied in the range of temperatures from -5 to 60 °C. The values of E_a for electron transfer obtained for Pt_{NP}, Pt_{Met}, PEDOT:PSS, and GCB are 26.5, 20.7, 15.6, and 16.9 kJ·mol^{-1}, respectively, revealing PEDOT:PSS as the best catalyst among the studied for the reduction of $Co(bpy)_3^{3+}$; GCB electrode displays only a slightly lower performance. Sputtered Pt_{Met} electrodes show decent catalytic activity towards $Co(bpy)_3^{3+}$ reduction, E_a = 20.7 kJ·mol^{-1}. Noteworthy, Pt_{NP} electrodes formed by thermal decomposition of H_2PtCl_6 are the least active catalysts. The highest E_a of Pt_{NP} is more likely due to the conventional thermal platinization, which typically leaves *ca.* 20 % of the platinum surface passivated as $PtCl_2$ and $PtCl_4$ [43].

3.3.2 Performance of M-DSSCs with Pt_{Met}, PEDOT:PSS and GCB counter-electrodes

Fig. 3.4 presents the photocurrent *vs.* applied potential (*J-V*) curves for M-DSSC assembled with counter-electrodes of Pt_{Met}, GCB, and PEDOT:PSS. As a spacer layer, conventional opaque ZrO_2 (6±1 μm) was used.

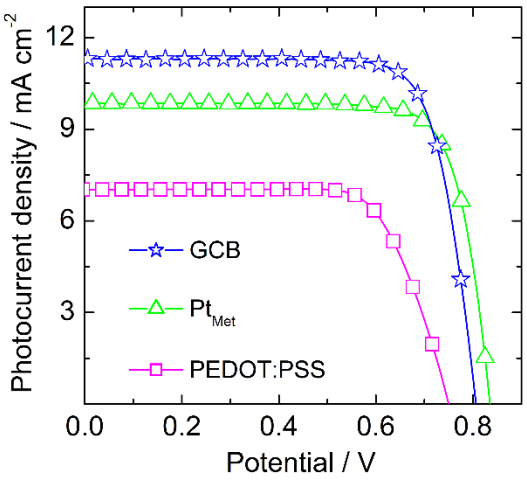

Fig. 3.4 *J-V* curves of M-DSSCs with different counter-electrodes.

The metrics of the photovoltaic performance were extracted from *J-V* curves and summarized in **Table 3.1**.

Table 3.1

Photovoltaic metrics of M-DSSCs and resistances (in $\Omega \cdot cm^2$) of the devices with different counter-electrodes.

CE	V_{OC} / V	J_{SC} / mA·cm^{-2}	FF	PCE / %	R_S	R_{CE}	R_K	R_{El}
Pt_{Met}	0.84	9.8	0.79	6.5	7.4	12.7	75.6	45.6
GCB	0.81	11.3	0.78	7.1	10.4	28.9	82.4	40.1
PEDOT:PSS	0.75	7.0	0.73	3.8	44.7	117.7	450.7	1288

M-DSSC with sputtered Pt_{Met} electrode displays a V_{OC} of 0.84 V, a J_{SC} of 9.8 mA·cm^{-2} and a FF of 0.79, resulting in a PCE of 6.5 %. The device with an electrode made by GCB displays the highest J_{SC} (J_{SC} = 11.3 mA·cm^{-2}) and PCE of 7.1 %. Surprisingly, despite the highest catalytic activity of PEDOT:PSS, M-DSSC with this electrode showed the weakest photocurrent and a PCE of only *ca*. 4 %. An EIS study was performed to identify the effect of the counter-electrodes on the device performance (**Fig. 3.5a**).

The equivalent electrical circuit presented in **Fig. 3.5b** fits well the EIS spectra [44-46]. The elements in the model represent series resistance (R_S), charge-transfer resistance at the electrolyte/counter-electrode interface (R_{CE}), recombination resistance at the photoanode/electrolyte interface (R_K), and the diffusion resistance in the electrolyte (R_{El}); CPE_{CE}, CPE_K, and CPE_{El} are the respective constant phase elements. Resistances of the equivalent circuit elements obtained fitting impedance response are summarized in **Table 3.1**.

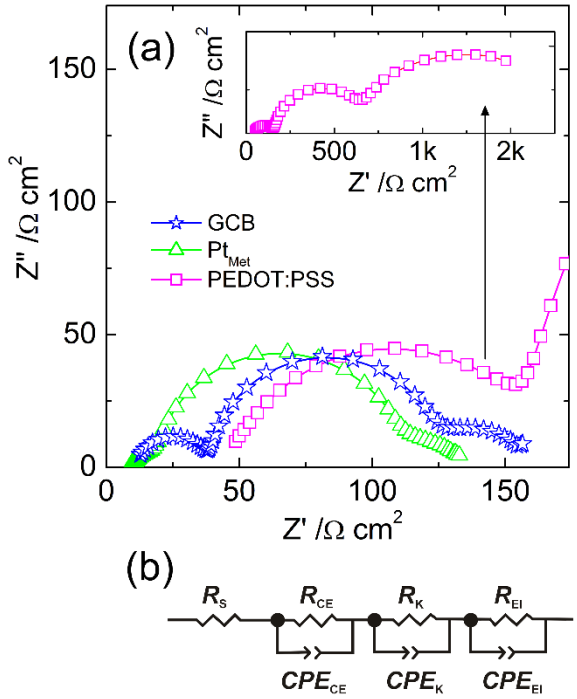

Fig. 3.5 EIS response in Nyquist plots of M-DSSCs with different counter-electrodes (***a***). Solid lines show fits to the equivalent circuit [44-46], presented in the chart (***b***).

In M-DSSC with counter-electrodes of PEDOT:PSS, all internal resistances of the device are incredibly high, bringing low overall performance. This was assigned to the way the PEDOT:PSS layer was applied. During the deposition of the PEDOT:PSS solution over the spacer-layer, the polymer penetrates it, clogging the pores. This hinders the charge transport in both counter-electrode/electrolyte and photoanode/electrolyte interfaces, preventing the diffusion of the electrolyte; high R_{CE}, R_K and R_{El} resistances support this interpretation of the observed low performance. PEDOT:PSS film prepared by spin-coating on the spacer layer had poor integrity, originating high R_S and low V_{OC}.

The devices assembled with Pt_{Met} and GCB electrodes show close values of R_S, R_K and R_{El}. Low R_S *ca.* 10 Ω·cm^2 points that conductivity of 15 μm GCB layer is comparable with that of solid 100 nm Pt layer obtained by sputtering. Practically identical for both devices, R_K is *ca.* 80 Ω·cm^2 and R_{El} is *ca.* 40-45 Ω·cm^2, indicating that photoanode/electrolyte interface and diffusion of the electrolyte through the spacer-layer are not affected by the counter-electrode. The R_{CE} on the GCB of *ca.* 30 Ω·cm^2 is higher than the R_{CE} of 13 Ω·cm^2 on Pt_{Met} electrode. This is opposite to the R_{CE} values obtained for the dummy cells, *ca.* 0.2 and 9 Ω·cm^2 for GCB and Pt_{Met}, respectively (**Table B1**). This happens because in the dummy cells the surface of the electrode is exposed to the electrolyte, while in the M-DSSC device, the counter-electrode is monolithically attached to the porous spacer. Higher

R_{CE} causes loss of potential, specifically at low current densities; as a result, the V_{OC} of the device with GCB electrode is slightly lower than V_{OC} of the M-DSSCs with Pt_{Met} (**Fig. 3.4**). Nevertheless, the developed surface of the GCB counter-electrode ensures a high rate for the diffusion-limited process; higher saturation photocurrent is achieved (**Fig. 3.4**), rendering a device with a PCE of 7.1 %. Further improvements were achieved optimizing the electrical spacer layer, the photoanode sensitization time, and the concentration of the recombination-suppressing additive.

3.3.3 Spacer layer in M-DSSCs

PCE of M-DSSCs is significantly affected by the electrical spacer layer [23,24,47]. The spacer layer must be insulating to prevent electron flow between photoanode and counter-electrode; must be porous to ensure a good flow of ions between electrodes, and must be light reflective to direct unabsorbed light back to the photoelectrode for more efficient light harvesting.

Fig. 3.6a presents the *J-V* response of the devices with commercial ZrO_2 and TiO_2 spacer layers and GCB counter electrode. A spacer made from porous titania improved the J_{SC} up to *ca*. 13.9 $mA \cdot cm^{-2}$, while the M-DSSCs with ZrO_2 layer display J_{SC} of 11.9 $mA \cdot cm^{-2}$.

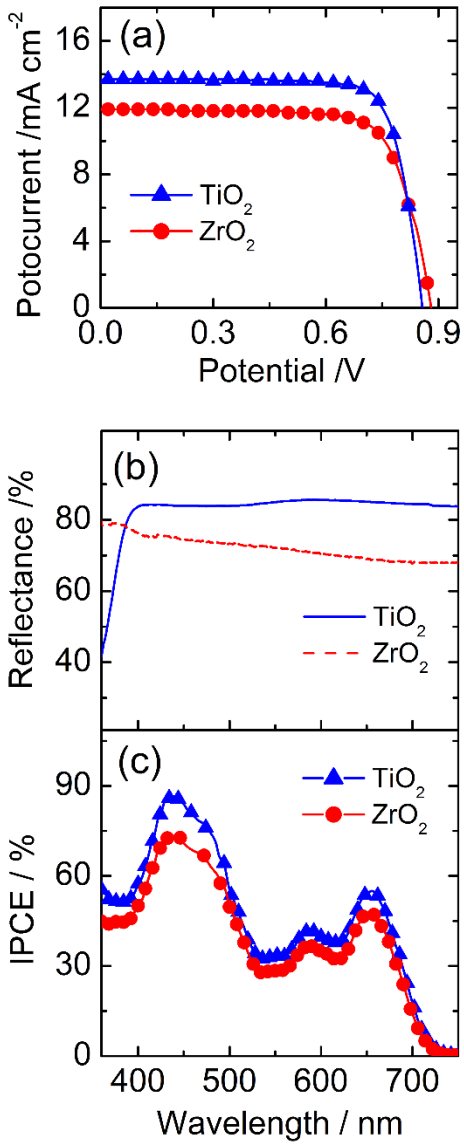

Fig. 3.6 *J-V* curves **(*a*)**, the reflectance of the TiO_2 and ZrO_2 electrical spacer layers **(*b*)** and IPCE spectra of M-DSSCs with different spacer layers (***c***).

Considering that titania and zirconia spacers have an identical thickness of *ca*. 6 μm, practically the same morphology and porosity (**Fig. C1**), the improvement of the photocurrent with the TiO_2 spacer was assigned to its higher reflectivity when compared with ZrO_2 (**Fig. 3.6b**). Titania spacer contains scattering particles of rutile, which has one of the highest refractive indexes of *ca.* 2.8 [48,49], contributing to better light scattering and reflection. The reflectivity of the titania spacer is superior to that of zirconia at wavelengths above 400 nm; following, more unabsorbed light is reflected to the photoanode, leading to the uniform increase of the IPCE response in the spectral range 400-750 nm (**Fig. 3.6c**) which renders M-DSSCs routinely displaying PCE of 9.0 % and a champion device with a PCE of 9.5%.

In the last couple of years, DSSCs has been established as one of the most promising PV devices for indoor applications [7-10]. Being a recent trend, none standard indoor-light source was yet recognized. We recorded the *J-V* curves of M-DSSC devices under indoor light using a LED lamp with an intensity of 600 lx (175 μW·cm^{-2}) and 1000 lx (286 μW·cm^{-2}) (**Fig. 3.7**). The PCE was determined considering the ratio of the maximum power delivered by the device to the incident light power of the LED lamp.

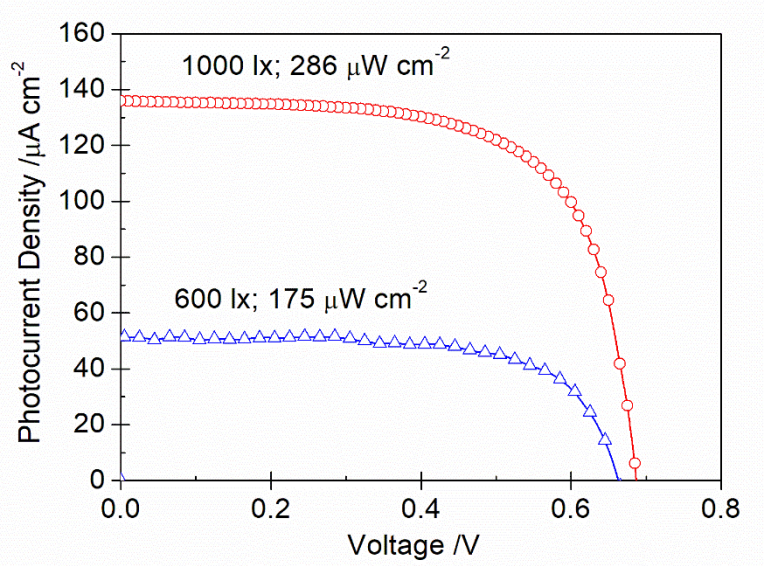

Fig. 3.7. *J-V* curves of the M-DSSC device under artificial light with different light intensities.

M-DSSCs with an average 1-sun PCE of 9.0 % – champion cell displayed 9.5 % of PCE – displayed the maximum output power of 22.8 μW·cm^{-2} and 62.7 μW·cm^{-2}, and PCE of 13.0 % and 21.9 % under 600 lx and 1000 lx, respectively. It is noteworthy that the artificial light PCEs derived from the M-DSSCs have achieved and even slightly surpassed the PCEs of the recently reported counterparts, assembled in a priori more efficient conventional configuration [50,51], with the use, however, expensive Pt metal film as a counter-electrode.

3.3.4 Sensitization of photoanode in M-DSSC

The sensitization conditions must ensure good dye loading at the photoanode for effective light absorption and efficient photocurrent generation [52,53]. Excessive dye adsorption leads to the agglomeration of the dye molecules, which causes quenching of the excited states and decreases electron injection into TiO_2. Dye agglomerates clog the mesopores in the photoanode, preventing electrolyte diffusion, dye regeneration, and charge transfer at the photoanode. It is possible to effectively mitigate the excessive dye adsorption controlling the sensitization time [52]. For the conventionally assembled device, the optimum time for TiO_2 sensitization using YD2-*o*-C8 dye

solution was determined as 12-16 h [28], when the mesoporous TiO_2 layer is directly exposed to sensitizing solution. In M-DSSCs, dye delivery to the TiO_2 occurs through the porous spacer and counter-electrode layers. The sensitization time has then to be optimized for the monolithic architecture [47], a crucial parameter often neglected by researchers. **Fig. 3.8** shows the normalized metrics (PCE, J_{SC}, $V_{OC,}$ and FF) of M-DSSC *vs*. time of sensitization in YD2-*o*-C8 solution.

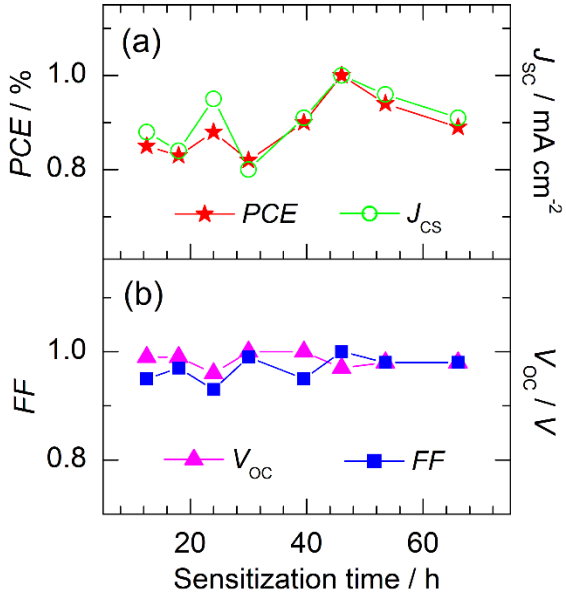

Fig. 3.8 Normalized PCE and J_{SC} ***(a)***, V_{OC} and FF ***(b)*** of M-DSSCs *vs.* sensitization time.

After 16 h of sensitization, M-DSSCs display rather low photocurrent and the FF values, indicate insufficient dye loading. The tested M-DSSCs show the highest PCE after *ca.* 46 ± 2 h of sensitization, which is mainly related to the current density (**Fig. 3.8a**); however, a small drop in V_{OC} and FF is also observed (**Fig. 3.8b**). After 48 h of sensitization, J_{SC} starts to drop (**Fig. 3.8a**), which should be related to the dye aggregation onset.

3.3.5 Concentration of the recombination-suppressing additive in the electrolyte

In cobalt electrolyte, 4-*tert*-butylpyridine (TBP) is used to suppress back electron recombination, increase the concentration of electrons on the conduction band of TiO_2, and to attain high V_{OC} and decent photocurrents [28,54-57]. An increase in TBP concentration raises the amount of TBP adsorbed on the TiO_2 surface, increasing the recombination resistance at TiO_2/electrolyte interface, improving the V_{OC} up to ~1 V [54]. Koh *et al.* [55] reported that excessive TBP concentration decelerates the diffusion of Co species and reduces the photocurrent. The optimum concentration of TBP in conventional DSSCs was determined as to be *ca*. 0.8 M [28]. Our study suggests that this could not be straightforwardly translated to M-DSSCs, and adjusting of TBP concentration is crucial for achieving high PCE.

Table 3.2 presents normalized photovoltaic parameters of M-DSSCs loaded with electrolytes containing different concentrations of TBP from 0.8 to 1.4 M.

Table 3.2

Normalized photovoltaic metrics of M-DSSCs for different TBP concentrations in the electrolyte; the resistances (in $\Omega \cdot cm^2$) were obtained by fitting the model (**Fig. 3.5b**) to the Nyquist plots (**Fig. 3.9**) of the corresponding devices.

[TBP] /M	V_{OC} / V	J_{SC} / mA·cm^{-2}	FF	PCE / %	R_S	R_{CE}	R_K	R_{El}
0.8	0.96	0.90	1.00	0.88	6.2	53.9	46.2	25.6
1.0	0.92	0.86	0.99	0.81	6.5	59.5	53.7	23.5
1.2	1.00	1.00	0.97	1.00	6.9	111.2	77.0	48.5
1.4	1.00	0.88	0.99	0.90	6.7	123.0	115.5	40.6

The highest PCE was observed at TBP concentration of 1.2 M. EIS study of the M-DSSCs was performed to identify the effect of TBP concentration on the M-DSSCs performance (**Fig. 3.9**).

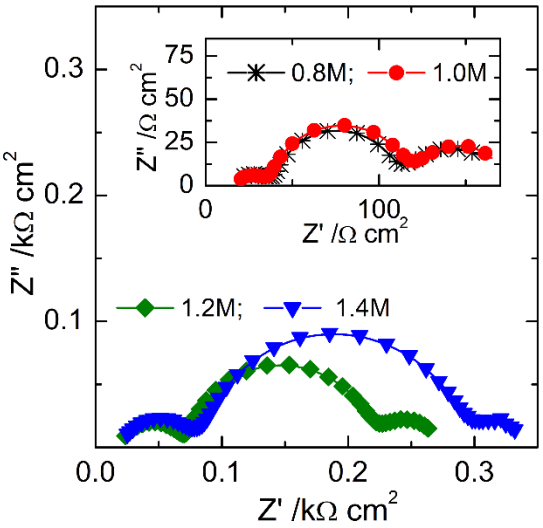

Fig. 3.9 Nyquist diagrams for EIS response of the M-DSSCs with different TBP concentration in the electrolyte.

Nyquist plots show typical patterns with 3 capacitive semicircles, which are associated with the interfacial charge transfer and diffusion in the electrolyte, as described in section 3.3.2 (**Fig. 3.5**). The assigned values to the corresponding resistances are summarized in **Table 3.2**. The series resistance of the devices (R_S) is not affected by TBP. Interfacial resistances R_{CE}, $R_{K,}$ and resistance R_{El} gradually increase with TBP concentration. Higher interfacial resistances are due to the TBP adsorption on the photoanode [56] and counter-electrode [57,58], and higher transport resistance in the electrolyte (R_{El}) originates from the increased viscosity of the electrolyte [55]. It is noteworthy that with an increase

of TBP concentration from 0.8 to 1.0 M, the resistances R_{CE}, R_K, and R_{El} increase slightly but at TBP concentration of 1.2 M they rise a lot, rendering the cells with the highest photovoltaic parameters. In comparison with conventional counterparts, monolithic cells require a higher optimum concentration of TBP. It might be because of the TiO_2 spacer layer with developed surface and thick porous GCB counter-electrode; TiO_2 effectively adsorbs TBP [56], significantly reducing the available concentration for the electrolyte, carbon counter-electrode may contribute as well in the TBP adsorption from the electrolyte [58].

3.3.6 Stability of cobalt-mediated M-DSSC

The history of the PCE in the devices was followed during 1000 h under natural aging (**Fig. 3.10**). Within the first 24 h the PCE slightly increases, which is typical behavior of DSSCs [59].

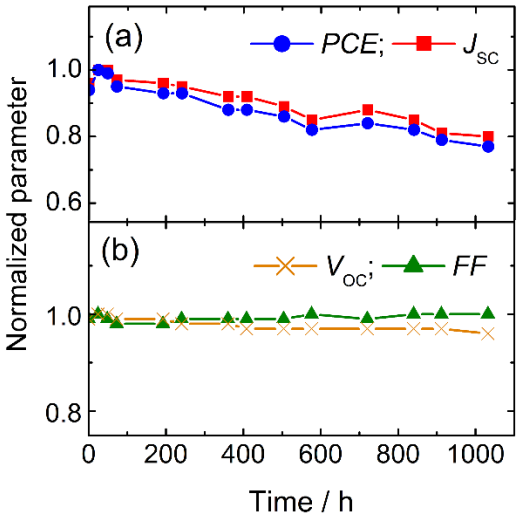

Fig. 3.10 History of the PCE and J_{SC} (***a***), V_{OC} and FF (***b***) for cobalt-mediated M-DSSC.

During aging, the PCE was mostly affected by the drop of photocurrent (**Fig. 3.10a**), which is most likely due to the acetonitrile leakage through polymeric sealants [60]. The V_{OC} remained practically constant, while the FF suffered a slight decrease up to 600 h of aging (**Fig. 3.10b**). The PCE deterioration factor determined from the declination of the plot is relatively high, *ca.* $1.6 \cdot 10^{-4}$ per day. The stability of the devices by preventing electrolyte leakage should be addressed in future studies, using recently developed by the authors highly hermetic laser-assisted encapsulation with glass materials [61,62], alternatively, implementing quasi-solid state electrolytes [50,51].

3.4 Conclusions

The challenge of preparing highly efficient liquid-junction cobalt-mediated monolithic DSSCs, using commercially available materials, was addressed. The electrochemical activity of conventional counter-electrodes, light-reflecting properties of the electrical spacer layers, optimizing the photoanode sensitization, and fine-tuning the concentration of back electron recombination suppressing additive in the electrolyte were studied and optimized. Conventional counter-electrodes made from Pt nanoparticles, Pt metal film, graphite/carbon-black composite and PEDOT:PSS display apparent activation energy of 26.5, 20.7, 16.9 and 15.6 $kJ \cdot mol^{-1}$, respectively, in the reduction of $Co(bpy)_3^{3+}$. Extremally low saturation current densities were obtained when using the Pt nanoparticles electrode, making it an inappropriate choice for preparing efficient device. The Pt and graphite/carbon-black counter-electrode layers allowed reaching decent photocurrents and PCE of *ca.* 6.5 and 7 %, respectively. Unexpectedly low PCE of *ca.* 4 % was obtained with PEDOT:PSS electrode due to the its infiltration on the spacer-layer, which clogs the pores, hindering the charge transport and electrolyte diffusion. Highly reflecting electrical spacer layer made from rutile TiO_2, counter-electrode of graphite/carbon-black, optimized photoanode sensitization conditions and of the recombination suppressing additive concentration (4-*tert*-butylpyridine) rendered M-DSSC with a record break PCE of 9.5 % under 1-sun illumination, and a decent PCE of 21.9 % under 1000 lx artificial light.

Acknowledgments

The authors acknowledge the financial support from the “SunStorage” project, POCI-01-0145-FEDER-016387, funded by European Regional Development Fund (ERDF) through COMPETE2020; the projects POCI-01-0145-FEDER-006939, NORTE-01-0145-FEDER-000005 and LEPABE-2-ECO-INNOVATION, all funded by FEDER funds through COMPETE 2020, and the Materials Centre of the University of Porto. This work was also financially supported by the UIDB/00511/2020 Energy – LEPABE - funded by national funds through the FCT/MCTES (PIDDAC); F. Santos and C.S. Hora acknowledge the FCT for their PhD grants reference SFRH/BD/132388/2017 and SFRH/BD/129761/2017, respectively.

References

[1] K. Sharma, V. Sharma, S.S. Sharma, Dye-Sensitized Solar Cells: Fundamentals and Current Status, *Nanoscale Res. Lett*., 2018, 13, 381. DOI: 10.1186/s11671-018-2760-6.

[2] N. Mariotti, M. Bonomo, L. Fagiolari, N. Barbero, C. Gerbaldi, F. Bella, C. Barolo, Recent Advances in Eco-Friendly and Cost-Effective Materials towards Sustainable Dye-Sensitized Solar Cells, *Green Chem.*, **2020**, 22, 7168-7218. DOI: 10.1039/D0GC01148G.

[3] T. Toyoda, T. Sano, J. Nakajima, S. Doi, S. Fukumoto, A. Ito, T. Tohyama, M. Yoshida, T. Kanagawa, T. Motohiro, T. Shiga, K. Higuchi, H. Tanaka, Y. Takeda, T. Fukano, N. Katoh, A. Takeichi, K. Takechi, M. Shiozawa, Outdoor performance of large scale DSC modules, *J. Photochem. Photobiol. A Chem*., 2004, 164, 203–207. DOI: 10.1016/j.jphotochem.2003.11.022.

[4] C. Cornaro, S. Bartocci, D. Musella, C. Strati, A. Lanuti, S. Mastroianni, S. Penna, A. Guidobaldi, F. Giordano, E. Petrolati, T.M. Brown, A. Reale, A.D. Carlo, Comparative analysis of the outdoor performance of a dye solar cell mini-panel for building integrated photovoltaics applications, *Prog. Photovolt: Res. Appl.*, 2015, 23, 215–225. DOI: 10.1002/pip.2426.

[5] J.-H. Kim, S.-H. Han, Energy Generation Performance of Window-Type Dye-Sensitized Solar Cells by Color and Transmittance, *Sustain*., 2020, 12(21), 8961. DOI: 10.3390/su12218961.

[6] G. Acciari, G. Adamo, G. Ala, A. Busacca, M. Caruso, G. Giglia, A. Imburgia, P. Livreri, R. Miceli, A. Parisi, F. Pellitteri, R. Pernice, P. Romano, G. Schettino, F. Viola, Experimental Investigation on the Performances of Innovative PV Vertical Structures, *Photonics*, 2019, 6(3), 86. DOI: 10.3390/photonics6030086.

[7] I. Mathews, S.N. Kantareddy, T. Buonassisi, I.M. Peters, Technology and Market Perspective for Indoor Photovoltaic Cells, *Joule*, 2019, 3, 1415–1426. DOI: 10.1016/j.joule.2019.03.026.

[8] M. Freitag, J. Teuscher, Y. Saygili, X. Zhang, F. Giordano, P. Liska, J. Hua, S.M. Zakeeruddin, J.E. Moser, M. Grätzel, A. Hagfeldt, Dye-Sensitized Solar Cells for Efficient Power Generation under Ambient Lighting, *Nat. Photonics*, 2017, 11, 372–378. DOI: 10.1038/nphoton.2017.60.

[9] Y. Cao, Y. Liu, M. Zakeeruddin, A. Hagfeldt, Y. Cao, Y. Liu, S.M. Zakeeruddin, A. Hagfeldt, M. Gra, Direct Contact of Selective Charge Extraction Layers Enables High-Efficiency Molecular Photovoltaics, *Joule*, 2018, 2, 1108–1117. DOI: 10.1016/j.joule.2018.03.017.

[10] H. Michaels, M. Rinderle, R. Freitag, I. Benesperi, T. Edvinsson, R. Socher, A. Gagliardi, M. Freitag, Dye-sensitized solar cells under ambient light powering machine learning: Towards autonomous smart sensors for the internet of things. *Chem. Sci.*, 2020, 11, 2895–2906. DOI: 10.1039/C9SC06145B.

[11] A. Fakharuddin, R. Jose, T.M. Brown, F. Fabregat-Santiago, J. Bisquert, A perspective on the production of dye-sensitized solar modules, *Energy Environ. Sci.*, 2014, 7, 3952–3981. DOI: 10.1039/C4EE01724B.

[12] B. O'Regan, M. Grätzel, A Low-Cost, High-Efficiency Solar Cell Based on Dye-Sensitized Colloidal TiO_2 Films, *Nat*., 1991, 353, 737-740. DOI: 10.1038/353737a0.

[13] M. Green, E. Dunlop, J. Hohl-Ebinger, M. Yoshita, N. Kopidakis, X. Hao, Solar Cell Efficiency Tables (Version 57), *Prog. Photovolt. Res. Appl*., 2020, 29, 3-15. DOI: 10.1002/pip.3371.

[14] L. Han, A. Islam, H. Chen, C. Malapaka, B. Chiranjeevi, S. Zhang, X. Yang, M. Yanagida, High-Efficiency Dye-Sensitized Solar Cell with a Novel Co-Adsorbent, *Energy Environ. Sci*., 2012, 5, 6057–6060. DOI: 10.1039/C2EE03418B.

[15] B.E. Hardin, H.J. Snaith, M.D. McGehee, The Renaissance of Dye-Sensitized Solar Cells, *Nat. Photonics*, 2012, 6, 162–169. DOI: 10.1038/nphoton.2012.22.

[16] K. Zeng, Z. Tong, L. Ma, W.H. Zhu, W. Wu, Y. Xie, Y. Xie, Molecular Engineering Strategies for Fabricating Efficient Porphyrin-Based Dye-Sensitized Solar Cells, *Energy Environ. Sci.*, 2020, 13, 1617–1657. DOI: 10.1039/C9EE04200H.

[17] S. Mathew, A. Yella, P. Gao, R. Humphry-Baker, B.F.E. Curchod, N. Ashari-Astani, I. Tavernelli, U. Rothlisberger, M.K. Nazeeruddin, M. Grätzel, Dye-Sensitized Solar Cells with 13% Efficiency Achieved through the Molecular Engineering of Porphyrin Sensitizers, *Nat. Chem*., 2014, 6, 242–247. DOI: 10.1038/nchem.1861.

[18] J.M. Ji, H. Zhou, Y.K. Eom, C.H. Kim, H.K. Kim, 14.2% Efficiency Dye-Sensitized Solar Cells by Co-Sensitizing Novel Thieno[3,2-b]Indole-Based Organic Dyes with a Promising Porphyrin Sensitizer, *Adv. Energy Mater*., 2020, 10, 1–12. DOI: 10.1002/aenm.202000124.

[19] S. Hattori, Y. Wada, S. Yanagida, S. Fukuzumi, Blue Copper Model Complexes with Distorted Tetragonal Geometry Acting as Effective Electron-Transfer Mediators in Dye-Sensitized Solar Cells, *J. Am. Chem. Soc*., 2005, 127, 9648–9654. DOI: 10.1021/ja0506814.

[20] J.M. Kroon, Energy Research Center report, ECN-C-05-078, 2005, 1–41.

[21] G. Liu, H. Wang, X. Li, Y. Rong, Z. Ku, M. Xu, L. Liu, M. Hu, Y. Yang, P. Xiang, T. Shu, H. Han, A mesoscopic platinized graphite/carbon black counter electrode for a highly efficient monolithic dye-sensitized solar cell, *Electrochim. Acta***,** 2012, 69, 334–339. DOI: 10.1016/j.electacta.2012.03.012.

[22] J. Kwon, N.G. Park, J.Y. Lee, M.J. Ko, J.H. Park, Highly efficient monolithic dye-sensitized solar cells, *ACS Appl. Mater. Interfaces*, 2013, 5, 2070–2074. DOI: 10.1021/am302974z.

[23] F. Behrouznejad, N. Taghavinia, N. Ghazyani, Monolithic dye sensitized solar cell with metal foil counter electrode, *Org. Electron*., 2018, 57, 194–200. DOI: 10.1016/j.orgel.2018.03.009.

[24] S.J. Thompson, N.W. Duffy, U. Bach, Y.B. Cheng, On the role of the spacer layer in monolithic dye-sensitized solar cells, *J. Phys. Chem. C*., 2010, 114, 2365–2369. DOI: 10.1021/jp907967h.

[25] A. Kay, M. Grätzel, Low cost photovoltaic modules based on dye sensitized nanocrystalline titanium dioxide and carbon powder, *Sol. Energy Mater. Sol. Cells*, 1996, 44, 99–117. DOI: 10.1016/0927-0248(96)00063-3.

[26] L. Vesce, R. Riccitelli, G. Mincuzzi, A. Orabona, G. Soscia, T.M. Brown, A. Di Carlo, A. Reale, Fabrication of spacer and catalytic layers in monolithic dye-sensitized solar cells, *IEEE J. Photovolt.*, 2013, 3, 1004–1011. DOI: 10.1109/JPHOTOV.2013.2262374.

[27] J. Maçaira, I. Mesquita, L. Andrade, A. Mendes, Role of Temperature in the Recombination Reaction on Dye-Sensitized Solar Cells, *Phys. Chem. Chem. Phys.*, 2015, 17, 22699–22710. DOI: 10.1039/C5CP02942B.

[28] A. Yella, H.-W. Lee, H.N. Tsao, C. Yi, A.K. Chandiran, M.K. Nazeeruddin, E.W.-G. Diau, C.-Y. Yeh, S.M. Zakeeruddin, M. Grätzel, Porphyrin-Sensitized Solar Cells with Cobalt (II/III)–Based Redox Electrolyte Exceed 12 Percent Efficiency, *Sci.*, 2011, 334, 629–634. DOI: 10.1126/science.1209688.

[29] H.N. Tsao, P. Comte, C. Yi, M. Grätzel, Avoiding Diffusion Limitations in Cobalt(III/II)-Tris(2,2′- Bipyridine)-Based Dye-Sensitized Solar Cells by Tuning the Mesoporous TiO2 Film Properties, *ChemPhysChem*, 2012, 13, 2976–2981. DOI: 10.1002/cphc.201200435.

[30] L. Kavan, J.H. Yum, M. Grätzel, Graphene nanoplatelets outperforming platinum as the electrocatalyst in co-bipyridine-mediated dye-sensitized solar cells, *Nano Lett.*, 2011, 11, 5501–5506. DOI: 10.1021/nl203329c.

[31] C.K. Kim, H.M. Kim, M. Aftabuzzaman, I.-Y. Jeon, S.H. Kang, Y.K. Eom, J.B. Baek, H.K. Kim, Comparative study of edge-functionalized graphene nanoplatelets as metal-free counter electrodes for highly efficient dye-sensitized solar cells, *Mater. Today Energy*, 2018, 9, 67–73. DOI: 10.1016/j.mtener.2018.05.003.

[32] I.-Y. Jeon, H.M. Kim, D.H. Kweon, S.-M. Jung, J.-M. Seo, S.-H. Shin, I.T. Choi, Y.K. Eom, S.H. Kang, H.K. Kim, M.J. Ju, J.-B. Baek, Metalloid tellurium-doped graphene nanoplatelets as ultimately stable electrocatalysts for cobalt reduction reaction in dye-sensitized solar cells, *Nano Energy*, 2016, 30, 867–876. DOI: 10.1016/j.nanoen.2016.09.001.

[33] H.N. Tsao, J. Burschka, C. Yi, F. Kessler, M.K. Nazeeruddin, M. Grätzel, Influence of the interfacial charge-transfer resistance at the counter electrode in dye-sensitized solar cells employing cobalt redox shuttles, *Energy Environ. Sci.*, 2011, 4, 4921–4924. DOI: 10.1039/C1EE02389F.

[34] J.C. Kim, M.M. Rahman, M.J. Ju, J.J. Lee, Highly conductive and stable graphene/PEDOT:PSS composite as a metal free cathode for organic dye-sensitized solar cells, *RSC Adv.*, 2018, 8, 19058–19066. DOI: 10.1039/C8RA02668H.

[35] S. Ahmad, T. Bessho, F. Kessler, E. Baranoff, J. Frey, C. Yi, M. Grätzel, M.K. Nazeeruddin, A new generation of platinum and iodine free efficient dye-sensitized solar cells, *Phys. Chem. Chem. Phys.*, 2012, 14, 10631–10639. DOI: 10.1039/C2CP41611E.

[36] H. Wang, Q. Feng, F. Gong, Y. Li, G. Zhou, Z.S. Wang, In situ growth of oriented polyaniline nanowires array for efficient cathode of Co(III)/Co(II) mediated dye-sensitized solar cell, *J. Mater. Chem. A*, 2013, 1, 97–104. DOI: 10.1039/C2TA00705C.

[37] I. Liu, Y. Hou, C. Li, Y. Lee, Highly Electrocatalytic Counter Electrodes Based on Carbon Black for Cobalt(III)/(II)-Mediated Dye-Sensitized Solar Cells, *J. Mater. Chem. A*, 2017, 5, 240–249. DOI: 10.1039/C6TA08818J.

[38] M. Stefik, J.H. Yum, Y. Hu, M. Grätzel, Carbon-graphene nanocomposite cathodes for improved Co(ii/iii) mediated dye-sensitized solar cells, *J. Mater. Chem. A*, 2013, 1, 4982–4987. DOI: 10.1039/C3TA01635H.

[39] A. Petrocco, M. Liberatore, A. Di Carlo, A. Reale, T.M. Brown, F. Decker, Thermal Activation of Mass Transport and Charge Transfer at Pt in the I3−/I− Electrolyte of a Dye-Sensitized Solar Cell, *Phys. Chem. Chem. Phys*, 2010, 12, 10786–10792. DOI: 10.1039/C002840A.

[40] G. Yue, J. Wu, Y. Xiao, M. Huang, J. Lin, J.Y. Lin, High Performance Platinum-Free Counter Electrode of Molybdenum Sulfide-Carbon Used in Dye-Sensitized Solar Cells, *J. Mater. Chem. A*, 2013, 1, 1495–1501. DOI: 10.1039/C2TA00860B.

[41] J. Burschka, V. Brault, S. Ahmad, L. Breau, M.K. Nazeeruddin, B. Marsan, S.M. Zakeeruddin, M. Grätzel, Influence of the Counter Electrode on the Photovoltaic Performance of Dye-Sensitized Solar Cells Using a Disulfide/Thiolate Redox Electrolyte, *Energy Environ. Sci*., 2012, 5, 6089–6097. DOI: 10.1039/C2EE03005E.

[42] A. Lasia, Impedance of Porous Electrodes, *J. Electroanal. Chem*. 1995, 397, 27-33. DOI: 10.1016/0022-0728(95)04177-5.

[43] G. Khelashvili, S. Behrens, C. Weidenthaler, C. Vetter, A. Hinsch, R. Kern, K. Skupien, E. Dinjus, H. Bo, Catalytic Platinum Layers for Dye Solar Cells: A Comparative Study, *Thin Solid Films*, 2006, 512, 342–348. DOI: 10.1016/j.tsf.2005.12.059.

[44] W.S. Arsyad, R. Hidayat, Photovoltaic and Impedance Characteristics of Quasi Solid-State Dye-Sensitized Solar Cell Using Polymer Gel Electrolytes, *Adv. Mater. Res.*, 2015, 1112, 256–261. DOI: 10.4028/www.scientific.net/AMR.1112.256.

[45] G. Zhu, L. Pan, J. Yang, X. Liu, H. Sun, Z. Sun, Electrospun nest-shaped TiO2 structures as a scattering layer for dye sensitized solar cells, *J. Mater. Chem.*, 2012, 22, 24326-24329. DOI: 10.1039/C2JM33219A.

[46] S. Suresh, G.E. Unni, C. Ni, R.S. Sreedharan, R.R. Krishnan, M. Satyanarayana, M. Shanmugam, V.P.M. Pillai, Phase Modification and Morphological Evolution in Nb2O5 Thin Films and Its Influence in Dye-Sensitized Solar Cells, *Appl. Surf. Sci.*, 2017, 419, 720–732. DOI: 10.1016/j.apsusc.2017.05.081.

[47] F. Santos, C. Hora, G. Bernardo, D. Ivanou, A. Mendes, Efficient Monolithic Dye Sensitized Solar Cells with Eco-Friendly Silica-Titania Spacer Layers, *Sol. Energy*, 2019, 183, 419–424. DOI: 10.1016/j.solener.2019.03.056.

[48] J. Rams, A. Tejeda, J.M. Cabrera, Refractive Indices of Rutile as a Function of Temperature and Wavelength, *J. Appl. Phys.*, 1997, 82, 994-997. DOI: 10.1063/1.365938.K.

[49] Möls, L. Aarik, H. Mändar, A. Kasikov, A. Niilisk, R. Rammula, J. Aarik, Influence of Phase Composition on Optical Properties of TiO2: Dependence of Refractive Index and Band Gap on Formation of TiO2-II Phase in Thin Films, *Opt. Mater. (Amst),* **2**019, 96, 109335. DOI: 10.1016/j.optmat.2019.109335.

[50] S. Venkatesan, I.P. Liu, W.N. Hung, H. Teng, Y.L. Lee, Highly Efficient Quasi-Solid-State Dye-Sensitized Solar Cells Prepared by Printable Electrolytes for Room Light Applications, *Chem. Eng. J.*, 2019, 367(1), 17–24. DOI: 10.1016/j.cej.2019.02.118.

[51] S. Venkatesan, I-P. Liu, C.-M. Tseng Shan, H. Teng, Y.-L. Lee, Highly Efficient Indoor Light Quasi-Solid-State Dye Sensitized Solar Cells Using Cobalt Polyethylene Oxide-Based Printable Electrolytes, *Chem. Eng. J.*, 2020, 394, 124954. DOI: 10.1016/j.cej.2020.124954.

[52] T. Higashino, H. Imahori, Porphyrins as excellent dyes for dye-sensitized solar cells: recent developments and insights, *Dalton Trans*., 2015, 44, 448-463. DOI: 10.1039/C4DT02756F.

[53] K. Zeng, Y. Lu, W. Tang, S. Zhao, Q. Liu, W. Zhu, H. Tian, Y. Xie, Efficient Solar Cells Sensitized by a Promising New Type of Porphyrin: Dye-Aggregation Suppressed by Double Strapping, *Chem. Sci.*, 2019, 41, 2186–2192. DOI: 10.1039/C8SC04969F.

[54] F. Bella, S. Galliano, C. Gerbaldi, G. Viscardi, Cobalt-Based Electrolytes for Dye-Sensitized Solar Cells: Recent Advances towards Stable Devices, *Energies,* 2016, 9, 384. DOI: 10.3390/en9050384.

[55] T.M. Koh, K. Nonomura, N. Mathews, A. Hagfeldt, M. Grätzel, S.G. Mhaisalkar, A.C. Grimsdale, Influence of 4-tert-Butylpyridine in DSCs with CoII/III Redox Mediator, *J. Phys. Chem. C,* 2013, 117, 15515−15522. DOI: 10.1021/jp403918q.

[56] T.A.P. Phan, N.P. Nguyen, L.T. Nguyen, P.H. Nguyen, T.K. Le, T. Van Huynh, T. Lund, D.H. Tsai, T.C. Wei, P.T. Nguyen, Direct Experimental Evidence for the Adsorption of 4-Tert-

Butylpyridine and 2,2'-Bipyridine on TiO2 Surface and Their Influence on Dye-Sensitized Solar Cells'Performance, *Appl. Surf. Sci*., 2020, 509, 144878. DOI: 10.1016/j.apsusc.2019.144878.

[57] J. Kim, J.Y. Kim, D. Lee, B. Kim, H. Kim, M.J. Ko, Importance of 4-Tert -Butylpyridine in Electrolyte for Dye-Sensitized Solar Cells Employing SnO2 Electrode, *J. Phys. Chem. C*, 2012, 116, 22759-22766. DOI: 10.1021/jp307783q.

[58] J. Lin, C. Lien, S. Chou, Multi-Wall Carbon Nanotube Counter Electrodes for Dye-Sensitized Solar Cells Prepared by Electrophoretic Deposition, *J. Solid State Electrochem.*, 2012, 16, 1415–1421. DOI: 10.1007/s10008-011-1541-2.

[59] F. Li, J.R. Jennings, N. Mathews, Q. Wang, Evolution of Charge Collection⁄Separation Efficiencies in Dye-Sensitized Solar Cells Upon Aging: A Case Study, *J. Electrochem. Soc.*, 2011, 158, B1158-B1163. DOI: 10.1149/1.3610366.

[60] W. Xiang, W. Huang, U. Bach, L. Spiccia, Stable High Efficiency Dye-Sensitized Solar Cells Based on a Cobalt Polymer Gel Electrolyte, *Chem. Commun.*, 2013, 49, 8997–8999. DOI: 10.1039/C3CC44555K.

[61] D.K. Ivanou, R. Santos, J. Maçaira, L. Andrade, A. Mendes, Laser assisted glass frit sealing for production large area DSCs panels, *Sol. Energy*, 2016, 135, 674–681. DOI: 10.1016/j.solener.2016.06.043.

[62] S. Emami, J. Martins, D. Ivanou, A. Mendes, Advanced Hermetic Encapsulation of Perovskite Solar Cells: The Route to Commercialization, *J. Mater. Chem. A,* 2020, 8, 2654-2662. DOI: 10.1039/C9TA11907H.

CHAPTER 4

STABLE COBALT-MEDIATED MONOLITHIC DYE-SENSITIZED SOLAR CELLS BY CELL FULL GLASS ENCAPSULATION

Under peer-revision in *ACS Applied Energy Materials* journal.

4

Stable cobalt-mediated monolithic dye-sensitized solar cells by cell full glass encapsulation

4.1 Introduction

Dye-sensitized solar cells (DSSCs) are the third generation photovoltaic (PV) devices [1] that recently reached a certified power conversion efficiency (PCE) of 13 % [2]. Since their inception in 1991 [3], DSSCs have attracted vast research interest due to their low manufacturing cost and sustainability [4,5], outstanding PCE under dim and artificial light [1,6], and aesthetics [1]. With the emergence of the Internet of Things (IoT) and indoor low-power consuming wireless communication devices, the development of energy sources for powering them emerged imperative [7,8]. DSSCs are among the most promising indoor PV technologies to address this challenge [9,10]: they display a record PCE of 34.5 % under indoor illumination [2], do not contain toxic lead or tin, can be produced in flexible substrates, and can be semitransparent with true colors for eye-pleasant interior integration [1,6]; DSSCs for indoor light conversion have recently entered the PV market [1,10].

The most efficient state-of-the-art DSSC devices use Co(III/II) or Cu(II/I) complexes as redox shuttles [2,6,11-13]. Copper-mediated devices hit certified 1-sun and artificial light conversion records [1,2], while cobalt DSSCs achieved a reported PCE above 14 % under AM1.5G light [12,13]. The best performing cobalt cells are liquid junctions with volatile acetonitrile (ACN) electrolyte [12-14]. Cobalt electrolytes are transparent compared to copper counterparts, which allow producing efficient bifacial devices [15,16] for gaining *ca.* 20-40 % of output power [17,18]; this is relevant for indoor use where the maximum power obtained from a single-face cell hardly reaches tenths of a milliwatt per cm^2 [8].

Since the advent of cobalt DSSCs, their stability has been questioned [19] and tremendous research efforts have been made for identifying the deterioration mechanisms [20-32]. Strategies for more stable devices include tuning the chemical structure of the cobalt complexes [20-22], adjusting concentration of Co(III) and Co(II) species [23,24], decreasing volatility of the solvents [25,26],

selecting proper electrolyte additives [20,23,26,27], identifying stable counter-electrodes [24,28], and developing of quasi-solid state gel-electrolyte devices [29-32]. The long-term stability of cobalt DSSCs loaded with ACN or with other less volatile electrolytes is always challenging due to the inevitable leakage of the solvent through the device's sealed perimeter [24-26,28]. Most of the time, the sealant used is a Surlyn thermoplastic that has poor barrier properties, low softening point temperature of *ca*. 93 ºC, and displays poor mechanical stability under temperature cycling tests [33]. To our knowledge, thermal cycling or damp heat tests, needed for final product certification, has never been reported for cobalt DSSCs with ACN electrolyte, even at a minimum setpoint temperature of 65 ºC, as recommended by ISOS protocols [34]. Electrolyte volatility also limits light-soaking tests for tracking PCE history; only a few studies consider testing periods for more than 1000 h [23,27]. Gao *et al.* [23,27] studied the effect of electrolyte composition and additives based on 1000 h aging tests under simulated solar light and 60 ºC. The authors reported that a higher concentration of Co(III/II) complexes favors the device's stability. 4-*tert*-butylpyridine (TBP)-free electrolytes allowed to fabricate a device with an initial PCE of 0.7 %, which improved over the testing period up to 3.5 %. A deterioration of *ca*. 15 % and 8 % in the initial PCE of *ca.* 6 % was observed with and without $LiClO_4$ additive, respectively; the low photostability in the presence of Li^+ ions was assigned to the fast dye degradation and electron lifetime decrease. Kamppinen *et al.* [24] studied the stability of poly(3,4-ethylenedioxythiophene) (PEDOT) and Pt counter-electrodes by exposing the devices to 1-sun light soaking for 2000 h at 40 ºC. Counter-electrodes made from Pt allowed a more stable device; however, the losses of PCE were 26 % and 53 % after 1000 h and 2000 h, respectively. Jiang *et al.* [25] observed *ca.* 34 % of PCE drop in the best ACN device after 2000 h of light soaking at open-circuit potential and 20 ºC, also reporting issues with electrolyte leakage.

Both intrinsic and extrinsic factors are affecting the stability of a PV cell [35]. The extrinsic factors are related to the encapsulation hermeticity. However, when the barrier properties of the encapsulant are unknown, it is impossible to clearly distinguish whether the intrinsic or extrinsic factors are responsible for the degradation of the device [35]. Surprisingly, the extrinsic stability of cobalt DSSCs has never been addressed, although practically all studies report electrolyte leaks.

Encouraged by the ability of cobalt-DSSCs to deliver high PCE under sunlight and artificial illumination [36], we report the most stable cobalt-DSSC device (M-DSSC), obtained by robust and exceptionally hermetic glass encapsulation. The device edges and the electrolyte injection holes were glass-sealed using a low-temperature laser-assisted process [37-39]. The seal tightness fully complies with MIL-STD-883 standard, helium leakage test, with no signs of deterioration after passing the humidity-freeze cycle test according to IEC 61646 standard. After eliminating the extrinsic factors of

degradation, we focused on the effect of the standard ISOS test conditions on the charge transfer at the interfaces of M-DSSCs, dye desorption, redistribution of the cobalt ions in the working device, and their impact on stability and overall PCE.

For the first time, glass-encapsulated M-DSSCs with ACN-based cobalt electrolyte and organic dye Y123 successfully passed several ISOS tests, including thermal cycling up to 85 ^{o}C, 1000 h of shelf-aging, 1000 h of solar and artificial light soaking with passive load, displaying the most steady history of photovoltaic metrics, and displaying an average PCE of 8 % under sunlight and 22 % under artificial illumination.

4.2 Experimental

4.2.1 Reagents and materials

Titanium diisopropoxide bis(acetylacetonate), acetylacetone, anhydrous isopropyl alcohol, 4-*tert*-butylpyridine (TBP), $LiClO_4$ (99.90 %) and acetonitrile (99.80 %) were purchased from Sigma-Aldrich®. Screen-printable TiO_2 pastes (30NR-D, WER2-O) and FTO-coated glasses (7 Ω/sq) were from GreatCell Solar®. Screen-printable glass paste to produce glass frit for the device sealing was based on Bi and Zn oxides. The thermoplastic sealant (Meltonix 1170-60, 60 µm Surlyn®) and the screen-printable graphite/carbon-black paste (Elcocarb B/SP) were acquired from Solaronix®. Complexes Co(III/II)tris(bipyridyl)tetracyanoborate (Eversolar Co-300 and Co-200) were from Everlight and Y123 organic sensitizer was ordered from Dyenamo. Titanium tetrachloride (99.90 %) and *t*-butanol (99.5 %) were purchased from Acros Organics.

4.2.2 Fabrication of fully hermetic M-DSSCs

Fully hermetic M-DSSCs were produced using laser-assisted glass-frit encapsulation of the cell edge [37-39] and the electrolyte injection holes were sealed with glass. **Fig. 4.1** illustrates the sequence of the device assembly procedures.

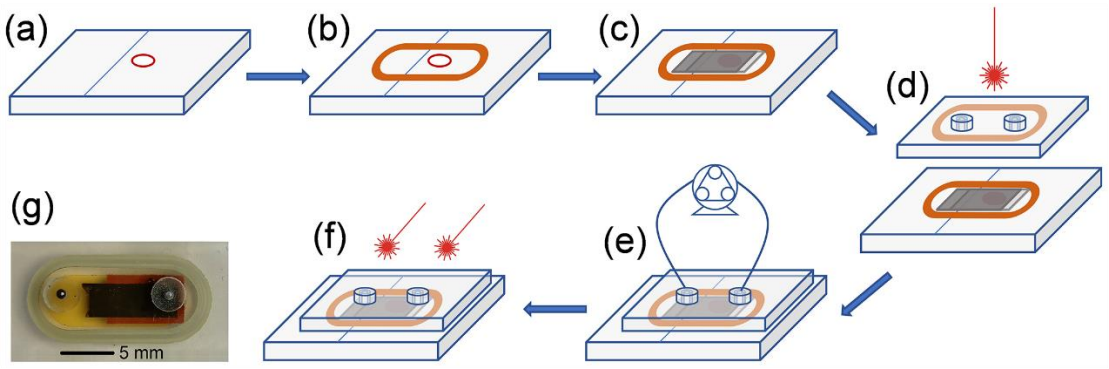

Fig. 4.1 Manufacturing flow chart (***a-f***) and photograph (***g***) of glass-sealed M-DSSC.

Scribed and cleaned FTO-coated glasses were covered with *ca.* 80±5 nm blocking-layer of TiO_2 deposited by spray pyrolysis at 450 ºC; the spray solution was made of 7.0 mL anhydrous isopropyl alcohol + 0.6 mL titanium diisopropoxide bis(acetylacetonate) + 0.4 mL of acetylacetone. A circular-shaped (4 mm in diameter) mesoporous TiO_2 layer with a thickness of 7±1 μm was formed by screen-printing of 30NR-D titania paste and annealing at 500 ºC (1 hour). The mesoporous TiO_2 layer was treated by dipping in 40 mM $TiCl_4$ solution at 70 ºC for 30 minutes, dried, and annealed at 500 ºC (**Fig. 4.1a**). A thin oval-shaped frame of the glass paste was screen-printed on the FTO glass, around the mesoporous TiO_2 layer, and sintered at 490 ºC for 60 minutes (**Fig. 4.1b**). An insulating spacer layer, with a thickness of 6±1 μm, was deposited atop mesoporous TiO_2 by screen-printing of conventional rutile paste (WER2-O) followed by sintering at 500 ºC for 1 hour. A 20±5 μm thick graphite/carbon-black counter-electrode was applied over the insulating spacer layer by doctor-blading of Elcocarb B/SP paste and sintered at 420 ºC for 45 minutes (**Fig. 4.1c)**. The cover glass was prepared by engraving the electrolyte injection holes in thin capillaries fabricated by laser ablation on one side of the glass and depositing identical glass frit sealing frame on the other side. The front FTO glass was aligned with the cover glass so that the frits frames match each other (**Fig. 4.1d**); a laser-assisted glass-frit bonding process, as described elsewhere [37], was used for sealing the cell edges. The photoanode sensitization was then obtained by closed-loop pumping for 5 hours (recirculation) of 10 mL, 0.1 mM Y123 dye in a solvent acetonitrile/*t*-butanol (1:1) volume ratio (**Fig. 4.1e**). The cavity of the cell was then cleaned through passing acetonitrile and dried with nitrogen. Electrolyte made of 0.165 M Co(II) and 0.045 M Co(III) tris(bipyridyl)tetracyanoborate complexes, 1.2 M TBP, and 0.1 M $LiClO_4$ was injected into the cavity; the tops of the injection glass capillaries were melted by fast heating using the laser beam (**Fig. 4.1f**), completing the device assembly and glass encapsulation (**Fig. 4.1g**).

For comparison with glass-sealed M-DSSCs, a batch of Surlyn sealed devices was also prepared. The cover glass with pre-drilled cylindrical injection holes (0.7 mm) was bonded to the device using a Surlyn spacer and hot pressing. After electrolyte injection, the holes were closed using Surlyn film with lamella glass on top.

Hermeticity and robustness of the device encapsulation were assessed by the standard helium gas leak test MIL-STD-883 method 1014.10 [40], before and after five humidity-freeze cycles corresponding to IEC 61646 standard [41]. Each humidity-freeze cycle included sample exposure to 85 ºC and 85 % relative humidity for 20 hours, then cooling to -40 ºC, without humidity control, and holding at -40 ºC for 30 minutes. Interested readers may consult the ref. [42] for details of the He-leakage and humidity-freeze test conditions.

Briefly, the obtained He-gas leak rates allowed the calculation of the equivalent air leak rates (L). L is used to assess the hermeticity of the device. Values of L below the reject limit indicate that the device hermeticity meets the standard. Considering the internal volume of the sealed devices is 1.2×10^{-2} cm^3, the reject limit (L) is 1×10^{-7} $atm\cdot cm^3\cdot s^{-1}$ [40].

Fig. 4.2 presents leak rates L for as prepared empty devices sealed with glass and polymer, subjected to five humidity-freeze cycles.

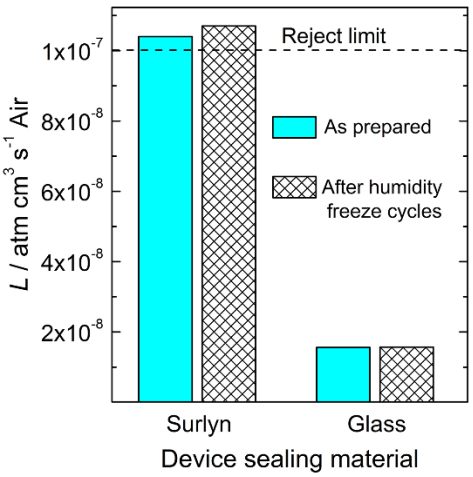

Fig. 4.2 Leak rates L according to MIL-STD-883 test conditions of glass and polymer sealed empty cells, before and after 5 humidity-freeze cycles according to IEC 61646 protocol.

Thermoplastic sealed devices show L values above the reject limit, meaning poor hermeticity, which, in addition, degraded under humidity-freeze cycles. Glass-sealed cells display L rates *ca*. 10 times less than the reject limit, demonstrating superior hermeticity. Encapsulation with glass withstands the standard IEC61646 humidity-freeze test, showing no signs of hermeticity deterioration.

Glass encapsulation involves more manufacturing steps, where the new steps may affect the PCE of the devices. However, freshly prepared glass and polymer sealed cells show almost identical current-potential (*J-V*) characteristics. The average 1-sun PCE of a batch of 7 devices was 8.0±0.5 %, and 7.9±0.4 % for glass and polymer encapsulated cells, respectively.

4.2.3 Characterization

A batch of 4 devices was subjected to a) He leak rates, measured using an Adixen ASM 142 mass spectrometer with a sensitivity of $5 \cdot 10^{-12}$ atm·cm^3·s^{-1} to He, and b) humidity-freeze cycle test, performed in a climatic chamber – Fitoclima (Aralab). Detailed protocols of ISOS tests can be found somewhere [34]. For temperature effect studies, the temperature of M-DSSCs was controlled using an in-house made experimental set-up [43] constructed from Peltier element (Marlow Industries, model RC12-6) connected to a Keithley power supply (Model 2425C). An Autolab electrochemical station (PGSTAT 302 N, Metrohm) was used to record *J-V* characteristics and to perform the electrochemical impedance spectroscopy (EIS) characterization. The EIS data were analyzed in ZView® software. A solar simulator MiniSol (LSH-7320, Newport) was used as a source of AM1.5G (100 mW·cm^{-2}) light.

The stability of the glass-sealed and polymer-sealed M-DSSCs devices was evaluated during 1000 h under continuous 850 W·m^{-2} light soaking at 45 ºC in a climatic chamber Atlas SUNTEST equipped with Xe lamp and AM1.5G filter; UV filter was used to cut the radiation below 390 nm.

A LED lamp (Osram, Class A+, 60 W, 2700 K with emission spectra presented in **Fig. 4.3**) was used as the light source for the artificial light-soaking test. The incident light intensity from the LED lamp was calibrated using a radiometer Delta Ohm HD 2102.2.

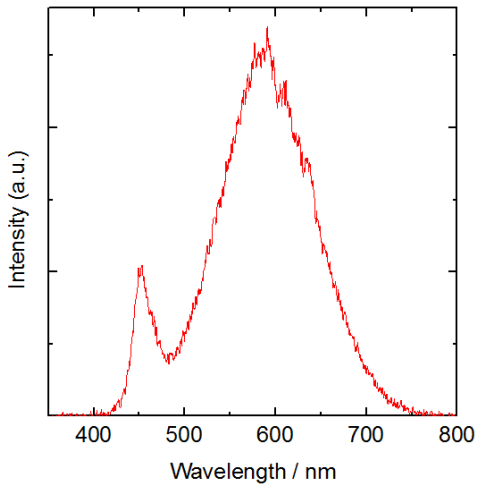

Fig. 4.3 Emission spectra of white LED lamp (Color temperature 2700 K) used for *J-V* characterization of the M-DSSCs under artificial room light.

During light-soaking tests, each M-DSSC was connected to a variable resistance as passive load. The resistance was adjusted to keep the M-DSSCs at their nominal operating potential, i.e. at the maximum power point. Adjustments of the connected resistance were made throughout the entire testing period, each time after measuring the device photoresponse.

The concentration of cobalt ions in the electrolyte before and after the device aging test was determined by dissolving a droplet (2 μL) of the electrolyte in 7 mL of distilled water and analyzing the solution using ICP-OES apparatus – iCAP 7000 (Thermo Scientific) with a detection limit for cobalt of 5 ppb.

4.3 Results and discussion

4.3.1. Photovoltaic behavior of cobalt M-DSSCs at the reversible heat impact according to ISOS-T-1

The certification of a photovoltaic device typically requires thermal cycling in the temperature range exceeding working conditions. Glass-encapsulated M-DSSCs successfully passed one heat cycle from room temperature to 85 ^{o}C, according to ISOS-T-1 protocol [34], showing no signs of electrolyte loss and retaining the initial PCE. Such a high setpoint temperature was never used before for testing devices with ACN since the boiling temperature of ACN is 82 ^{o}C. The Surlyn-based devices did not pass the test due to severe electrolyte leakage above *ca*. 67 ^{o}C.

Fig. 4.4 shows the normalized photovoltaic parameters of a glass-sealed M-DSSC at stepwise heating up to 85 ^{o}C, followed by a gradual temperature decrease.

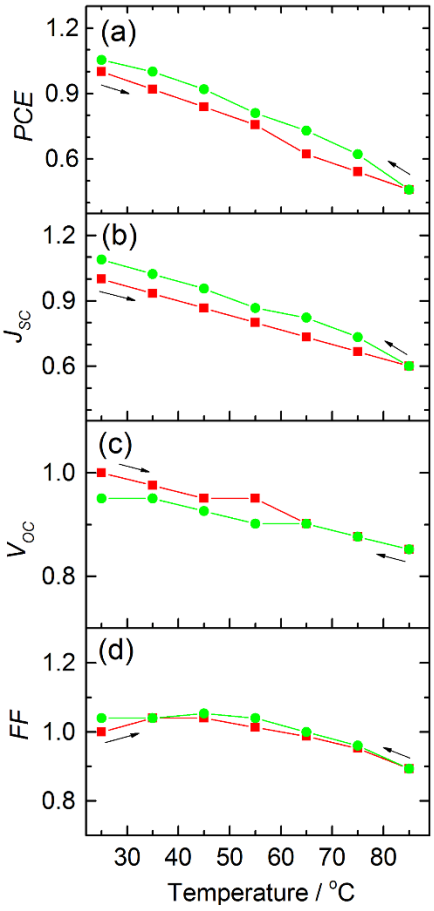

Fig. 4.4 Photovoltaic metrics of the M-DSSCs during ISOS-T-1 temperature cycle 25 ºC→ 85 ºC → 25 ºC; 0.7 ºC·min^{-1}. The PCE (***a***), J_{SC} (***b***), V_{OC} (***c***), and FF (***d***) are normalized to the values obtained at the beginning of the cycle at 25 ºC. The red squares and the green circles correspond to the rise and fall in temperature, respectively.

The M-DSSCs display an expectable deterioration of the PCE with the temperature (**Fig. 4.4a**), when moving from 25 °C to 85 °C, assigned to an increase of recombination at the photoanode/electrolyte interface [43,44]. At 85 ºC the V_{OC} and FF remained *ca*. 90 % of their initial values at 25 ºC. The temperature accelerates the overall charge transfer kinetics, including recombination, which may justify the decrease of V_{OC}. The drop of the overall PCE is caused mainly because of J_{SC} decrease (**Fig. 4.4b**); at 85 ºC the devices display 59 % and 60 % of the initial PCE and J_{SC}, respectively. With the device cooling down, the J_{SC} and PCE slightly improved, increasing *ca.* 1.05 times after the device cooled down to 25 ºC. However, the V_{OC} of the heat-treated devices decreased 5 % from the initial value.

EIS measurements at V_{OC} (forward bias in the dark) accessed the changes in the device after thermal cycling (**Fig. 4.5**). Impedance responses were collected before and after exposing the devices to the heating cycle and at the highest setpoint temperature of 85 ºC.

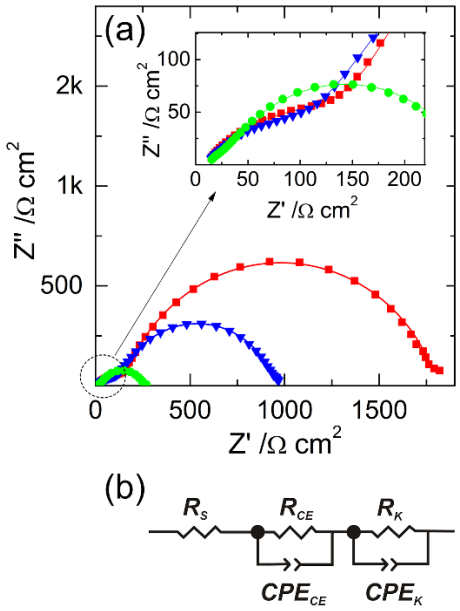

Fig. 4.5 Nyquist plots of the M-DSSC: initial at 25 ºC – red squares; at 85 ºC – green circles; after colling down to 25 ºC – blue triangles (***a***). Solid lines stand for the fits to the equivalent circuit [45,46], shown in chart (***b***).

The obtained Nyquist plots are typical for M-DSSCs [45,46] and show two well-resolved time constants. The first one appears at the high-frequency range with low impedance (inset in **Fig. 4.5a**) and corresponds to charge transfer at the counter-electrode/electrolyte interface. Another time constant shows up at lower frequencies due to the charge transfer at the photoanode/electrolyte interface and is commonly used to estimate the rate of back electron recombination with electrolyte; higher resistance corresponds to less recombination [47]. The equivalent electrical circuit shown in **Fig. 4.5b** fitted well with the EIS response, and it was used to identify the internal resistances of the devices. The elements in the model are series resistance (R_S), charge transfer resistances at the interfaces counter-electrode/electrolyte (R_{CE}), and photoanode/electrolyte (R_K); CPE_{CE} and CPE_K are the respective constant phase elements connected in parallel to the resistance. The values of resistances obtained from the fitting model are listed in **Table 4.1**.

Table 4.1

Values R_S, R_{CE}, and R_K (in $\Omega \cdot cm^2$) of the M-DSSC at different temperatures.

T /ºC	R_S	R_{CE}	R_K
Initial 25 ºC	10.0	148.7	1651.0
85 ºC	10.6	22.4	227.4
Final 25 ºC	10.3	125.3	817.3

The series resistance of the devices was not affected by temperature and remained almost constant during the temperature cycling. R_{CE} decreased drastically with the temperature, being *ca.* 6.6 times lower at 85 ºC when compared to the initial value – the charge transfer is accelerated with the temperature. When the device was cooled down, the R_{CE} did not return to its initial value – *ca.* 125 ($\Omega \cdot cm^2$) at the end *vs*. 148 ($\Omega \cdot cm^2$) initial. This was assigned to partial desorption of the dye from the carbon surface, which leads that more surface area of the electrode becoming accessible to electron exchange with cobalt ions. Although after the sensitization the cells were thoroughly cleaned at room temperature with a solvent, it is expected that a fraction of the dye did not desorb from the carbon layer. To confirm this assumption, a fresh carbon counter electrode (0.7 cm^2) layer was deposited onto glass, immersed into Y123 solution, vigorously rinsed with acetonitrile at room temperature, and dipped into 1 mL of acetonitrile in a closed vessel. The vessel was held at 65 °C and at 75 ºC for 10 minutes; after each temperature exposure, the absorption spectra of the acetonitrile were taken (**Fig. 4.6**). The dye release from the carbon counter-electrode is evidenced by an increase in the absorption in the 400-530 nm region, characteristic of Y123 dye [48].

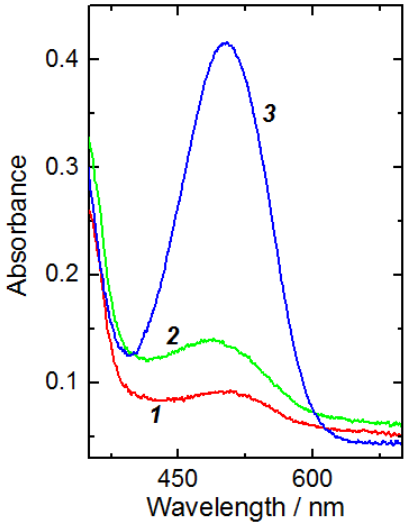

Fig. 4.6 Absorption spectra of acetonitrile after immersion of the carbon counter-electrode for 10 minutes at 65 ºC (**1**) and 75 ºC (**2**). Absorbance spectra of 0.01 M solution of Y123 dye (**3**) in acetonitrile/*t*-butanol mixture (1:1 volume ratio).

The resistance R_K is most strongly and irreversibly affected by temperature. At 85 ºC, R_K falls *ca.* 7.3 times, leading to faster recombination and to the drop of the photocurrent (**Fig. 4.4b**). When the device is cooled back to 25 ºC, R_K restored *ca.* 2.6 part of the initial - 817 ($\Omega \cdot cm^2$) at the end *vs.* 1651 ($\Omega \cdot cm^2$) initial. This is in line with previously reported electron lifetime reduction in heat-treated cobalt DSSCs [26] and consistent with the observed drop in V_{OC} (**Fig. 4.4c**). The slight improvement of the photocurrent (**Fig. 4.4b**) was assigned to the positive shift of the conduction band edge potential of TiO_2 due to dye desorption [26]. However, strong dye desorption should cause the photocurrent to drop. The absorption spectra of the photoanode were taken before and after the immersion in a heated electrolyte (**Fig. 4.7**).

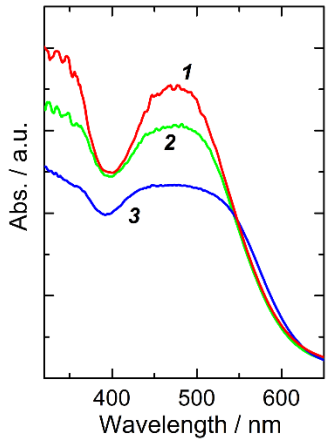

Fig. 4.7 Absorbance spectra of the photoanode right after sensitization (**1**); after being in contact with electrolyte in the device at 65 ºC (**2**) and at 85 ºC (**3**).

Freshly sensitized photoanode displays a broad band centered at 438 nm, matching Y123 absorption. After being in contact with electrolytes at elevated temperatures, the absorption of the photoanode in the wavelength range of 400-530 nm drops *ca.* 1.2 and 1.5 times at 65 and 85 °C, respectively. The dye equivalent to the absorption decrease was desorbed from the mesoporous titania. Since the dye desorption does not lead to a significant photocurrent drop (the amount of the desorbed dye is rather high), on the contrary, it slightly improves, it can be assumed that adsorbed dye aggregates present at mesoporous TiO_2 surface of the fresh device leave the photoanode after the temperature cycle. A decrease in the R_K value after the heating cycle (**Table 4.1**) corresponds to this assumption. In the as-prepared device, i.e. before the heating cycle, the aggregated dye molecules prevent charge transfer at the photoanode/electrolyte interface, originating a high R_K resistance. Hence, optimization of the sensitization conditions should be addressed in future studies.

4.3.2. Aging of cobalt M-DSSCs in the dark and under simulated solar light soaking according to ISOS D-1 and modified ISOS-L-2 protocols, respectively

Fig. 4.8a and **b** show the history of photovoltaic metrics of the glass-sealed M-DSSCs at natural aging in dark conditions according to ISOS-D-1.

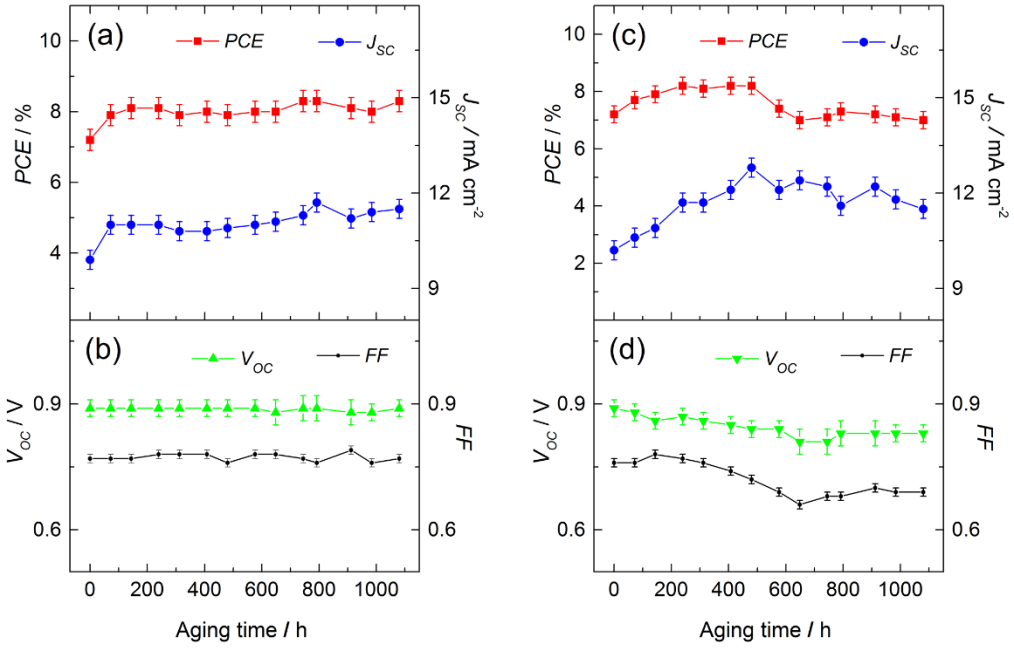

Fig. 4.8 History of the photovoltaic metrics of hermetically sealed cobalt M-DSSCs during aging in the dark (***a***,***b***) and under simulated solar light soaking (***c***,***d***), according to ISOS-D-1 and modified ISOS-L-2 for 45 °C of operation.

The cells display a well-defined increase of the PCE from *ca.* 7 % initial to 8 % within the first 200 h of aging and maintained until the end of the 1000 h test, displaying full stability. Initial

improvement of the PCE is mainly due to J_{SC}, as FF and V_{OC} remained constant within the entire testing period. EIS study revealed minor changes in impedance response of the cells before and after dark aging (**Fig. 4.9a**). Charge transfer resistance on photoanode R_K dropped slightly from 1.76 kΩ·cm^2 to 1.61 kΩ·cm^2 after aging, while R_{CE} increased from 68 Ω·cm^2 to 88 Ω·cm^2. Small changes in the charge transfer resistances point to the high stability of all internal components and interfaces of the M-DSSCs, which are in line with the history of the photovoltaic metrics (**Fig. 4.8 a,b**).

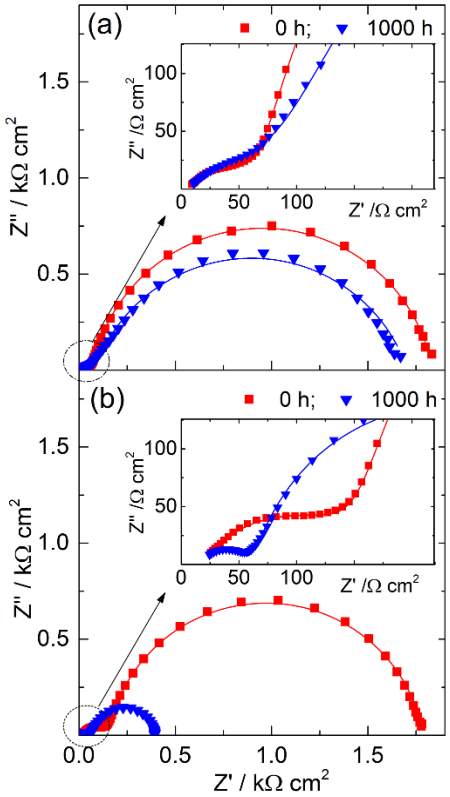

Fig. 4.9 Nyquist plots of the glass-encapsulated M-DSSCs before (red squares) and at the end (blue triangles) of aging in the dark (***a***) and under simulated solar light soaking (***b***) according to ISOS-D-1 and modified ISOS-L-2 (45 °C), respectively. Solid lines are the fittings obtained using the electrical equivalent circuit shown in **Fig. 4.5b**.

The batch of the devices sealed with Surlyn barely accomplished ISOS-D-1 test, initially demonstrating similar PCE improvement compared with the glass encapsulated devices, within 200 h (**Fig. 4.10a**).

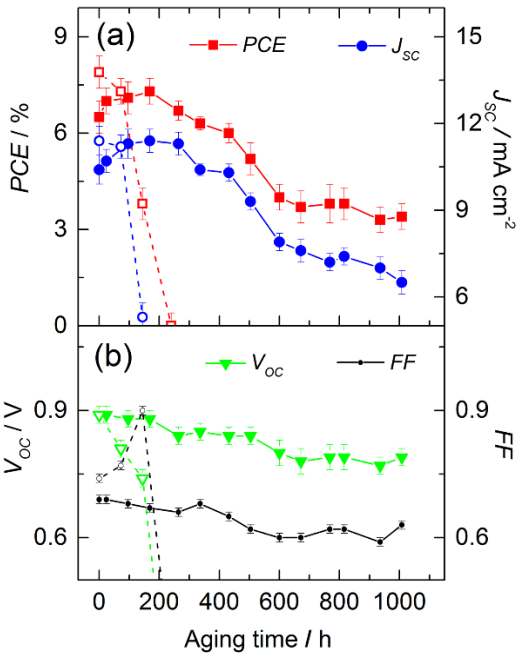

Fig. 4.10 Photovoltaic metrics *vs*. time of the polymer-sealed M-DSSCs – PCE and J_{SC} (***a***), V_{OC} and FF (***b***) in the course of natural aging in the dark (solid symbols) and under simulated solar light soaking (empty symbols).

However, after the initial 200 h, the degradation of the cell onsets, ultimately leading to the devices with only 3 % of the PCE. The apparent reason for PCE deterioration was electrolyte leakage visualized at *ca*. 300 h. Nevertheless, devices with electrolyte leakage accomplished 1000 h of aging in the dark, constantly displaying a drop on J_{SC}, V_{OC}, and FF (**Fig. 4.10b**). At the light-soaking test, devices encapsulated with Surlyn survived only 200 h until PCE dropped to zero (**Fig. 4.10a**).

Fig. 4.8c and **d** show photovoltaic metrics *vs.* time of the glass-sealed M-DSSC as they were exposed to simulated sunlight (850 W·m^{-2}) at *ca*. 45 ^{o}C, and connected to an electrical resistance for operating at maximum power point conditions. From *ca*. 7.2 % of the initial value, the PCE decreased after 1000 h of continuous illumination to 7.0 %, which is within the error of the reads. The average response history of the glass-encapsulated devices was more complex. PCE gradually increased until instant 200 h, reaching *ca*. 8.2 %, stabilized for the next 300 h, decreased for the next 200 h, and stabilized afterward; J_{SC} constantly raised until instant 500 h, slightly decreasing afterward; FF and V_{OC} displayed a slight dropping trend within the whole testing period of 1000 h.

The prolonged period of PCE constant improvement, 200 h, is observed for the first time; previous reports concerning the initial 500 h of light-soaking history of similar Surlyn-sealed devices display quite the opposite behavior [23-25,27]. J. Gao *et al.* [23] observed *ca*. 20 % of PCE deterioration mainly due to pronounced drop of V_{OC} and FF (1-sun; 60 ^{o}C); R. Jiang *et al.* [25]

reported very stable V_{OC}, but descending FF and J_{SC} leads to *ca*. 25 % loss of the original PCE (1-sun, 20 ^{o}C, open-circuit); A. Kamppinen *et al.* [24] obtained *ca*. 25 % PCE drop caused by V_{OC} and FF decrease (1-sun, 40 ^{o}C, open-circuit).

The observed 200 h PCE improvement in continuously working devices is due to the continuous J_{SC} increase. The origin and mechanism of light-induced photocurrent improvement are quite interesting and profoundly studied elsewhere in ref. [49], using LEG1 and PD2 as modeling dyes. Briefly, in the presence of a Lewis base such as TBP, adsorbed dye molecules are reorganized on the TiO_2 surface and partially substituted with TBP. This process is accelerated under illumination and leads to an up-shift of dye LUMO level and down-shift of TiO_2 conduction band; the driving force for electron injection is increased.

Later, after *ca*. 500 h, the photocurrent started to decrease, along with FF and V_{OC}. The decrease of the FF value is assumed to be related to the increase of the concentration of Co(III) in the pores of the TiO_2 mesoporous layer, which impairs the diffusion of Co(III) [25]. Accumulation of cobalt ions in the mesoporous layer should affect the electrolyte composition. Cobalt ions concentration in the electrolyte of aged devices has not been previously determined. Our findings show that the concentration of cobalt ions (total Co(III) and Co(II)) in the electrolyte surrounding the device, after light soaking, is 0.12 M, i.e. became 1.7 times lower than the initial 0.21 M. This implies that cobalt complexes concentration drastically increases in the porous triple-layer sandwich of the M-DSSC. The exact determination of the amount of Co(III) and Co(II) mainly adsorbed by each layer of the monolithic device is challenging but should be addressed in future studies. The drop of cobalt concentration justifies the bleaching of the electrolyte around the M-DSSC layers (**Fig. 4.11**).

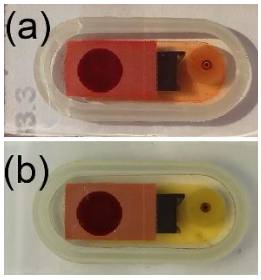

Fig. 4.11 Photographs of the glass-sealed M-DSSCs taken before (***a***) and after 1000 h (***b***) of accelerated aging under 850 W·m^{-2} simulated solar light.

Impedance spectra of light-aged M-DSSCs display a drastic acceleration of charge transfer (recombination) at the photoanode/electrolyte interface: R_K decreases from 1.63 kΩ·cm^2 to 337 Ω·cm^2 at the end of the test (**Fig. 4.9b**). The reduction of R_K fits well with the observed accumulation of cobalt ions in the M-DSSC layers; upon increasing cobalt complex concentration, the interfacial charge transfer increases, as expected. Among other reasons that could cause R_K to

decrease is partial dye desorption [49]. What is quite interesting here is that, despite the observed significant changes in the interfacial charge transfer, accompanied by changes of local concentration of cobalt complexes in the device, the overall PCE is practically not affected.

The photovoltaic metrics of the cells for the last *ca.* 250 h of the test is relatively stable, especially regarding V_{OC} and FF, and the full lifespan of the device cannot be predicted yet. A testing period longer than 1000 h is desirable for future studies.

4.3.3. Artificial 600 lx and 1000 lx light soaking

The requirements for long-term stability testing of PV devices under artificial indoor light are not clearly defined yet, and there is no standard lamp spectrum for indoor PV testing [50,51]. As the share of LEDs in the market for indoor lighting is increasing, we used a LED lamp of Class A+ with a color temperature of 2700 K and emission spectra as presented in **Fig. 4.3**.

The devices were aged for 1000 h under 600 lx, the temperature of *ca.* 22-26 ^{o}C in a close compartment, with a device connected to passive resistance load. *J-V* characteristics were recorded periodically under 600 lx and 1000 lx; **Fig. 4.12a,b** presents the history of the photovoltaic metrics.

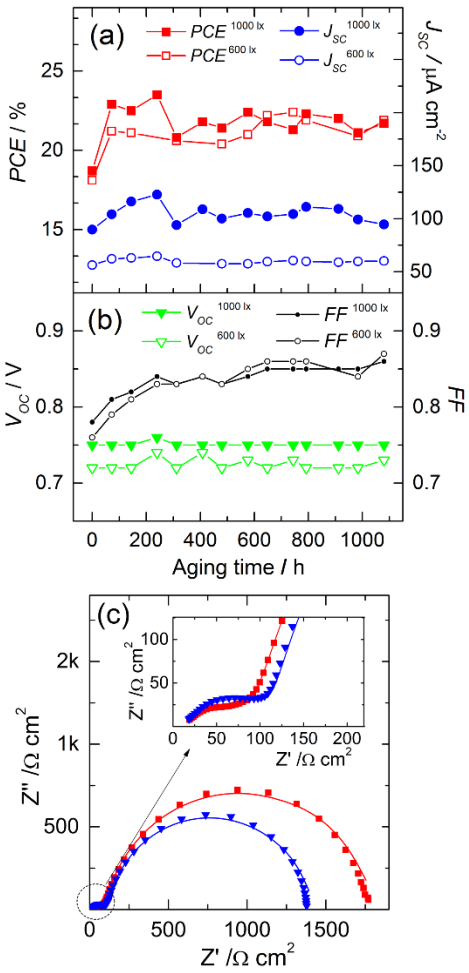

Fig. 4.12 Photovoltaic metrics *vs*. time of the glass-sealed M-DSSCs in the course of 600 lx LED light soaking (***a,b***) and EIS responses of the devices before (red squares) and after (blue triangles) artificial light soaking test (***c***).

After 1000 h of aging, the overall PCE improved 20 % and 16 % under 600 lx and 1000 lx, respectively. The variations in PCE are mostly related to small fluctuations in photocurrent, which might be due to minor variations in the incident light intensity. Aging under low artificial lighting indoors causes much less stress on cells, as shown in **Fig. 4.12c** – EIS probing before and after the test. The charge transfer resistance at the photoanode and counter-electrode slightly decrease, similar to shelf-aging at room temperature in the dark (**Fig. 4.9a**). To the best of our knowledge, this is the most stable DSSC employing ACN cobalt electrolyte reported so far, under artificial light soaking. The history of PCE shows that liquid-junction M-DSSCs are very promising as power sources, albeit with low but steady power under indoor illumination.

4.4 Conclusions

Hermetic encapsulation of liquid-junction cobalt M-DSSCs with ACN is absolutely essential for a stable photovoltaic response under ISOS testing conditions. Glass-encapsulated M-DSSCs showed fully stable PCE in the dark and under continuous operation under artificial light. Robust encapsulation allowed for the first time ever to test the devices with ACN electrolyte according to the ISOS thermal cycle protocol at 85 ^{o}C. After heating to 85 °C, the M-DSSCs retained the initial PCE, however, with profound intrinsic changes attributed to dye desorption and acceleration of charge transport at the photoanode/electrolyte interface. Continuous 1000 h operating with a passive load under simulated solar light led to a drastic increase of charge transfer at the photoanode and redistribution of cobalt ions over the device; nevertheless, and for the first time ever, the PCE showed mostly a constant value over the entire testing period. This is one of the most impressive conclusions of this report; after increasing interfacial charge transfer, dye desorption, and a concentration gradient of cobalt ions over the cell cavity, the overall PCE is only slightly deteriorated or even unaffected.

Full glass encapsulation proved to be a keystone for the stability of cobalt-based DSSC devices and critical for in-deep study of the internal degradation mechanisms. Longer tests are now possible, opening the doors to the development of more stable and performing devices.

Acknowledgments

F. Santos and J. Martins acknowledge the FCT for their PhD grants reference SFRH/BD/132388/2017 and SFRH/BD/147201/2019, respectively; J. Capitão acknowledges LEPABE for his PhD grant reference UI/BD/150993/2021. The research leading to these results also received funding from: i) project 2SMART - engineered Smart materials for Smart citizens, with reference NORTE-01-0145-FEDER-000054, supported by Norte Portugal Regional Operational Programme (NORTE 2020), under the PORTUGAL 2020 Partnership Agreement, through the European Regional Development Fund (ERDF); ii) project HopeH2, with reference POCI-01-0145-FEDER-030760, funded by FEDER funds through COMPETE2020 – Programa Operacional Competitividade e Internacionalização (POCI) and by national funds (PIDDAC) through FCT/MCTES; and iii) LA/P/0045/2020 (ALiCE), UIDB/00511/2020 and UIDP/00511/2020 (LEPABE), funded by national funds through FCT/MCTES (PIDDAC).

References

[1] A.B. Muñoz-García, I. Benesperi, G. Boschloo, J.J. Concepcion, J.H. Delcamp, E.A. Gibson, G.J. Meyer, M. Pavone, H. Pettersson, A. Hagfeldt, M. Freitag, Dye-sensitized solar cells strike back, *Chem. Soc. Rev.*, 2021, 50, 12450–12550. DOI: 10.1039/d0cs01336f.

[2] D. Zhang, M. Stojanovic, Y. Ren, Y. Cao, F.T. Eickemeyer, E. Socie, N. Vlachopoulos, J.E. Moser, S.M. Zakeeruddin, A. Hagfeldt, M. Grätzel, A molecular photosensitizer achieves a Voc of 1.24 V enabling highly efficient and stable dye-sensitized solar cells with copper(II/I)-based electrolyte, *Nat. Commun*. 2021, 12, 2–11. DOI:10.1038/s41467-021-21945-3.

[3] B. O'Regan, M. Grätzel, A low-cost, high-efficiency solar cell based on dye-sensitized colloidal TiO_2 films, *Nature*, 1991, 353, 737–740. DOI: 10.1038/353737a0.

[4] M.L. Parisi, S. Maranghi, L. Vesce, A. Sinicropi, A. Di Carlo, R. Basosi, Prospective life cycle assessment of third-generation photovoltaics at the pre-industrial scale: A long-term scenario approach, *Renew. Sustain. Energy Rev.*, 2020, 121, 109703. DOI: 10.1016/j.rser.2020.109703.

[5] N. Mariotti, M. Bonomo, L. Fagiolari, N. Barbero, C. Gerbaldi, F. Bella, C. Barolo, Recent advances in eco-friendly and cost-effective materials towards sustainable dye-sensitized solar cells, Green Chem., 2020, 22, 7168-7218. DOI: 10.1039/d0gc01148g.

[6] M. Kokkonen, P. Talebi, J. Zhou, S. Asgari, S.A. Soomro, F. Elsehrawy, J. Halme, S. Ahmad, A. Hagfeldt, S.G. Hashmi, Advanced research trends in dye-sensitized solar cells, *J. Mater. Chem. A*, 2021, 9, 10527–10545. DOI: 10.1039/d1ta00690h.

[7] M.K. Mishu, M. Rokonuzzaman, J. Pasupuleti, M. Shakeri, K.S. Rahman, F.A. Hamid, S.K. Tiong, N. Amin, Prospective efficient ambient energy harvesting sources for IoT-equipped sensor applications, *Electronics*, 2020, 9, 1345. DOI: 10.3390/electronics9091345.

[8] I. Mathews, S.N. Kantareddy, T. Buonassisi, I.M. Peters, Technology and market perspective for indoor photovoltaic cells, *Joule*, 2019, 3, 1415–1426. DOI: 10.1016/j.joule.2019.03.026.

[9] H. Michaels, M. Rinderle, R. Freitag, I. Benesperi, T. Edvinsson, R. Socher, A. Gagliardi, M. Freitag, Dye-sensitized solar cells under ambient light powering machine learning: Towards autonomous smart sensors for the Internet of things, *Chem. Sci.*, 2020, 11, 2895–2906. DOI: 10.1039/c9sc06145b.

[10] A. Aslam, U. Mehmood, M.H. Arshad, A. Ishfaq, J. Zaheer, A. Ul Haq Khan, M. Sufyan, Dye-sensitized solar cells (DSSCs) as a potential photovoltaic technology for the self-powered internet of things (IoTs) applications, *Sol. Energy*, 2020, 207, 874–892. DOI: 10.1016/j.solener.2020.07.029.

[11] J.H. Yum, E. Baranoff, F. Kessler, T. Moehl, S. Ahmad, T. Bessho, A. Marchioro, E. Ghadiri, J.E. Moser, C. Yi, Md. K. Nazeeruddin, M. Grätzel, A cobalt complex redox shuttle for dye-sensitized

solar cells with high open-circuit potentials, *Nat. Commun.*, 2012, 3, 631. DOI: 10.1038/ncomms1655.

[12] K. Kakiage, Y. Aoyama, T. Yano, K. Oya, J. Fujisawa, M. Hanaya, Highly-efficient dye-sensitized solar cells with collaborative sensitization by silyl-anchor and carboxy-anchor dyes, *Chem. Commun.*, 2015, 51, 15894–15897. DOI: 10.1039/C5CC06759F.

[13] J.M. Ji, H. Zhou, Y.K. Eom, C.H. Kim, H.K. Kim, 14.2% Efficiency Dye-Sensitized Solar Cells by Co-Sensitizing Novel Thieno[3,2-b]indole-Based Organic Dyes with a Promising Porphyrin Sensitizer, *Adv. Energy Mater.*, 2020, 10, 1–12. DOI: 10.1002/aenm.202000124.

[14] S. Mathew, A. Yella, P. Gao, R. Humphry-Baker, B.F.E. Curchod, N. Ashari-Astani, I. Tavernelli, U. Rothlisberger, M.K. Nazeeruddin, M. Grätzel, Dye-sensitized solar cells with 13% efficiency achieved through the molecular engineering of porphyrin sensitizers, *Nat. Chem.*, 2014, 6, 242–247. DOI: 10.1038/nchem.1861.

[15] J.S. Kang, J. Kim, J.Y. Kim, M.J. Lee, J. Kang, Y.J. Son, J. Jeong, S.H. Park, M.J. Ko, Y.E. Sung, Highly Efficient Bifacial Dye-Sensitized Solar Cells Employing Polymeric Counter Electrodes, *ACS Appl. Mater. Interfaces*, 2018, 10(10), 8611–8620. DOI: 10.1021/acsami.7b17815.

[16] J. De Peng, Y.T. Wu, M.H. Yeh, F.Y. Kuo, R. Vittal, K.C. Ho, Transparent Cobalt Selenide/Graphene Counter Electrode for Efficient Dye-Sensitized Solar Cells with Co2+/3+-Based Redox Couple, *ACS Appl. Mater. Interfaces*, 2020, 12(40), 44597–44607. DOI: 10.1021/acsami.0c08220.

[17] S. Ito, S.M. Zakeeruddin, P. Comte, P. Liska, D. Kuang, M. Grätzel, Bifacial Dye-Sensitized Solar Cells Based on an Ionic Liquid Electrolyte, *Nat. Photonics*, 2008, 2(11), 693–698. DOI: 10.1038/nphoton.2008.224.

[18] J. Wu, Y. Li, Q. Tang, G. Yue, J. Lin, M. Huang, L. Meng, Bifacial Dye-Sensitized Solar Cells: A Strategy to Enhance Overall Efficiency Based on Transparent Polyaniline Electrode, *Sci. Rep.*, 2014, 4, 1–7. DOI: 10.1038/srep04028.

[19] F. Bella, S. Galliano, C. Gerbaldi, G. Viscardi, Cobalt-based electrolytes for dye-sensitized solar cells: Recent advances towards stable devices, *Energies*, 2016, 9, 1–22. DOI: 10.3390/en9050384.

[20] M.K. Kashif, M. Nippe, N.W. Duffy, C.M. Forsyth, C.J. Chang, J.R. Long, L. Spiccia, U. Bach, Stable Dye-Sensitized Solar Cell Electrolytes Based on Cobalt(II)/(III) Complexes of a Hexadentate Pyridyl Ligand, *Angew. Chem. Int. Ed*., 2013, 52: 5527-5531. DOI: 10.1002/anie.201300070.

[21] D. Xu, H. Zhang, X. Chen, F. Yan, Imidazolium Functionalized Cobalt Tris(bipyridyl) Complex Redox Shuttles for High Efficient Ionic Liquid Electrolyte Dye-Sensitized Solar Cells, *J. Mater. Chem. A*, 2013, 1, 11933-11941. DOI: 10.1039/C3TA12031G.

[22] M. Freitag, W. Yang, L.A. Fredin, L. D'Amario, K.M. Karlsson, A. Hagfeldt, G. Boschloo, Supramolecular Hemicage Cobalt Mediators for Dye-Sensitized Solar Cells, *ChemPhysChem*, 2016, 17, 3845. DOI: 10.1002/cphc.201600985.

[23] J. Gao, M.B. Achari, L. Kloo, Long-Term Stability for Cobalt-Based Dye-Sensitized Solar Cells obtained by Electrolyte Optimization, *Chem. Commun*., 2014, 50(47), 6249-6251. DOI: 10.1039/c4cc00698d.

[24] A. Kamppinen, K. Aitola, A. Poskela, K. Miettunen, P. Lund, Stability Of Cobalt Complex Based Dye Solar Cells With PEDOT And Pt Catalysts And Different Electrolyte Concentrations, *Electrochim. Acta*, 2020, 335, 135652. DOI: 10.1016/j.electacta.2020.135652.

[25] R. Jiang, A. Anderson, P. Barnes, L. Xiaoe, C. Law, B. O'Regan, 2000 Hours Photostability Testing Of Dye Sensitized Solar Cells Using A Cobalt Bipyridine Electrolyte, *J. Mater. Chem. A*, 2014, 2, 4751-4757. DOI: 10.1039/C4TA00402G.

[26] W. Yang, Y. Hao, P. Ghamgosar, G. Boschloo, Thermal Stability Study of Dye-Sensitized Solar Cells with Cobalt Bipyridyl–based Electrolytes, *Electrochim. Acta*, 2016, 213, 879–886. DOI: 10.1016/j.electacta.2016.07.112.

[27] J. Gao, W. Yang, M. Pazoki, G. Boschloo, L. Kloo, Cation-Dependent Photostability of Co(II/III)-Mediated Dye-Sensitized Solar Cells, *J. Phys. Chem. C*, 2015, 119, 44, 24704-24713. DOI: 10.1021/acs.jpcc.5b06310.

[28] K. Miettunen, T. Saukkonen, X. Li, C. Law, Y. Sheng, J. Halme, A. Tiihonen, P. Barnes, T. Ghaddar, M.I. Asghar, P. Lund, B. O'Regan, Do Counter Electrodes on Metal Substrates Work with Cobalt Complex Based Electrolyte in Dye Sensitized Solar Cells?, *J. Electrochem. Soc*., 2012, 160, H132-H137. DOI: 10.1149/2.074302jes.

[29] W. Xiang, W. Huang, U. Bach, L. Spiccia, Stable high efficiency dye-sensitized solar cells based on a cobalt polymer gel electrolyte, *Chem. Commun*., 2013, 49, 8997-8999. DOI: 10.1039/C3CC44555K.

[30] F. Bella, N. Vlachopoulos, K. Nonomura, S.M. Zakeeruddin, M. Grätzel, C. Gerbaldi, A. Hagfeldt, Direct Light-Induced Polymerization Of Cobalt-Based Redox Shuttles: An Ultrafast Way Towards Stable Dye-Sensitized Solar Cells, *Chem. Commun*., 2015, 51(91), 16308–16311. DOI:10.1039/c5cc05533d.

[31] G. Sonai, A. Tiihonen, K. Miettunen, P. Lund, A. Nogueira, Long-Term Stability of Dye-Sensitized Solar Cells Assembled with Cobalt Polymer Gel Electrolyte, *J. Phys. Chem. C*, 2017, 121, 33, 17577–17585. DOI: 10.1021/acs.jpcc.7b03865.

[32] X.L. Zhang, W. Huang, A. Gu, W. Xiang, F. Huang, Z.X. Guo, Y.B. Cheng, L. Spiccia, High efficiency solid-state dye-sensitized solar cells using a cobalt(II/III) redox mediator, *J. Mater. Chem. C*, 2017, 5, 4875–4883. DOI: 10.1039/c7tc00994a.

[33] F. Corsini, G. Griffini, Recent progress in encapsulation strategies to enhance the stability of organometal halide perovskite solar cells, *JPhys Energy*, 2020, 2, 031002. DOI: 10.1088/2515-7655/ab8774.

[34] M.O. Reese, S.A. Gevorgyan, M. Jørgensen, E. Bundgaard, S.R. Kurtz, D.S. Ginley, D.C. Olson, M.T. Lloyd, P. Morvillo, E.A. Katz, et al., Consensus stability testing protocols for organic photovoltaic materials and devices, *Sol. Energy Mater. Sol. Cells*, 2011, 95, 1253–1267. DOI: 10.1016/j.solmat.2011.01.036.

[35] M.V. Khenkin, E.A. Katz, A. Abate, G. Bardizza, J.J. Berry, C. Brabec, F. Brunetti, V. Bulović, Q. Burlingame, A. Di Carlo, et al., Consensus statement for stability assessment and reporting for perovskite photovoltaics based on ISOS procedures, *Nat. Energy*, 2020, 5, 35–49. DOI: 10.1038/s41560-019-0529-5.

[36] F. Santos, C. Hora, D. Ivanou, A. Mendes, Efficient Liquid-Junction Monolithic Cobalt-Mediated Dye-Sensitized Solar Cells for Solar and Artificial Light Conversion, *ACS Appl. Energy Mater.*, 2021, 4, 5, 5050–5058. DOI: 10.1021/acsaem.1c00616.

[37] D.K. Ivanou, R. Santos, J. Maçaira, L. Andrade, A. Mendes, Laser assisted glass frit sealing for production large area DSCs panels, *Sol. Energy*, 2016, 135, 674–681. DOI: 10.1016/j.solener.2016.06.043.

[38] S. Emami, J. Martins, D. Ivanou, A. Mendes, Advanced Hermetic Encapsulation of Perovskite Solar Cells: The Route to Commercialization, *J. Mater. Chem. A*, 2020, 8, 2654-2662. DOI: 10.1039/C9TA11907H.

[39] J. Martins, S. Emami, R. Madureira, J. Mendes, D. Ivanou, A. Mendes, Novel Laser-Assisted Glass Frit Encapsulation for Long-Lifetime Perovskite Solar Cells, *J. Mater. Chem. A*, 2020, 8, 20037–20046. DOI: 10.1039/d0ta05583b.

[40] MIL-STD-883H, Test method standard microcircuits. 2010, United States Department of Defense.

[41] IEC61646. 2008 Thin-film terrestrial photovoltaic (PV) modules - design qualification and type approval.

[42] S. Emami, J. Martins, R. Madureira, D. Hernandez, G. Bernardo, J. Mendes, Development of hermetic glass frit encapsulation for perovskite solar cells, *J. Phys. D: Appl. Phys*., 2019, 52, 074005. DOI: 10.1088/1361-6463/aaf1f4.

[43] J. Maçaira, I. Mesquita, L. Andrade, A. Mendes, Role of Temperature in the Recombination Reaction on Dye-Sensitized Solar Cells, *Phys. Chem. Chem. Phys*., 2015, 17, 22699–22710. DOI: 10.1039/C5CP02942B.

[44] S.R. Raga, F. Fabregat-Santiago, Temperature effects in dye-sensitized solar cells, *Phys. Chem. Chem. Phys*., 2013, 15, 2328. DOI: 10.1039/c2cp43220j.

[45] F. Santos, C. Hora, G. Bernardo, D. Ivanou, A. Mendes, Efficient Monolithic Dye Sensitized Solar Cells with Eco-Friendly Silica-Titania Spacer Layers, *Sol. Energy*, 2019, 183, 419–424. DOI: 10.1016/j.solener.2019.03.056.

[46] H. Wang, G. Liu, X. Li, P. Xiang, Z. Ku, Y. Rong, M. Xu, L. Liu, M. Hu, Y. Yang, H. Han, Highly efficient poly(3-hexylthiophene) based monolithic dye-sensitized solar cells with carbon counter electrode, *Energy Environ. Sci.*, 2011, 4, 2025–2029. DOI: 10.1039/c0ee00821d.

[47] M. Mahbuburrahman, N. Chandradebnath, J.J. Lee, Electrochemical Impedance Spectroscopic Analysis of Sensitization-Based Solar Cells, *Isr. J. Chem.*, 2015, 55, 990–1001. DOI: 10.1002/ijch.201500007.

[48] H.N. Tsao, C. Yi, T. Moehl, J.H. Yum, S.M. Zakeeruddin, M.K. Nazeeruddin, M. Grätzel, Cyclopentadithiophene bridged donor-acceptor dyes achieve high power conversion efficiencies in dye-sensitized solar cells based on the tris-cobalt bipyridine redox couple, *ChemSusChem*, 2011, 4, 591–594. DOI: 10.1002/cssc.201100120.

[49] J. Gao, A.M. El-Zohry, H. Trilaksana, E. Gabrielsson, V. Leandri, H. Ellis, L. D'Amario, M. Safdari, J.M. Gardner, G. Andersson, L. Kloo, Light-Induced Interfacial Dynamics Dramatically Improve the Photocurrent in Dye-Sensitized Solar Cells: An Electrolyte Effect, *ACS Appl. Mater. Interfaces*, 2018, 10, 26241–26247. DOI: 10.1021/acsami.8b06897.

[50] B. Minnaert, P. Veelaert, A proposal for typical artificial light sources for the characterization of indoor photovoltaic applications, *Energies*, 2014, 7, 1500–1516. DOI: 10.3390/en7031500.

[51] Y. Li, N.J. Grabham, S.P. Beeby, M.J. Tudor, The effect of the type of illumination on the energy harvesting performance of solar cells, *Sol. Energy*, 2015, 111, 21–29. DOI: 10.1016/j.solener.2014.10.024.

CHAPTER 5

MAIN CONCLUSIONS AND OUTLOOK

5

Main Conclusions and Outlook

The work developed along this thesis addresses the state-of-the-art weaknesses of monolithic dye-sensitized solar cells (M-DSSCs). The results obtained allow now the fabrication of more efficient, stable, and cost-effective M-DSSCs, capable of competing favorably with their conventional counterparts. This chapter highlights the main achievements of this thesis work and suggestions for future research.

5.1 Main Conclusions

The indoor photovoltaic (iPV) market continuous growth is being driven by the need of powering low-power electronic devices of the Internet of Things (IoT). Among all possible iPV technologies, dye-sensitized solar cells (DSSCs) stand out with the record power conversion efficiency (PCE) of 34.5 % under 1000 lx room light; capitalizing on their low cost, non-toxicity, versatile design, and pleasing to the eye appearance, DSSCs became the most appealing iPV technology.

The monolithic design of the DSSCs is straightforward to fabricate in-series modules with a reduction of 20-30 % in material costs. Research on monolithic dye-sensitized solar cells (M-DSSCs) is relatively scarce compared with the research on conventional architecture DSSC. Also, most of the research on M-DSSCs addresses the development of cost-effective counter-electrodes, but there is a noticeable lack of works on the insulating spacer layer. Besides the porous structure and the insulating properties, the spacer layers made of highly reflective materials enhance the light harvesting in the device. **Chapter 2** reports the study of SiO_2 spacer layers made of nanoparticles of *ca.* 20 nm, entirely derived from a water-based formulation. The reflectance of this SiO_2 spacer layer, *ca.* 30 %, was enhanced adding TiO_2 nanoparticles of also *ca.* 20 nm. A sharp increase of light reflectance from the spacer layer, up to *ca.* 70-76 %, was observed using a TiO_2 mass fraction of 25-30 % due to the formation of TiO_2 agglomerates and its higher refractive index of TiO_2 compared with SiO_2 (2.5 *vs* 1.5), resulting in an increase of the IPCE spectra above 450 nm; higher concentrations of TiO_2 onset electron percolation from the photoanode to the counter-electrode - recombination. M-DSSCs using a SiO_2 spacer layer containing 30 % in mass of TiO_2 nanoparticles, and a Pt metal counter-electrode

rendered a device with 1-sun PCE of 8.3 %, the record PCE of iodide-mediated M-DSSCs. The reflectance of these SiO_2-TiO_2 spacer layers can be further enhanced using nanoparticles with higher refractive indexes and band gaps above 3.2 eV. The sensitization time effect on the photovoltaic performance of M-DSSCs was also addressed for the first time. The optimum sensitization time for conventional DSSCs sensitized with ruthenium dyes is 12-48 h. However, the additional spacer layer and thick carbon-based counter-electrode of the M-DSSC, make the optimum sensitization time increase to *ca.* 60-70 h of dipping in an ethanolic solution of N719, at room temperature.

The counter-electrode of M-DSSCs must have high electrical conductivity and electrocatalytic activity, and the pores of the triple-layer structure (counter-electrode, spacer layer, sensitized TiO_2 mesoporous layer) should be large enough for fast charge carriers' diffusion. **Chapter 3** studies the apparent activation energy for electron transfer (E_a), the electron charge transfer resistance at counter-electrode/electrolyte interface (R_{CE}), and the exchange current density (J_0) for different materials in cobalt(III/II) redox electrolyte: Pt nanoparticles, Pt metal, graphite/carbon-black and poly(3,4-ethylenedioxythiophene) polystyrene sulfonate (PEDOT:PSS). Among these, PEDOT:PSS presents the lowest apparent activation energy (E_a), 15.6 $kJ \cdot mol^{-1}$. However, the poor integrity of PEDOT:PSS films, prepared by spin-coating, resulted in high series resistance (R_S) and low open-circuit potential (V_{OC}); the deposition of PEDOT:PSS solution over the spacer layer clogged the pores and hindered the diffusion of the charge carriers, resulting in incredibly high internal resistances and low performance. Graphite/carbon-black counter-electrode presented a slightly higher E_a than PEDOT:PSS, 16.9 $kJ \cdot mol^{-1}$, which turned this material a good catalyst for the reduction of $Co(bpy)_3^{3+}$. Cobalt-mediated M-DSSC using a highly reflective TiO_2-rutile spacer layer and a graphite/carbon-black counter-electrode rendered a PCE of 9.5 % under 1-sun simulated solar illumination, the highest ever reported for liquid-junction M-DSSCs. A decent PCE of *ca.* 22 % was achieved under 1000 lx light intensity provided by a LED lamp, showing excellent prospects of the developed M-DSSCs for indoor use. 4-*tert*-butylpyridine (TBP) is added to the electrolyte solution to mitigate the back electron recombination by adsorption at the TiO_2 surface; the diffusion of cobalt species can, however, be affected by a high concentration of TBP. The conventional DSSC architecture often uses 0.6-0.8 M of TBP; M-DSSCs may require a different concentration of TBP, since TiO_2 and carbon layers adsorb TBP from the electrolyte, decreasing the amount of TBP available in the electrolyte. The best photovoltaic performance of the prepared cobalt-mediated M-DSSCs was obtained for 1.2 M concentration of TBP. The prepared cobalt-mediated M-DSSCs were sensitized with a Zn-porphyrin, YD2-*o*-C8, which displays a higher extinction coefficient than the ruthenium dyes, allowing a more efficient light harvesting using thinner TiO_2 mesoporous layers. In this case, the best performance was reached after *ca.* 46±2 h of sensitization time.

The emergence of redox mediators with higher redox potential than I_3^-/I^-, such as Co(III)/Co(II) and Cu(II)/Cu(I), allow DSSCs to attain higher V_{OC} and PCEs. However, there is a lack of information regarding the long-term stability of these devices. Most of the research on cobalt-mediated DSSCs concerns the optimization of the electrolyte composition and uses light-soaking times shorter than 500 h illuminated with white LED lamps, which does not contribute to the heating up of the devices. Nevertheless, there are few works considering at least 1000 h of aging under 1-sun, and all report pronounced device degradation. In **Chapter 4** was addressed the long-term stability of cobalt-mediated M-DSSCs; the device edges and the electrolyte injection holes were glass-sealed using a laser-assisted encapsulation process. The seal tightness complied with the standard helium gas leak test MIL-STD-883, method 1014.10, and resisted the humidity-freeze cycles according to IEC 61646 standard. Glass-encapsulated M-DSSCs loaded with ACN-based cobalt electrolyte passed successfully, and for the first time, the ISOS standard tests for a thermal cycle of 85 ºC. The prepared devices showed the most steady history of photovoltaic metrics ever recorded for 1000 h under dark, 1-sun, and 600 lx of illumination. The glass encapsulation process demonstrated to be a critical tool for developing high PCE performing devices that meet the stability required for a certificated record.

Finally, it should be emphasized that this thesis presents two records a) 1-sun PCEs of M-DSSCs (8.3 % in iodide-mediated M-DSSCs and 9.5 % in cobalt-mediated M-DSSCs), and b) fully stable cobalt-mediated DSSC according to ISOS standard tests. PCEs of *ca*. 22 % were reached with cobalt-mediated M-DSSCs under 1000 lx, showing that these devices are suitable for indoor applications.

5.2 Outlook

Since the first M-DSSC was reported, several approaches were followed to improve the photovoltaic and cost performance of these devices: the material cost and transparency of the layers were assessed developing cost-effective counter-electrodes and alternative spacer layers; the commercial aptitude for these devices was exploited producing M-DSSCs modules in rigid and flexible substrates; the stability issues were addressed using less volatiles electrolytes or solid-state hole transport materials (HTMs).

The transparency of M-DSSCs can be enhanced using semi-transparent spacer layers made of *ca.* 20-30 nm of SiO_2, TiO_2, and ZrO_2 nanoparticles, but compromising the reflectivity of this layer and the light harvesting of the devices, as shown in **Chapter 2**. Regarding the counter-electrodes, their transparency could be improved by replacing the most used carbonaceous materials with polymers, such as poly (3,4-ethenedioxythiophene) (PEDOT), or metal layers, such as Pt loaded with *ca.* 70 nm of indium tin oxide (ITO) nanoparticles. Recently, the graphite/carbon-black

counter-electrode used in **Chapters 3** and **4** was replaced by a thin PEDOT film (*ca.* 150 nm) deposited by spin-coating of a PEDOT:PSS aqueous solution. The sensitization of the TiO_2 mesoporous layer was performed prior to PEDOT:PSS deposition and the devices were properly masked using a Kapton tape, resulting in M-DSSCs with enhanced transparency, and a PCE of 8.4 % under 1-sun simulated solar light, and a PCE of *ca.* 30 % under 1000 lx light intensity. This is an ongoing work at the research team.

Another drawback of carbon counter-electrodes is the poor adhesion to the TCO-coated glass substrate, resulting in high electronic contact resistances and low fill factors. The sheet resistance of DSSCs increases in large area fluorine or indium-doped substrates; large area M-DSSCs using carbon-based counter-electrodes may present low FF and PCE. M-DSSCs with active areas of *ca.* 0.07 cm^2 and *ca.* 4 cm^2 were recently prepared in the group, rendering average PCEs of 8.5 % and 3.8 %, respectively, under 1-sun simulated solar light. The next step must be the production of M-DSSCs modules; the charge collection in M-DSSCs modules must be enhanced using current collectors, such as metal grids; however, when corrosive electrolytes are used, the metal grids should be protected. Ultimately, the TCO-coated substrate of M-DSSCs could be replaced by conducting plastic or metallic substrates, which are suitable for flexible devices and portable applications.

Among other factors, the stability of DSSCs depends on the quality of device encapsulation. Fully stable cobalt-mediated M-DSSCs were produced using laser-assisted glass-frit encapsulation, as presented in **Chapter 4**. In liquid-junction DSSCs, the electrolyte leakage through the pre-drilled holes can be reduced using less volatile organic solvents or ionic liquids, as solvents. Another option is the production of solid-state DSSCs, by replacing the liquid redox mediator with a solid-state hole transporting material (HTM). Organic and inorganic molecules, polymers, and coordination metal complexes are the most common HTM for solid-state DSSCs. Among them, copper-HTMs are the most attractive nowadays; these HTMs are produced by slow evaporation at room temperature of the electrolyte solvent of liquid-state copper-mediated DSSCs. The higher redox volt of the copper complexes and the thicker mesoporous TiO_2 layers of these solid-state DSSCs allowed achieving a PCE of 11.7 % under 1-sun simulated solar light. Liquid-junction M-DSSCs were recently produced in the group using an organic dye, Y123 dye, and a $[Cu(tmby)_2]TFSI_{2/1}$ (tmby = 4,4´,6,6´-tetramethyl-2,2´-bipyridine)] redox mediator, rendering a PCE of 6.6 % under 1-sun simulated solar light in the first experiments; unfortunately, the copper-HTMs were not assessed yet in the M-DSSC architecture. The highest PCEs recorded under indoor illumination turn DSSCs as one of the most attractive PV technologies to low-power electronic devices of the IoTs. All the strategies mentioned above must contribute to the development of efficient, stable, and cost-effective M-DSSCs modules for indoor use.

APPENDIX

Appendix A. Characterization of $SiO_2@xTiO_2$ spacer layers.

Appendix B. Determination of charge-transfer resistance and exchange current density of different materials for the Co(III) reduction at different temperatures.

Appendix C. Morphology of commercial TiO_2 and ZrO_2 spacer layers.

Appendix A. Characterization of $SiO_2@xTiO_2$ spacer layers

In M-DSSCs, the spacer layer must be porous to allow the diffusion of the charge carriers in the electrolyte solution and, at the same time, must be insulating to avoid direct contact between photoanode and counter-electrode. N_2 adsorption/desorption isotherms were obtained for the powder of sintered $SiO_2@xTiO_2$ spacer layers, which allowed to determine the specific surface area and the average pore diameter of these layers using Brunauer-Emmett-Teller (BET) and Barret-Joiner-Halenda (BJH) equations. These isotherms, as well the cumulative pore volume distribution and its differentiation in function of the pore radius, are shown in **Fig. A1**. The specific surface area (SSA) and the average pore diameter (r_p) obtained from BET and BJH equations, respectively, are displayed in **Table A1**.

The BET equation assumes that the layer has uniform and cylindrical pores estimated by the **eq. (A1)**, where n_g is the specific amount of adsorbed gas at the relative pressure P/P_0, P is the pressure, P_0 is the saturation pressure, n_m is the monolayer capacity of the adsorbed gas, and C is a BET constant [1].

$$\frac{\frac{P}{P_0}}{n_g(1-\frac{P}{P_0})} = \frac{1}{n_m \times C} + \frac{(C-1)}{n_m \times C} \times \frac{P}{P_0} \tag{A1}$$

The specific surface area (SSA) is then determined using **eq. (A2)**, where m is the mass of adsorbate, N is the Avogadro's number, and A_{cs} is the adsorbate cross sectional area - 16.2 $Å^2$ for N_2) [1].

$$\text{SSA} = \frac{n_m \times N \times A_{cs}}{m} \tag{A2}$$

Regarding BJH equation, here is assumed a capillary condensation of N_2 inside the pores. For each desorption step, the average pore diameter r_p is calculated from Kelvin equation and the statistical t-plot method, according with the **eq. (A3)** to **eq.(A5)**, where r_k is the Kelvin radius and t is the film thickness [2].

$$\log\frac{P}{P_0} = \frac{-4.14}{r_k} \tag{A3}$$

$$\log\frac{P}{P_0} = 0.034 - \frac{13.99}{t^2} \tag{A4}$$

$$r_p = r_k + t \tag{A5}$$

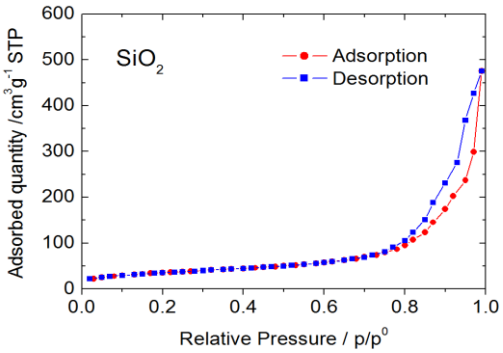
SiO2
Adsorption
Desorption
Adsorbed quantity /cm3g-1 STP
Relative Pressure / p/p0

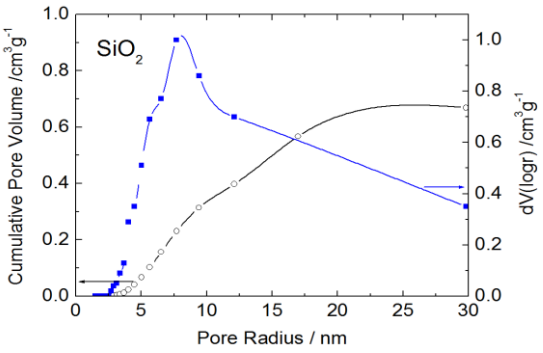
SiO2
Cumulative Pore Volume /cm3g-1
dV(logr) /cm3g-1
Pore Radius / nm

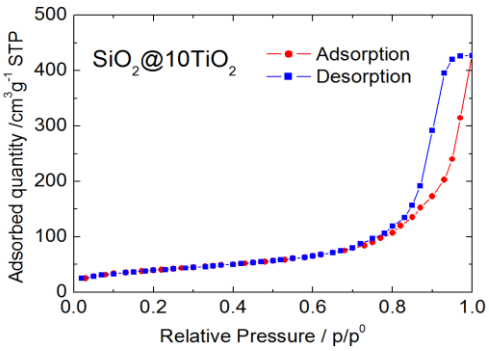
SiO2@10TiO2
Adsorption
Desorption
Adsorbed quantity /cm3g-1 STP
Relative Pressure / p/p0

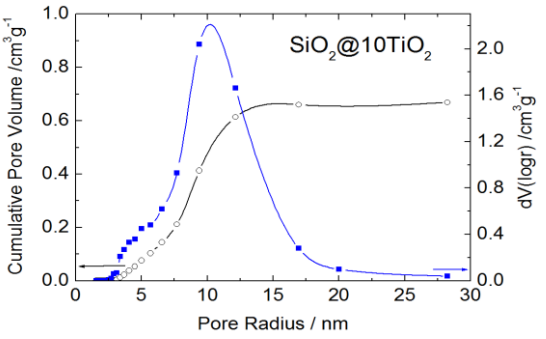
SiO2@10TiO2
Cumulative Pore Volume /cm3g-1
dV(logr) /cm3g-1
Pore Radius / nm

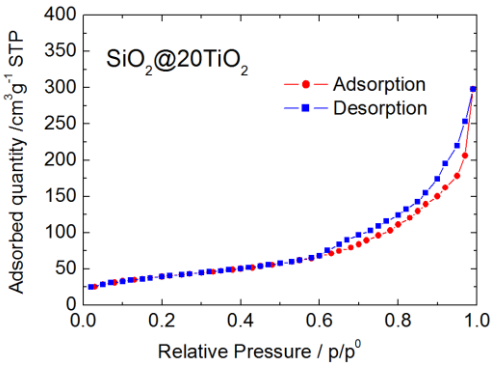
SiO2@20TiO2
Adsorption
Desorption
Adsorbed quantity /cm3g-1 STP
Relative Pressure / p/p0

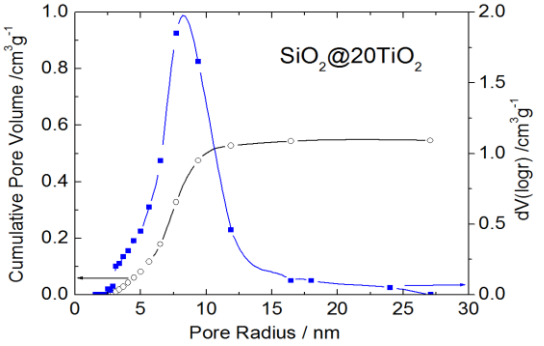
SiO2@20TiO2
Cumulative Pore Volume /cm3g-1
dV(logr) /cm3g-1
Pore Radius / nm

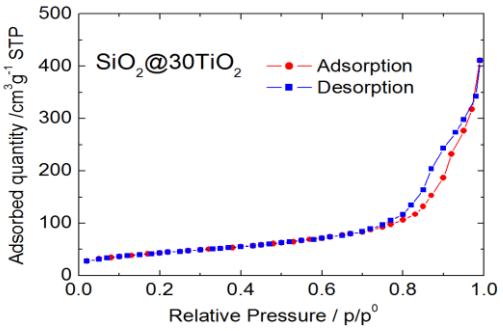
SiO2@30TiO2
Adsorption
Desorption
Adsorbed quantity /cm3g-1 STP
Relative Pressure / p/p0

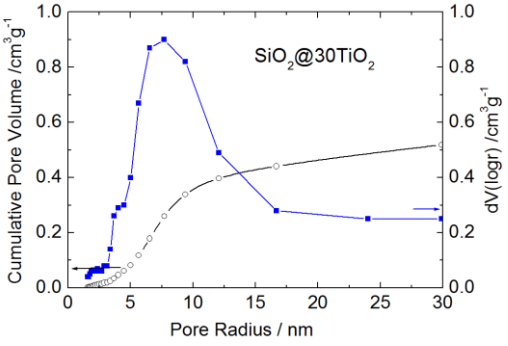
SiO2@30TiO2
Cumulative Pore Volume /cm3g-1
dV(logr) /cm3g-1
Pore Radius / nm

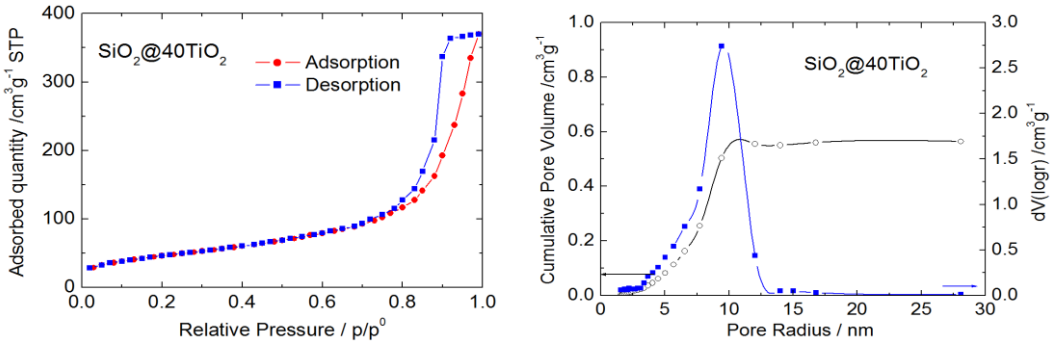

Fig. A1 N_2 adsorption/desorption isotherms for $SiO_2@xTiO_2$ (left column); cumulative pore volume distribution and dV(log*r*) *vs* pore radius for $SiO_2@xTiO_2$ (right column).

Table A1

Specific surface area and an average pore diameter of the spacer layers.

Electrical spacer	**SSA, $m^2 \cdot g^{-1}$**	**r_p, nm**
SiO_2	125 ± 20	15.0 ± 2.4
$SiO_2@10TiO_2$	140 ± 20	19.0 ± 2.4
$SiO_2@20TiO_2$	139 ± 20	14.0 ± 2.4
$SiO_2@30TiO_2$	153 ± 20	15.4 ± 2.4
$SiO_2@40TiO_2$	166 ± 20	18.8 ± 2.4

Further characterization was performed using Energy-Dispersive X-Ray Spectroscopy (EDS); EDS mapping was used to visualize TiO_2 distribution in the spacer layers, and it is presented in **Fig. A2**. The element composition of the $SiO_2@xTiO_2$ spacer layers is presented in **Table A2**.

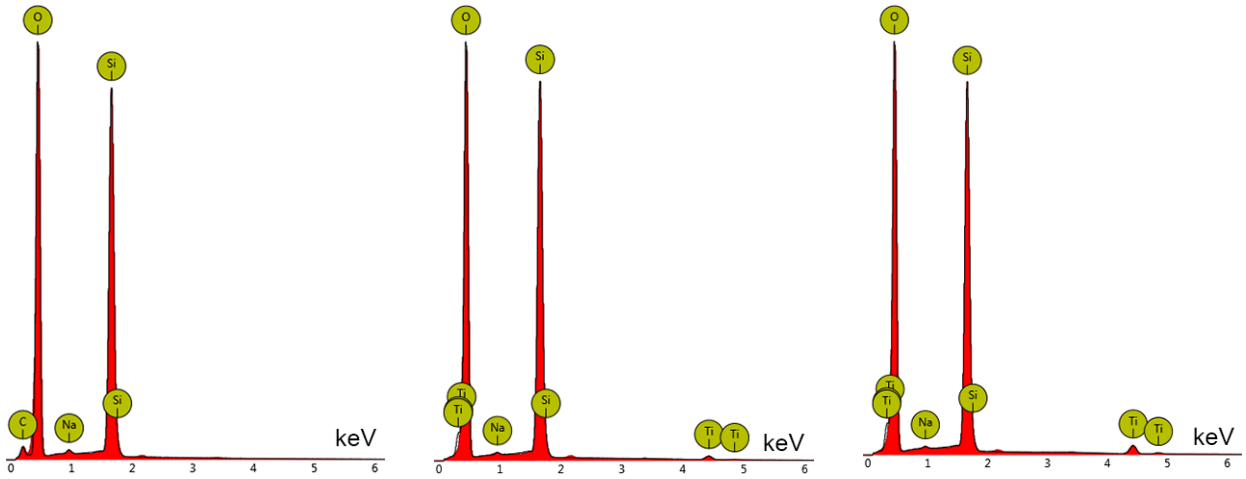

(a) (b) (c)

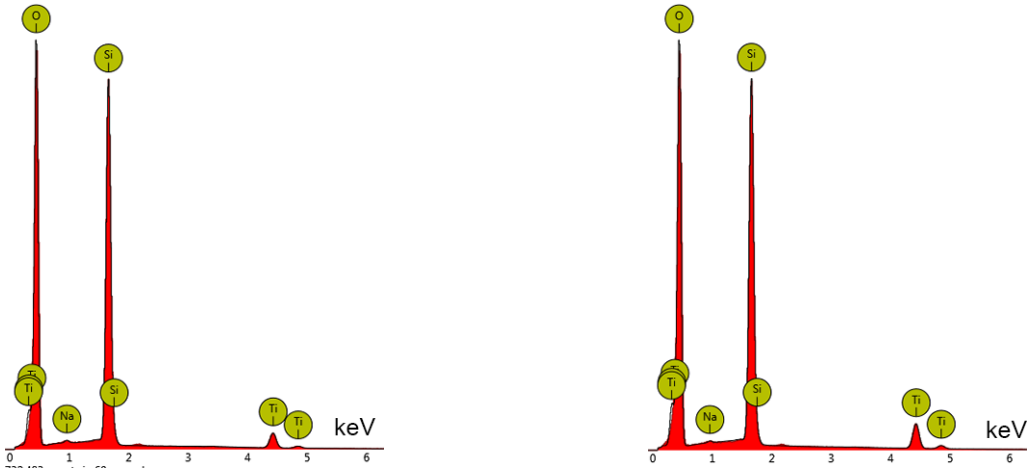

(d) (e)

Fig. A2 EDS of SiO_2@$x$$TiO_2$ films with different mass fraction x of TiO_2; ***a***, ***b***, ***c, d*** and ***e*** are the spectra for x = 0, 10, 20, 30 and 40 respectively.

Table A2

Element composition (in the form of oxides) of the spacer layers obtained by EDS.

Spacer layer	TiO_2 (wt.%)	SiO_2 (wt.%)	Na_2O (wt.%)
SiO_2	-	99.1	0.9
SiO_2@10TiO_2	9	90.4	0.6
SiO_2@20TiO_2	19.2	80.3	0.5
SiO_2@30TiO_2	29.9	69.6	0.5
SiO_2@40TiO_2	41.0	58.7	0.3

References

[1] F. Ambroz, T.J. Macdonald, V. Martis, I.P. Parkin, Evaluation of the BET Theory for the Characterization of Meso and Microporous MOFs, *Small Methods*, 2018, 2, 1800173. DOI: 10.1002/smtd.201800173.

[2] R. Bardestani, G.S. Patience, S. Kaliaguine, Experimental methods in chemical engineering: specific surface area and pore size distribution measurements—BET, BJH, DFT, *Can. J. Chem. Eng*., 2019, 97, 2781– 2791. DOI: 10.1002/cjce.23632.

Appendix B. Determination of charge-transfer resistance and exchange current density of different materials for the Co(III) reduction at different temperatures.

The apparent activation energy of different materials - platinum nanoparticles (Pt_{NP}), platinum metal (Pt_{Met}), carbon-black/graphite (GCB) and PEDOT:PSS - for the reduction of Co(III) was determined using Arrhenius equation, **eq. (3.2)**; the Arrhenius plots are displayed in **Fig. 3.3**. In **Table B1** is presented the R_{CE} and the J_0 determined for each counter-electrode, in a range of temperature between -5 and 50 ºC.

Table B1

Charge transfer resistance (R_{CE}) and exchange current density (J_0) for counter-electrodes at different temperatures.

T/ ºC	R_{CE} /Ω·cm^2				J_0 /mA·cm^{-2}			
	Pt_{NP}	**Pt_{Met}**	**PEDOT:PSS**	**GCB**	**Pt_{NP}**	**Pt_{Met}**	**PEDOT:PSS**	**GCB**
-5	169.2	19.4	6.8	0.28	0.14	1.2	3.4	81.6
0	142.4	17.0	5.7	0.25	0.17	1.4	4.1	96.1
5	120.2	15.1	5.0	0.22	0.20	1.6	4.8	111.8
10	103.6	13.3	4.4	0.18	0.24	1.8	5.6	133.0
15	-	11.8	4.1	0.17	-	2.1	6.1	149.2
20	73.0	10.6	3.6	0.14	0.35	2.4	6.9	175.4
25	-	9.3	3.3	-	-	2.8	7.8	-
30	48.0	8.1	3.1	0.13	0.54	3.2	8.5	204.5
35	-	7.2	2.9	0.12	-	3.7	9.2	231.1
40	36.0	6.0	2.7	0.10	0.75	4.5	9.9	263.9
50	27.0	4.6	2.5	0.09	1.03	6.1	11.3	297.4

Appendix C. Morphology of commercial TiO_2 and ZrO_2 spacer layers.

Top-view SEM images showing the morphology of the spacer layers used in Chapters 3 and 4 are presented in **Fig. C1**.

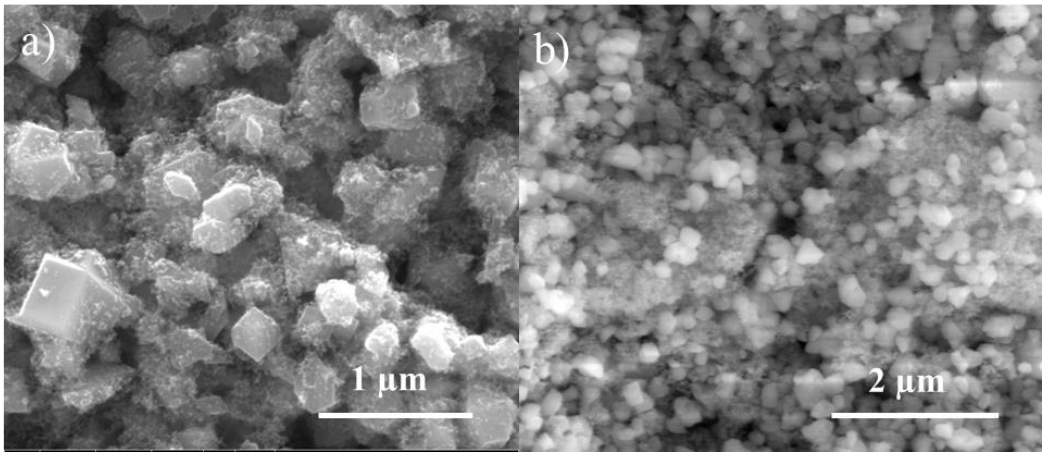

Fig. C1. Top-view SEM images of TiO_2 (***a***) and ZrO_2 (***b***) electrical spacer layers.